VSB TECHNICAL UNIVERSITY OF OSTRAVA
IT4INNOVATIONS NATIONAL SUPERCOMPUTING CENTER

Dynamics of cardiac electrophysiology models

Dynamika modelů srdeční elektrofyziologie

Radek Halfar

PhD Thesis

Supervisor: prof. RNDr. Marek Lampart, Ph.D.

Ostrava, 2023

Abstrakt a přínos práce

Srdeční arytmie jsou ve vyspělém světě rozšířeným onemocněním, zejména u starší populace, a hlavní příčinou úmrtí. Jejich původ je velmi složitý a těžko předvídatelný. Příčiny tohoto onemocnění jsou různé. K nepravidelnému šíření řídících signálů v srdeční tkáni může dojít v důsledku zjizvení srdeční tkáně po infarktu, ucpání tepen v srdci, infekce COVID-19 atd. V této práci jsou analyzovány dynamické vlastnosti srdeční elektrofyziologie a jejich změny při patofyziologickém šíření elektrických signálů v srdci. Nelineární analýzou matematických modelů srdečních buněk jsou nalezeny kombinace stimulačních frekvencí a amplitud, při kterých dochází k chaotických odpovědím srdeční elektrofyziologie. Dále jsou prezentovány možnosti využití umělé inteligence k detekci nebezpečných míst na základě prostorového uspořádání jizev v srdci.

Klíčová slova

dynamické systémy, chaos, 0-1 test na chaos, kvantifikační analýza rekurence, entropie, neuronové sítě, srdeční fibróza, srdeční akční potenciál

Abstract and Contributions

Cardiac arrhythmias are a widespread disease in the developed world, especially in the elderly population, and a leading cause of death. Their origin is very complex and difficult to predict. The causes of this disease are various. Irregular propagation of control signals in heart tissue can occur due to scarring of heart tissue after a heart attack, clogging of arteries in the heart, infection with COVID-19, etc. This work analyses the dynamic properties of cardiac electrophysiology and their changes during the pathophysiological propagation of electrical signals in the heart. Using nonlinear analysis of mathematical models of heart cells are found combinations of stimulation frequencies and amplitudes, at which chaotic responses of cardiac electrophysiology occur. Furthermore, the possibilities of using artificial intelligence to detect dangerous sites based on the spatial arrangement of scars in the heart are presented.

Keywords

dynamical systems, chaos, the 0-1 test for chaos, recurrence quantification analysis, entropy, neural networks, cardiac fibrosis, cardiac action potential

Acknowledgement

I want to thank everyone without whose help this work would not have happened. Especially to my supervisor, prof. RNDr. Marek Lampart, PhD, for his guidance during my PhD study and Professor Kevin Burrage, Dr Brodie Lawson and Professor Rodrigo Weber Dos Santos for their help, without which much of my research would not have happened.

Contents

List of symbols and abbreviations

RQA	–	Recurrence Quantification Analysis
AP	–	Action Potential
RP	–	Recurrence Plot

List of Figures

List of Tables

Chapter 1

Introduction

Cardiac arrhythmias are a collective term for heart rhythm disorders. These disorders include, for example, slowed or accelerated heart rhythm (bradycardia and tachycardia resp.) or disordered electrical activity in the tissue (fibrillation). The onset of arrhythmia is complex and difficult to anticipate. Although the function and dysfunction of the heart have been extensively studied, the sheer complexity of the spatiotemporal dynamics underlying its electrical signalling process leaves much still poorly understood. This is particularly true when complicating factors are present, such as cardiac fibrosis.

Due to the physiological nature of this problem, research *in silico* is an important part of its solution. The beginnings of this research can be dated to 1952, when Alan Hodgkin and Andrew Huxley created a mathematical model explaining the ionic mechanisms underlying the initiation and propagation of action potential (AP) in the squid giant axon. Since then, many mathematical models have been developed describing this ion mechanism in cardiac cells. These models mainly aim to understand complex physiological phenomena and as patient-specific models for streamlining therapy.

In this work, the influence of pathology on the dynamic properties of cardiac electrophysiology is analyzed. The main findings presented here can be divided into two parts.

In the first part, dangerous parameters of the stimulation current are found, during which chaotic responses of heart cells occur. For this purpose, several mathematical models paced with varying stimulation frequency and amplitude combinations are used. The Fourier spectra and bifurcation diagrams were used to detect the irregular character of AP changes in cell. In addition, the chaotic behaviour of action potential was confirmed by the 0–1 test for chaos.

Finally, the possibilities of using artificial intelligence to detect potentially dangerous sites in the heart tissue are demonstrated. These sites are searched by analyzing the tissue's spatial arrangement of fibrosis (scarring). Fibrotic tissue is caused by pathological conditions in the heart (such as congestive heart failure, cardiomyopathy, etc.) or simply by ageing. Fibrotic

cells can separate myocytes, resulting in tortuous paths of activation that increase the risk of signalling malfunctions.

The main findings presented in this work are summarized in three published journal research papers (WoS) and two indexed conference papers.

The outline of this work is following. In the Chapter 2 the nonlinear analysis methods used in this work are summarized. Specifically, a basic summary of recurrence quantification analysis (RQA) in Section 2.2 and the 0-1 test for chaos in Section 2.3 is given here. Furthermore, entropy calculation options in Section 2.4. The use of these methods is demonstrated using the Hénon map (see Section 2.1). Chapter 3 summarizes the main research contributions achieved in this work. The results achieved in the field of heart cell dynamics (Section 3.1) and section 3.2 describes the results attained in the field of using artificial intelligence to detect dangerous proarrhythmogenic sites in heart tissue. Published full papers related to presented work are listed in Chapter 4. Chapter 5 concludes the achieved results and list of all the author's published papers is then given in the appendix.

Chapter 2

Nonlinear analysis methods

After the discovery of the butterfly effect by Edward Lorenz, thanks to the increase in computing power of computers and the attractiveness of chaos theory, the development of new methods of analyzing dynamical systems took place. In this work, a combination of classical and modern techniques for the study of dynamic systems is used. This set of different mathematical methods for dynamic system analysis ensures a robust analysis of time series dynamic behaviour. Each method examines a slightly different aspect of dynamic motion. For complex analysis, it is necessary to use a set of methods thanks to which more detailed information about the system's behaviour can be obtained. The use of those methods is demonstrated through the analysis of the Hénon map.

2.1 Hénon map

This map was introduced by Michel Hénon [1] as a simplified model of the Poincaré section of the Lorenz equations. The Hénon map is a real two-dimensional discrete-time dynamical system (see Equation (2.1)). In this work, only the variable x is investigated using the presented methods (due to the shape of Equation (2.1), this analysis is sufficient).

$$\begin{cases} x_{n+1} = 1 - ax_n^2 + y_n \\ y_{n+1} = bx_n \end{cases} \tag{2.1}$$

This map consists of two parameters, a and b. In this paper, the initial condition $x_0 = 0.63135448$, $y_0 = 0.18940634$ with parameter $b = 0.3$ are used. These values are identical to the parameters published in [1]). The parameter a is changed from $a = 1$ to $a = 1.4$ with step 0.005. In this range, Hénon maps show both regular and chaotic behaviour (see Figure 2.1, and Figure 2.2). For the parameter a computed in this range, the chaotic motions are concentrated in three regions $a \in \{[1.06, 1.225] \cup [1.27, 1.295] \cup [1.31, 1.4]\}$.

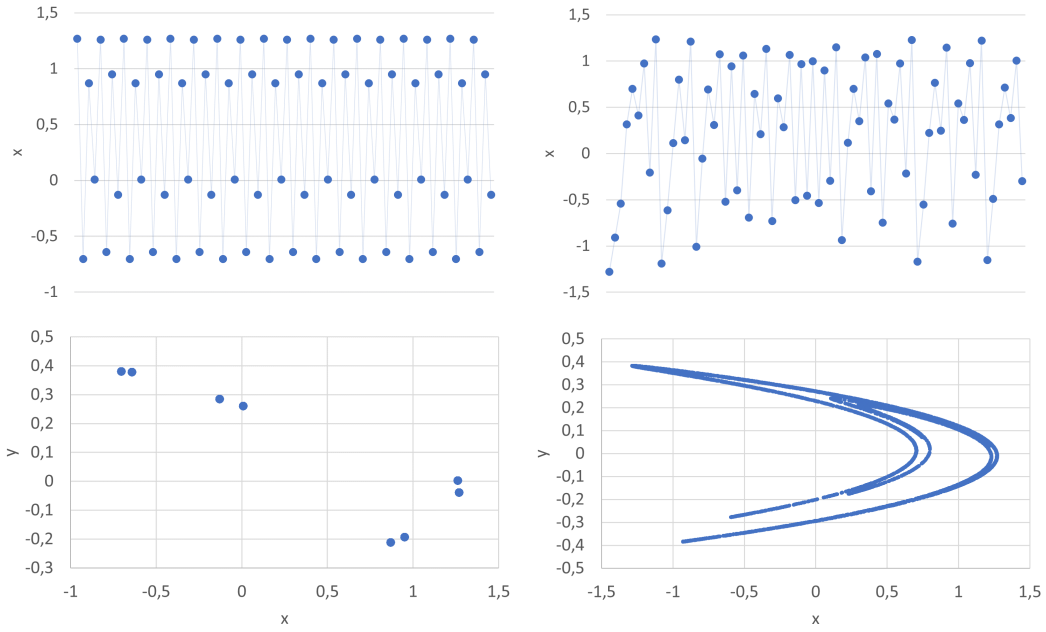

Figure 2.1: Example of a Hénon map showing regular behaviour for $a = 1.035$ (left column). The solution for this parameter value shows a periodic orbit (8 cyclus). This solution can be seen in the time series of the variable x (upper left) and the phase portrait (bottom left), in which only eight values can be seen. For parameter $a = 1.4$, the solution for Equation (2.1) is chaotic motion. An irregular movement can be seen in the time series of the variable x (upper right). The phase portrait of this solution (bottom right) depicts a strange attractor.

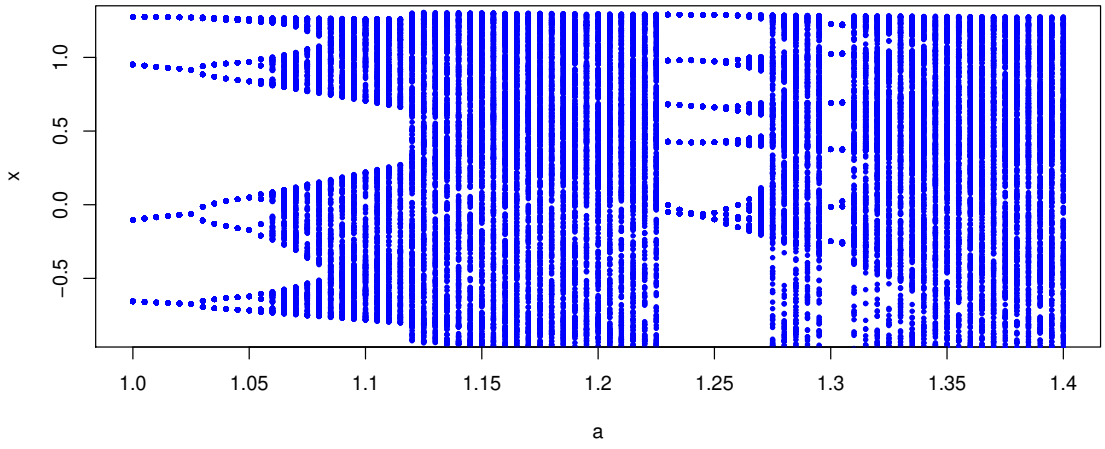

Figure 2.2: Bifurcation diagram of variable x for parameters $a \in [1, 1.4]$. The parameter a is marked on the horizontal axis. All values of the variable x computed with parameter a are depicted on the vertical axis. In the case of regular motions of the Hénon map, only isolated points can be seen in the diagram for a given a since the variable x cyclically reaches the same values. The chaotic behaviour does not manifest periodicity. Therefore, the line is visible for the given a, which denotes many unique values of the variable x.

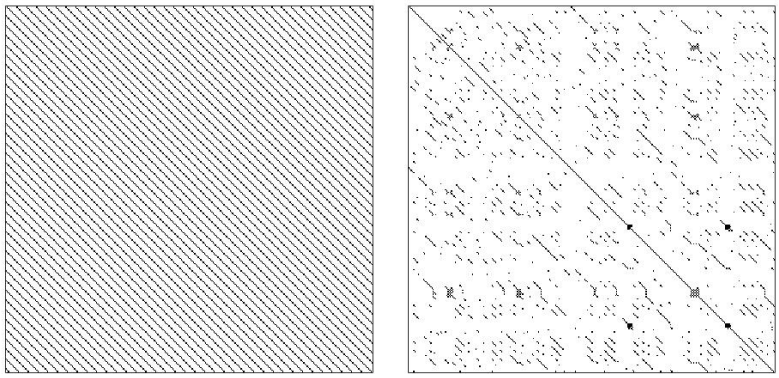

Figure 2.3: Examples of computed recurrence plots for the regular motion (left) of the Hénon map ($a = 1.035$) and for the parameter $a = 1.4$ in which the Hénon map is in a chaotic regime (the original time series are shown in Figure 2.1). Long uninterrupted lines characterize the regular motion of a dynamic system. There is no periodic behaviour in the chaotic regime. The short diagonal lines appear due to the introduction of the threshold ϵ in Equation (2.2).

2.2 Recurrence Quantification Analysis

Recurrence quantification analysis (RQA) [2, 3] is a nonlinear dynamic system analysis method. This method analyzes the recurrence of a dynamic system (the return of a dynamic system to the same position in phase space) displayed using a recurrence plot (RP). RP is a two-dimensional array consisting only of ones and zeros. The time is marked on both of its axes. The value of RP at position (i, j) depicts whether the examined dynamic system at time t_i and t_j recur ($R_{(i,j)} = 1$) or not ($R_{(i,j)} = 0$). The RP is calculated using Equation (2.2).

$$R_{i,j} = \theta(\epsilon - ||\mathbf{x}_i - \mathbf{x}_j||), \qquad \mathbf{x}_i \in \mathbb{R}^m, \qquad i, j = 1 \dots N \tag{2.2}$$

Here $\mathbf{x}_i$ denotes the values of the system's m dependent variables at the moment of its i-th snapshot, with N the total number of snapshots. The Heaviside function θ specifies that recurrence occurs when the difference, under some choice of norm $\|\cdot\|$, falls under the threshold ϵ. During regular behaviour, a dynamical system visits the exact location in phase space at regular intervals. Thanks to this, the recurrence plot created from regular movement manifests long uninterrupted lines. However, in the case of chaotic behaviour, the dynamical system does not reach the same place in phase space. In these cases, the recurrence is detected due to the threshold ϵ in Equation (2.2), and patterns (short diagonal lines, rectangles, etc.) appear in the RP (examples of RP calculated from regular and chaotic behaviour of the Hénon map are depicted in Figure 2.3).

RP can be analysed using RQA, which quantifies this two-dimensional matrix utilising a number of measures. These measures examine the quantity and spatial arrangements of

Table 2.1: Description of RQA measures used in this work.

Equation	**Description**
$\mathrm{REC} = \frac{1}{N^2}\sum_{i,j=1}^{N}\mathbf{R}(i,j)$	Percentage of recurrence points in a recurrence plot
$\mathrm{DET} = \frac{\sum_{\ell=\ell_{\min}}^{N}\ell P(\ell)}{\sum_{\ell=1}^{N}\ell P(\ell)}$	Percentage of recurrence points that form diagonal lines
$\mathrm{RATIO} = N^2\frac{\sum_{l-l_{\min}}^{N} lP(l)}{\left(\sum_{l=1}^{N} lP(l)\right)^2}$	Ratio between DET and REC
$L_{\max} = \max\left(\{l_i; i = 1,\ldots,N_l\}\right)$	Length of the longest diagonal string of recurrence points
$\mathrm{L}_{\mathrm{mean}} = \frac{\sum_{\ell=\ell_{\min}}^{N}\ell P(\ell)}{\sum_{\ell=\ell_{\min}}^{N} P(\ell)}$	Mean length of the diagonal lines
$\mathrm{DIV} = \frac{1}{L_{\max}}$	The inverse of L_{max}
$\mathrm{ENTR} = -\sum_{\ell=\ell_{\min}}^{N} p(\ell)\ln p(\ell)$	The Shannon entropy of the diagonal line lengths distribution
$\mathrm{LAM} = \frac{\sum_{v=v_{\min}}^{N} vP(v)}{\sum_{v=1}^{N} vP(v)}$	Percentage of recurrence points that form vertical lines
$V_{\max} = \max\left(\{v_i; i = 1,\ldots,N_v\}\right)$	Length of the longest vertical line
$\mathrm{V}_{\mathrm{mean}} = \frac{\sum_{v=v_{\min}}^{N} vP(v)}{\sum_{v=v_{\min}}^{N} P(v)}$	Mean length of vertical lines

ones in RP. The equations and description of the RQA measures used in this work is given in Table 2.1.

In Figure 2.4, the RQA measure DET and REC values are shown depending on the parameter a in Equation (2.1). Periodic motion manifests as value 1 for the DET measure because RP only forms diagonal lines. As the complexity of the time series increases, the DET decreases as other patterns and isolated points appear in the RP. Likewise, measure REC also decreases with the higher complexity of the time series. In the case of regular movement of a dynamic system, this measure also reflects the length of the period, as the individual diagonal lines are further apart.

2.3 The 0-1 test for chaos

The 0-1 test for chaos is a method introduced by Gottwald and Melbourne [4] (see also [5]). This method is used for qualitative analysis of time series. The resulting values of this test close to 0 indicate regular time series. If the result is close to 1, it marks the examined series as chaotic. In the case of other resulting values, it is not possible to decide whether it is a regular or chaotic time series. Although this method does not serve to quantify the complexity of a time series (in comparison with RQA or entropy), its advantage lies in the

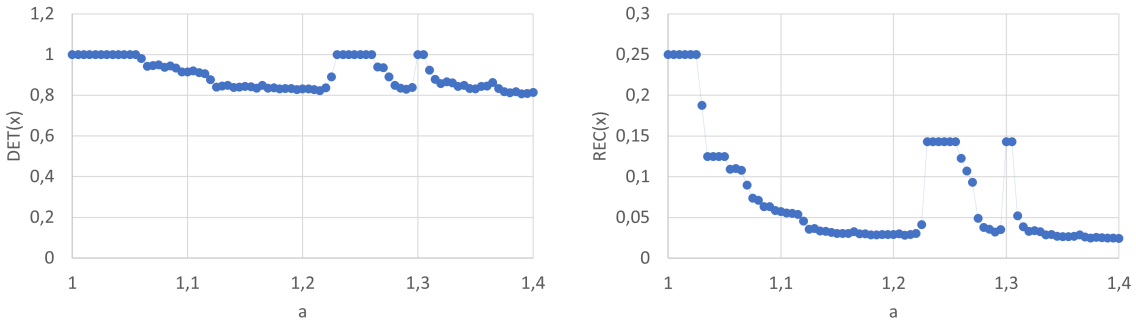

Figure 2.4: RQA results for measures *DET* (left) and *REC* (right) depending on the parameter a. In the case of irregular movement in the time series, the observed RQA measure decreases.

possibility of applying it directly to the investigated time series, without the need to calculate the embedding dimension or time lag. This test can also be used for noisy data.

The calculation procedure of this correlation method is as follows. For a given set of observations $\phi(j)$ for $j \in \{1, 2, \ldots, N\}$ are computed translation variables for suitable choice of $b \in (0, 2\pi)$.

$$p_b(n) = \sum_{j=1}^{N} \phi(j) \cos(jb) = 1,$$

$$q_b(n) = \sum_{j=1}^{N} \phi(j) \sin(jb) = 1,$$

then the mean square displacement is computed using the following equation

$$M_b(n) = \lim_{N\to\infty} \frac{1}{N} \sum_{j=1}^{N} [p_b(j+n) - p_b(j)]^2 + [q_b(j+n) - q_b(j)]^2$$

here $n \leq n_{cut}$ where $n_{cut} \ll N$. The next step is to estimate modified mean square displacement using the following formula

$$D_b(n) = M_b(n) - \left(\lim_{N\to\infty} \frac{1}{N} \sum_{j=1}^{N} \phi(j) \right)^2 \frac{1 - \cos(nb)}{1 - \cos(b)}.$$

Finally, the output of the 0-1 test is computed as correlation coefficient of ξ and Δ for fixed parameter b

$$K_b = \mathrm{corr}(\xi, \Delta)$$

where $\xi = (1, 2, \ldots, n_{cut})$ and $\Delta = (D_c(1), D_c 2, \ldots, D_c(n_{cut}))$. Hence, K_b is dependent on the choice of c. To get K as the output of the 0-1 test, as limiting value of all K_b, the result value

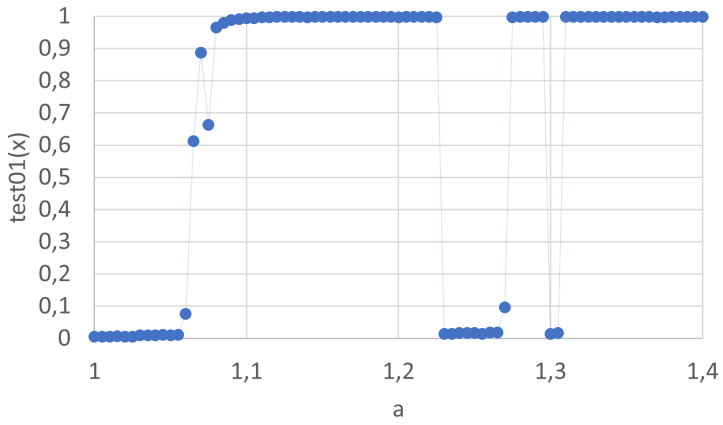

Figure 2.5: Results of the 0-1 test for chaos depending on the parameter a. The results of test classified the regular motion ($test01(x) < 0.05$) in the time series x for the values of the parameter $a \in [1, 1.055] \cup [1.23, 1.265] \cup [1, 3, 1.305]$. For the values of parameter $a \in [1.06, 1.075] \cup [1.23, 1.265] \cup [1, 3, 1.305] \cup 1.27$, it is not possible to decide according to the 0-1 test for chaos whether the investigated time series is chaotic or regular. In the remaining analyzed cases, a chaotic movement was detected.

is taken as

$$K = \text{median}(K_b).$$

The results of the 0-1 test for chaos for parameter a of Hénon map is depicted in Figure 2.5. This test very well found the regions of the a parameter where regular and chaotic Hénon map responses occur. Regular behavior (classified as a test result less than 0.05) is detected for regions $a \in [1, 1.055] \cup [1.23, 1.265] \cup [1, 3, 1.305]$. Chaotic motions in the time series are classified when the result of the 0-1 test for chaos is greater than 0.95. In other cases, the dynamics cannot be decided ($a \in [1.06, 1.075] \cup [1.23, 1.265] \cup [1, 3, 1.305] \cup 1.27$).

2.4 Entropy

Entropy is a dynamic systems theory concept that tries to express the amount of systems' complexity. There are many different kinds of entropy. This work uses approximate entropy (*ApEnt*) and sample entropy (*SampEnt*). *ApEnt* (see Equation (2.3)) as developed by Pincus *et al.* [6] as a method to overcome the requirement of large amounts of data and noise sensitivity. *ApEnt* is based on searching for similar subsequences in the analyzed time series. To avoid the occurrence of natural logarithms of zero in the *ApEnt* calculation, the algorithm counts each sequence as identical to itself, although this also introduces a bias [7]. Richman and Moorman [7] proposed sample entropy (see Equation (2.4)) that removes this bias, is independent of the length of the data and requires fewer computational operations for its

calculation [8]. More information about the computation and usage of these metrics can be found in the paper by Delgado-Bonal and Marshak [9].

$$ApEnt(x, m, r) = \\ = \frac{1}{N-m+1}\left[\sum_{i=1}^{N-m+1}\log\left(\frac{|j_i|}{N-m+1}\right)\right] - \frac{1}{N-m}\left[\sum_{i=1}^{N-m}\log\left(\frac{|k_i|}{N-m}\right)\right], \tag{2.3}$$

where

$$j_i = \{\xi \mid \|y_i - y_\xi\| \leq r \wedge \xi \in \langle 1, N-m+1\rangle\}$$
$$k_i = \{\xi \mid \|z_i - z_\xi\| \leq r \wedge \xi \in \langle 1, N-m\rangle\}$$
$$y_i = [x_i, x_{i+1}, \ldots, x_{i+m-1}], \quad z_i = [x_i, x_{i+1}, \ldots, x_{i+m}], \quad N = |x|.$$

$$SampEnt(x, m, r) = \log\left(\frac{\sum_{i=1}^{N-m+1}|b_i|}{\sum_{i=1}^{N-m}|a_i|}\right) \tag{2.4}$$

where

$$b_i = \{\xi \mid \|y_i - y_\xi\| \leq r \wedge \xi \in \langle 1, N-m+1\rangle \backslash i\},$$
$$a_i = \{\xi \mid \|z_i - z_\xi\| \leq r \wedge \xi \in \langle 1, N-m\rangle \backslash i\},$$
$$y_i = [x_i, x_{i+1}, \ldots, x_{i+m-1}], \quad z_i = [x_i, x_{i+1}, \ldots, x_{i+m}], \quad N = |x|.$$

In Figure 2.6 the *ApEn* measure for Hénon map with respect to parameter a is shown. *ApEn* is low, and as complexity increases, the *ApEn* increase as well. This figure shows that the *ApEn* corresponds well with the results of RQA and the 0-1 test for chaos. However, slight differences can be seen in certain areas. For example, in the examined region of the parameter $a \in [1.04, 1.055]$, it can be seen that the 0-1 test for chaos (see Figure 2.5) classifies these time series as regular. However, there is already an increase in *ApEn*. It is because each method analyses a different aspect of the time series. In addition, it is possible that the resulting values are distorted due to inappropriately chosen parameters of the algorithm. These results show that an increased value of *ApEn* does not necessarily mean a chaotic time series. Therefore, it is necessary not to rely solely on one mathematical method but investigate time series using multiple methods and analyse results about their dynamics concerning each of them.

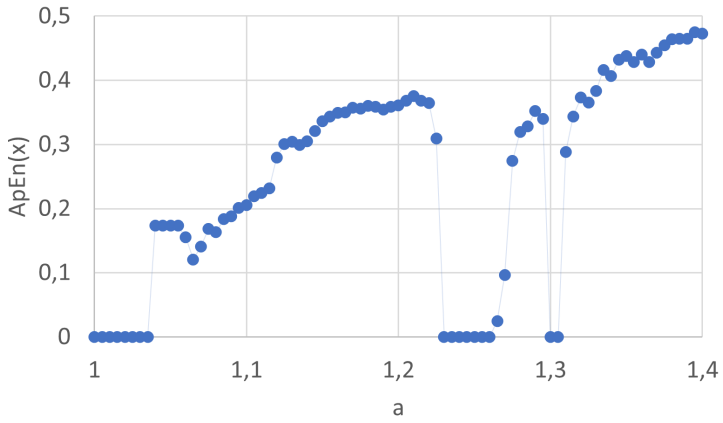

Figure 2.6: Dependence of the approximate entropy of the variable x Hénon map on the parameter a. The $ApEn$ of the regular movement reaches a value close to 0. With the increase in complexity, the $ApEn$ value also increases.

Chapter 3

Summary of author's contributions

This section contains a summary of all scientific results achieved by the author. The author's contributions are divided into two sections. In Section 3.1, the dynamic behavior of the heart cell depending on its stimulation is described and in the second Section 3.2, the results achieved in the application of neural networks for searching for dangerous sites in tissue are described. In these sections, the results achieved by the author himself or based on author's collaboration with other scientists are presented. The presented results were written in the form of scientific papers and published in impact journals. For a complete description of presented results, please see the full papers included in Chapter 4.

3.1 Dynamic behavior of the human heart cell

The dynamic behavior of the heart cell was analyzed using several mathematical models. This work summarizes the main results achieved using two models. The first one is the Fenton-Karma (FK) [10] model. It is a dimensionless model that has 3 degrees of freedom (AP and two gating variables v and w). Complete results are published as journal research paper (see **[TR.1.3]**). Another model whose analysis is summarized in this work is Beeler-Reuter (BR) [11]. This model has 8 degrees of freedom (AP, intracellular Ca^{2+} concentration and 6 gating variables). Complete results can be found in published research paper (see **[TR.1.2]**).

These models were stimulated with regular stimulation current with different combination of amplitude and stimulation period (sum of stimulation delay c and stimulation pulse duration). The stimulation function is composed of the positive half of the sine function and the zero function (see Figure 3.1).

Regular and irregular responses were found for individual stimulation amplitude and frequency combinations. These time series were detected using frequency spectrum analysis (see Figure 3.2) and bifurcation diagrams (see Figure 3.3).

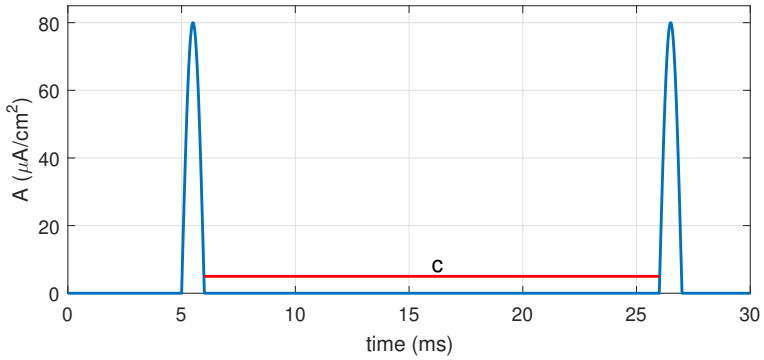

Figure 3.1: Example of stimulation current for amplitude $A = 80$ μA/cm^2, and simulation delay $c = 20$ ms. Parameter c is labeled by red color.

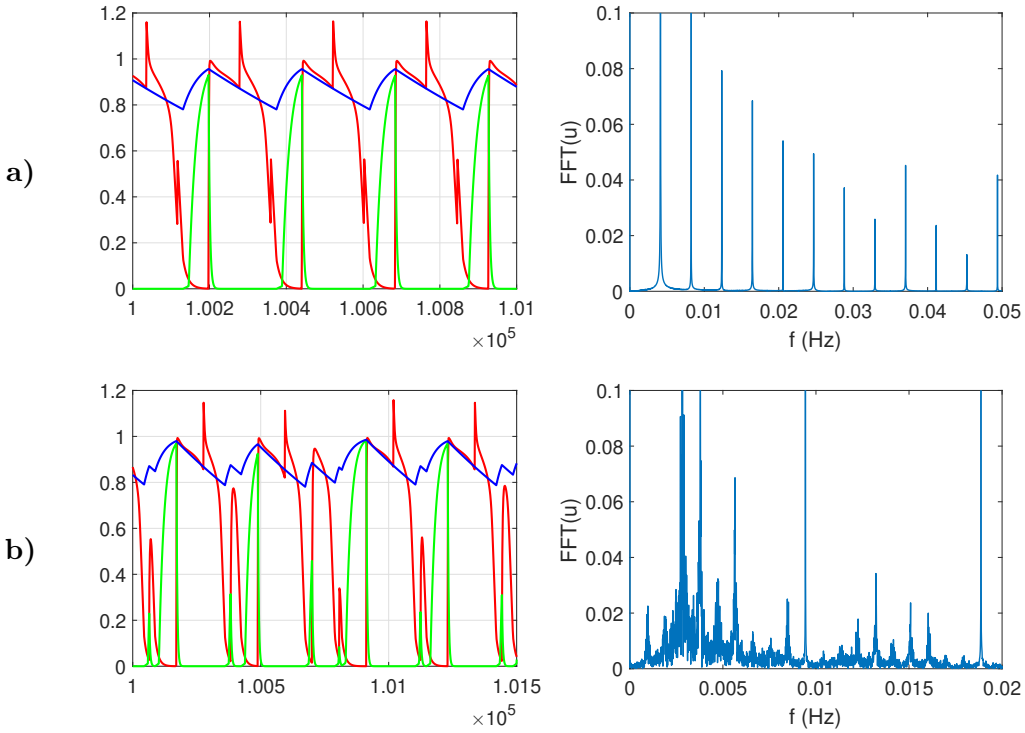

Figure 3.2: Time series showing regular AP motions (row **a**, AP is depicted by red color, and gating variables v (green), and w (blue)). The FK model was stimulated with a periodic signal with stimulation period 80 ms and amplitude 0.48 (left). On the right is depicted the frequency power spectrum of AP. The regular movement of the AP is manifested by discrete peaks in the frequency spectrum. If the model is in a chaotic mode (row **b**, stimulation period 105 ms and amplitude 0.48), the irregular movement of the AP manifests itself in the frequency spectrum as a continuous spectrum.

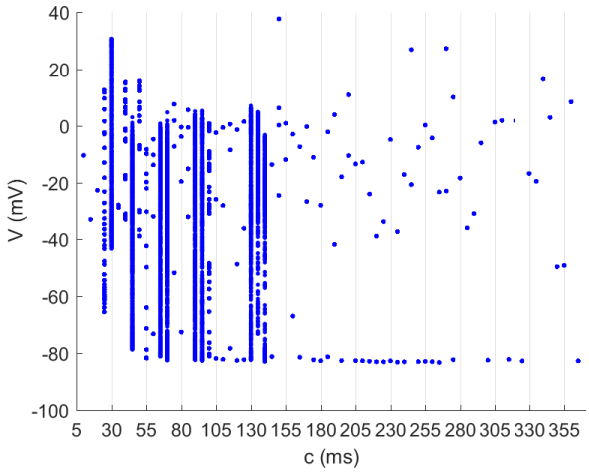

Figure 3.3: Bifurcation diagram of AP computed using BR model for $A = 80\ \mu\text{A/cm}^2$. AP snapshots are depicted in the bifurcation diagram, which is scanned at a rate equal to the stimulation period. In the case of the AP regular movement computed for the parameter c (see Figure 3.1), only isolated points are visible in the bifurcation diagram. Due to the irregular movement, the AP scanned at regular intervals always has a different value. For this reason, it is manifested In the diagram as a vertical line.

Chaotic responses of used models were confirmed using the 0-1 test for chaos. (see Figure 3.4). This figure shows the dependence of the action potential dynamic motion on the frequency and amplitude of the pacing current.

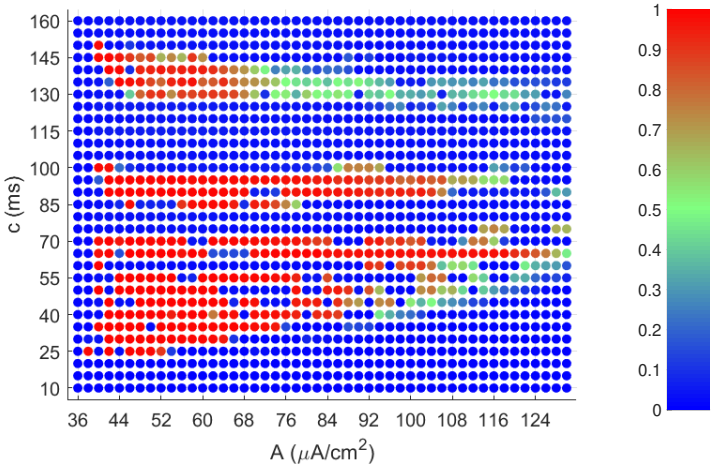

Figure 3.4: Results of the 0–1 test for chaos for AP, computed using the BR model, for all simulated amplitudes and frequencies of stimulation current. Values close to 0 (blue) indicate a regular time series. Results close to 1 (red) mark chaotic responses. If the results are not close to either of these values, the nature of the dynamic movement cannot be decided. In the figure, you can see dynamic motion's dependence on the stimulation's period and amplitude.

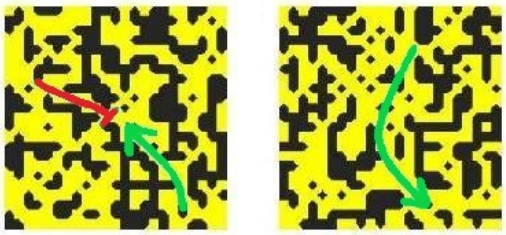

Figure 3.5: Pro-arrhythmic (left) and non-arrhythmogenic (right) fibrotic structure. Green arrows display the directions of successful AP propagation and the red flat arrowheads demonstrating conduction block.

3.2 Detection of potentially dangerous scars with neural networks

Researchers have proved the connection between scarring and arrhythmia in previous years. However, thanks to the complexity of the dynamics of cardiac electrical signalling, the effect of different arrangements of blockage on various arrhythmic consequences remain poorly understood.

In the following study (for detailed result description, please see paper [**TR.1.1**] which is enclosed in Chapter 4), the AP propagation impacted by fibrotic changes with various degrees was simulated. By simulations analysis, the percentage level of tissue affected by fibrosis was found, with the highest risk of emerging pathological re-entrant activation. A new set of simulations was then subsequently calculated, in which the tissue was always affected by fibrotic changes to the extent that re-entrant activation is most likely to occur. The sites initiating re-entrant activations patterns were found in the new data set. More precisely, the structures that selectively stop conduction by permitting conduction in one direction but not the other (unidirectional block) were detected. Figure 3.5 shows an example of this structure.

Then, the dataset of fibrotic structures that do and do not initiate re-entries was created by extracting the fibrotic structures around unidirectional blocks and non-blocking tissue. This dataset was used to train a neural network to classify whether the fibrotic structure causes a unidirectional block or not. This classification was performed for different sizes of fibrotic structures to determine to what extent re-entry initiation is predictable and over what spatial scale conduction heterogeneities appear to act to produce this effect. The classification accuracy is depicted in Figure 3.6. The results suggest that structural information within approximately 0.5mm (in the simulations, this spatial dimension is represented by a 9×9 grid) is sufficient to predict structures producing unidirectional blocks with more than 90% accuracy.

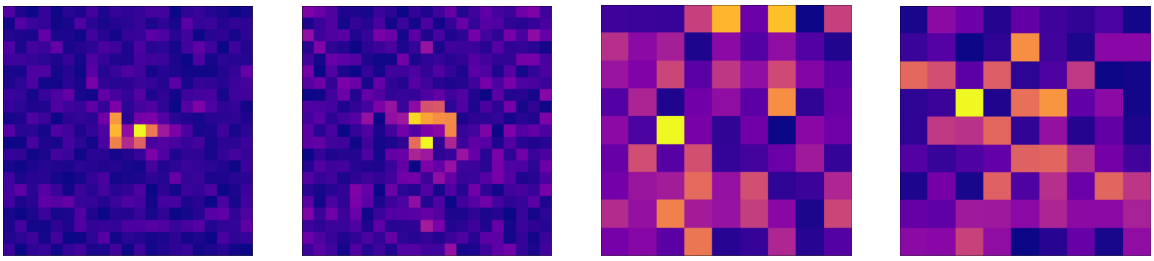

Figure 3.7: Example of saliency maps computed for larger (the first two from the left) and smaller fibrotic structures (last two from the left). The element's brightness indicates the site's overall importance for the classifier to decide whether this structure causes a unidirectional block. In the larger structure, it can be seen that the essential elements for the overall decision-making process are concentrated in the centre of the fibrotic structure. In the case of a small fibrotic structure, the total importance is evenly distributed.

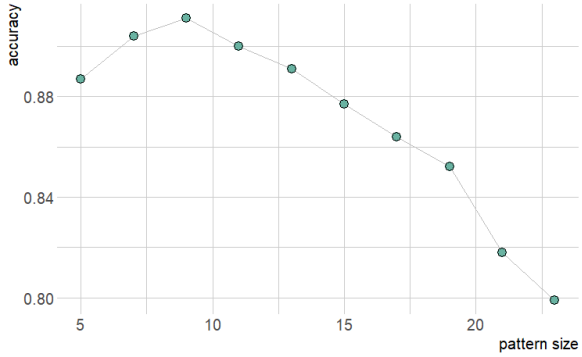

Figure 3.6: Graph of resulting accuracy dependence on structure size for two hidden layers and 1000 neurons.

The fact that these proarrhythmic phenomena take place on small spatial dimensions was also confirmed using saliency maps. These maps show the respective levels of contribution of the individual elements of a structure towards the resulting classification output by a NN. Saliency maps created for the classification of larger fibrotic structures showed a tendency to concentrate importance on a small central subsection of the larger micropatterns (Figure 3.7). This provides further evidence towards the conclusion that selective and unidirectional block events are governed by structure over only a small length scale.

Chapter 4

Fulltext of papers

Received <day> <Month>, <year>; | Revised <day> <Month>, <year>; | Accepted <day> <Month>, <year>

DOI: xxx/xxxx

SPECIAL ISSUE PAPER

Dynamical properties of the improved FK3V heart cell model

Radek Halfar*[1,2] | Marek Lampart[1,3]

[1]VŠB - Technical University of Ostrava, Department of Applied Mathematics, Czech Republic
[2]VŠB - Technical University of Ostrava, Department of Cybernetics and Biomedical Engineering, Czech Republic
[3]VŠB - Technical University of Ostrava, IT4Innovations, Czech Republic

Correspondence
*Radek Halfar, VŠB - Technical University of Ostrava, 17. listopadu 15/2172, 708 33 Ostrava, Czech Republic. Email: radek.halfar@vsb.cz

Present Address
VŠB - Technical University of Ostrava, 17. listopadu 15/2172, 708 33 Ostrava, Czech Republic.

Abstract

The main aim of this paper is to study the evolution of the transmembrane potential on the cardiac cell under different rates and amplitudes of stimulation. For modeling this potential, the modification of the Fenton-Karma model was applied. It is a phenomenological model with three degrees of freedom that corresponds to non-dimensional transmembrane potential and gating variables for regulation of inward and outward ion currents which can better reproduce the shape of the transmembrane potential than the original Fenton-Karma model. The model was newly forced by stimulus with the shape of the half-sine period. As the main goal of the paper is to show that this model is showing regular as well as irregular motion; periodic as well as chaotic patterns are detected using bifurcation diagrams, the Fourier spectra, Poincaré sections, and 0-1 test for chaos.

KEYWORDS:
cardiac cell model, bifurcation, Fourier spectra, 0-1 test for chaos

1 | INTRODUCTION

The cardiac electrophysiology is the result of complex processes occurring on the heart cell membranes, which aim to ensure the proper progression of cardiac action potential inherent in the heart muscle. The stability of the propagation of the action potential in the heart tissue is often examined parameter[1,2,3]. The ordered propagation of the action potential is essential for the proper functioning of the heart, and a life-threatening condition, such as ventricular fibrillation, may occur when the propagation is not correct. To understand the dynamic properties of propagation of the action potential, it is important to examine not only the entire tissue but also the dynamic properties of the individual cells from which it is created.

The three variable Fenton-Karma (FK3V) model is commonly used to describe heart electrophysiology. Studies that use this model can be generally divided into several groups. Studies dealing with the determination of model parameters to better replicate the outputs obtained by using physiological models or experimental data, studies that uses the FK3V model to study the electrophysiology of the heart, and studies that examine the characteristics of the FK3V model itself.

The first group can include, for example, the study published by Oliver and Krassowska[4], which describes a procedure for finding such parameters of the FK3V model to its restitution characteristics corresponding to the restitution characteristics of the Courtemanche-Ramirez Nattel model of atrial tissue. Lombardo et al.[5] edited the parameters of the detailed model and FK3V to fit for five clinical data of patients undergoing ablation therapy.

Another possible field of study is termination of fibrillation[6]. Objective of this paper is to numerically validate the experimental techniques for terminating fibrillation presented in Pak et al.[7] In his work, they found that the synchronized defibrillation can create a low-energy alternative to the traditional defibrillation. Allexandre and Otani[1] studied the electrophysiological and dynamic mechanism of spiral wave break up. The authors found several alternans unstable modes with different growth rates,

[0]**Abbreviations:** FK3V, Three variable Fenton-Karma

frequencies and spatial structures. In another study[8], the authors examined the behavior of fibers in the computing FK3V monodomain anisotropic model of re-entrant ventricular fibrillation.

Another topic, which is often targeted in individual work dealing with the FK3V model, is the description of properties of the model itself. One of these studies examines the steady state of the system[2]. Linear stability of these points and their response to external stimulation were examined.

In this work an improvement of the FK3V model is introduced to obtain a better shape of action potential. The dynamical properties of this improved FK3V model are analyzed in dependence on the stimulation frequencies and amplitudes. It is shown that for suitable choices of the system parameters the system is chaotic (irregular patterns are visible) as well as periodic (regular).

For this purpose, the 0-1 test for chaos was applied. The 0-1 test for chaos, a newly established test[9,10], gives a binary characteristic of motion's behavior. More precisely, this test returns 0 for regular (periodic) and 1 for irregular (chaotic) patterns. The mathematical background can be found in the article by Gottwald and Melbourne[11], Bernardini and Litak[12] or in the latest review[13]. This test is applicable on discrete dynamical systems[14], continuous dynamical systems[15] as well as on a real data represented as time series[16]. This test has been successfully used in many applications, for example, in distinguishing between chaos and randomness from a noisy data[17], exploration of mechanical system's dynamic properties consisting of a ball jumping between a movable baseplate and a fixed upper stop[18]. This test was also used for analysis of the nonlinear floating potential fluctuations from a glow discharge plasma[19], for tracing the presence of nonlinearity and chaos in wireless network traffic[20], for chaos detection of the partial discharge patterns[21], or traffic flows[22] .

The paper is organized as follows. In Section 2, the original FK3V model and its parameters are presented. Section 3 is dedicated to the model modification. In Section 4, the main results of this work are summarized. In particular, they include the phase portraits, Fourier spectra, and Poincaré section of the model results for various stimulation frequencies in Subsection 4.2, and test for chaos 0-1 for various stimulation frequencies and amplitudes in Subsection 4.3. The paper is closed by conclusions in Section 5.

2 | FK3V MODEL

The FK3V model is a dimensionless ionic model of cardiac action potential, which is based on the Luo-Rudy-I model. For reproducing action potential it uses three variables u, v, and w. Variable u represents the transmembrane potential (so that $u = 0$ and $u = 1$ are the rest and peak voltages, respectively). The transmembrane potential changes depending on ionic currents according to the following equation:

$$\dot{u} = J_{stim} - J_{fi} - J_{so} - J_{si} \tag{1}$$

where J_{fi} (accountable for depolarization of the membrane), J_{so} (accountable for repolarization of the membrane), and J_{si} (balances J_{so} during the plateau phase) are cross-membrane currents named fast inward (fi), slow outward (so), and slow inward (si) that roughly corresponds to sodium, potassium, and calcium ion currents, respectively. But because they do not represent the quantitatively measured currents but only their activation, inactivation, and reactivation, it is preferred to call these currents as fast and slow inward, and slow outward, rather than Na, Ca, and K as a reminder of these simplification. J_{stim} indicates the externally applied current. In this study, the external current composition of pulses is created by the first half period of sine function followed by zero function. J_{stim} is therefore defined by the following equation:

$$J_{stim} = \begin{cases} A\sin(t - n(c+1)) & t \in [n(c+1), n(c+1)+1] \ n \in \mathbb{N} \cup \{0\}, \\ 0 & t \notin [n(c+1), n(c+1)+1] \ n \in \mathbb{N} \cup \{0\}, \end{cases} \tag{2}$$

where c denotes the length of time interval between pulses and A stands for the amplitude. In Equation 1 $\dot{u}$ denotes the first derivative of u with respect to time. The cross membrane currents are given by

$$\begin{aligned} J_{fi}(u;v) &= \Theta(u-u_c)(1-u)(u-u_c)\frac{-v}{\tau_d}, \\ J_{so}(u) &= \Theta(u_c-u)\frac{u}{\tau_0} + \Theta(u-u_c)\frac{1}{\tau_r}, \\ J_{si}(u;w) &= \frac{-w(1+\tanh(k(u-u_c^{si})))}{2\tau_{si}}, \end{aligned} \tag{3}$$

where $\Theta(x)$ is the Heaviside function.
Another two variables v and w used in the model are gating variables which regulate inactivation of J_{fi}, and J_{so} takes the following form:

$$\dot{v} = \Theta(u_c - u)(1 - v)\frac{1}{\tau_v^-(u)} - \Theta(u - u_c)v\frac{1}{\tau_v^+}, \tag{4}$$

$$\dot{w} = \Theta(u_c - u)(1 - w)\frac{1}{\tau_w^-} - \Theta(u - u_c)w\frac{1}{\tau_w^+}, \tag{5}$$

$\tau_v(u)$ is a function for defining the time constants for two voltage ranges ($u_v < u < u_c$ and $u < u_v$) and is introduced for proper reproducing CV restitution curve. It controls reactivation of J_{fi} and is given by equation

$$\tau_v^-(u) = \Theta(u - u_v)\tau_{v_1}^- + \Theta(u_v - u)\tau_{v_2}^-$$

The model contains several constants, which are used for fitting the output curves into the requested shape, time constants τ_r, τ_{si}, τ_0, threshold potentials u_c, u_c^{si}, and u_v.
The original paper[3] describes four different sets of parameters to fit for different dataset.

- BR: obtained by stimuli of the Beeler-Reuter model with standard parameter values.
- MBR: obtained by stimuli of modified the Beeler-Reuter model with accelerated up calcium kinetic.
- MLBR-I: stimuli of Luo-Rudy-I model with speeded up calcium kinetic.
- GP: experimental data from measuring the membrane potentials on the epicardial surface of the left Ventricle of a guinea pig.

TABLE 1 Original published parameters of the FK3V model[3] for BR parametric set, $k = 10$

Parameter	Description	unit	value
τ_d	setting influence J_{fi} for $u > u_c$	ms	0.25
τ_r	setting influence J_{so} for $u > u_c$	ms	33
τ_{si}	setting influence J_{si} on $\dot{u}$	ms	30
τ_0	setting decrease u to 0 for $u < u_c$	ms	12.5
τ_v^+	setting decrease v to 0 for $u > u_c$	ms	3.33
$\tau_{v_1}^-$	setting value for $\tau_v^-(u)$ for $u > u_v$	ms	1250
$\tau_{v_2}^-$	setting value for $\tau_v^-(u)$ for $u < u_v$	ms	19.6
τ_w^+	setting decrease w to 0 for $u > u_c$	ms	870
τ_w^-	setting increase w to 1 for $u < u_c$	ms	41
u_c	depolarization threshold	-	0.13
u_v	threshold for activation $\tau_{v_1}^-$ or $\tau_{v_2}^-$	-	0.04
u_c^{si}	threshold for opening J_{si}	-	0.85

3 | MODEL MODIFICATION

Since the shape of FK3V model is not realistic, the modification of this model is proposed. The modification consists of replacing constant τ_r in Equation 3 by the following function

$$\tau_r(u) = \Theta(u_{\tau_r} - u)\tau_r + \Theta(u - u_{\tau_r})\Big(\frac{\tau_r(1 + \tanh(k_2(1 - u)))}{4} + \frac{\tau_r}{2}\Big). \tag{6}$$

This equation divides $\tau_r(u)$ into two potential ranges. From 0 to u_{τ_r} where $\tau_r(u)$ remains constant and from u_{τ_r} above, where u decreases from τ_r to $\tau_r/2$. Another parameter introduced in Equation 6 is k_2 which sets the speed of decrease of $\tau_r(u)$. In this

work $u_{\tau_r} = 0.85$ and $k_2 = 20$. Another change from the original model is redefining u_c^{si} to value $u_c^{si} = 0.7$. The rest of the parameters stay the same as in the original BR parameters set (see Table 1).

In Figure 1 , the difference in the shape of the transmembrane potential of the original FK3V model as well as the modified model can be seen.

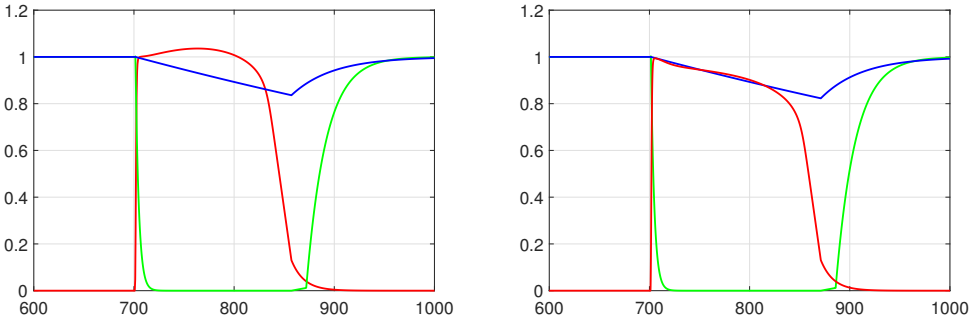

FIGURE 1 Time responses of u (red), v (green) and w (blue) of the original model (left) and improved model (right) for $c = 700$ ms and $A = 0.48$.

4 | MAIN RESULTS

In individual simulations, the heart cell was stimulated with the half-sine shaped current pulses with an amplitude from $A = 0.16$ to $A = 0.96$ with step of 0.04 and duration 1 ms. The individual stimulation pulses were separated by the delay c (see Equation 2). The computations were performed for the stimulation delays from 10 to 300 ms with step of 5 ms. Each simulation was done for the time from 0 to 5×10^5 ms. From the results, a phase diagram, amplitude frequency spectrum, and Poincaré section for each simulated frequency was computed. From the data was also created bifurcation diagram for the entire simulated frequency spectrum and the 0-1 test for chaos was computed.

4.1 | Phase portraits, the Fourier spectra, and Poincaré section

The Fourier spectra and phase portraits were computed for $A = 0.48$ (twice as needed to cause stimulation). Chaotic behavior of the model was observed on stimulation delays ranging from 30 to 50 ms and 105 ms. Regular behavior was observed elsewhere.

Cases with regular behavior can be divided into five groups (**RG1** – **RG5**). Each of these groups corresponds to the different biological response of the cell to the stimulatory pulses and corresponding representatives are shown in (Figure 2 – Figure 6); in all of these cases the Fourier spectra is formed by a number of harmonic frequencies, hence the frequency of the periodic trajectory is computable. Periodic motions of trajectories are also visible in Poincaré sections.

The irregular (chaotic) case is shown in Figure 7 , the **IRG** case. In this case, the Fourier spectra is formed by a number of harmonic components having the basic, super-harmonic, sub-harmonic, and combination frequencies on which there are superposed further motions with frequencies forming the sided bands of the dominant frequencies. Their mutual ratio indicates the irregularity of the motion. The character of this motion's case is underlined by the Poincaré section.

RG1 This case is represented in Figure 2) for stimulation delay 20 ms. The amplitude of u does not reach the full range (0 to 1), but changes only between 0 and 0.34. The action potential shape (variable u) also does not match with proper shape of action potential (see Figure 1 for comparsion).

RG2 At stimulation delays from 75 ms to 100 ms, stimulation causes every third stimulus (two unsuccessful stimulation followed by successful pacing). In the phase diagram, a closed loop with two spikes due to unsuccessful stimulation can be seen. The representative case of the model with this behavior can be seen in Figure 3 .

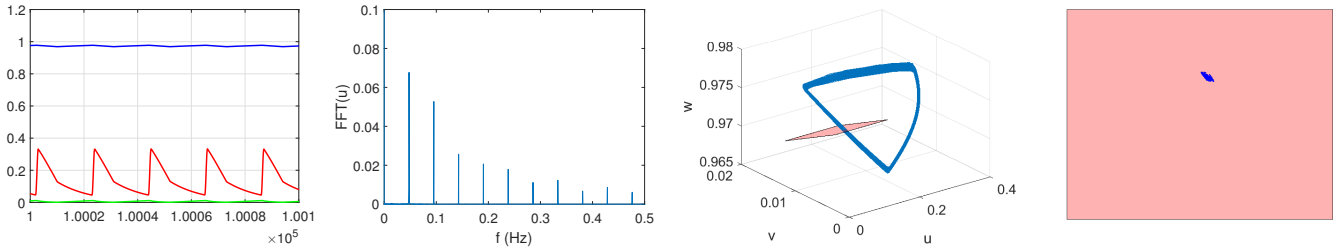

FIGURE 2 From the left: time responses of u (red), v (green), and w (blue); FFT of variable u; phase diagram and Poincaré section of the modified FK3V model for $c = 20$ ms.

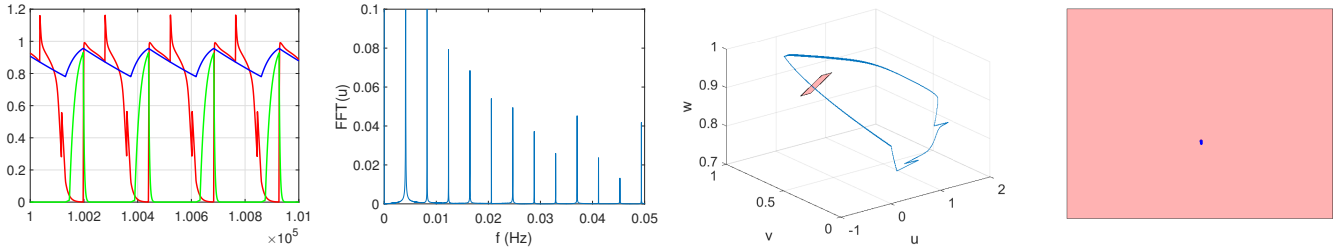

FIGURE 3 From the left: time responses of u (red), v (green), and w (blue); FFT of variable u; phase diagram and Poincaré section of the modified FK3V model for $c = 80$ ms.

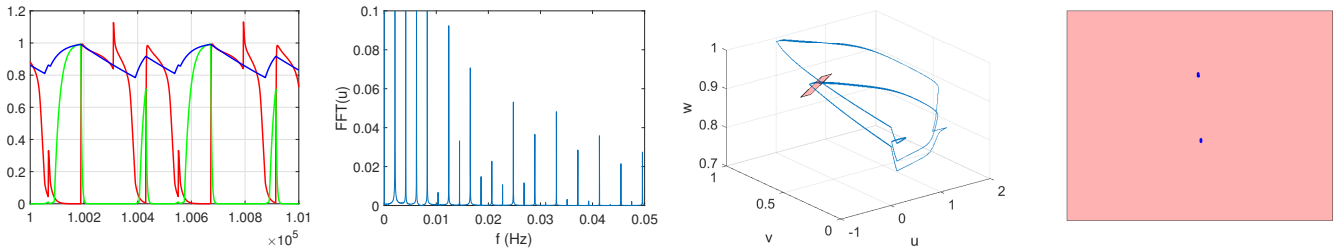

FIGURE 4 From the left: time responses of u (red), v (green), and w (blue); FFT of variable u; phase diagram and Poincaré section of the modified FK3V model for $c = 120$ ms.

RG3 In Figure 4 , the typical model response for the delays ranging from 110 ms to 145 ms can be seen. The relevant stimulation is caused by every second stimulation impulse, but every second successful stimulation comes to phase of relative refracterity, therefore the action potential of this stimulation has shorter duration than the action potential of the previous successful stimulation impulse. In the phase portrait, two spikes from unsuccessful stimulation and two curves from the stimulation (one comes from the phase of relative refracterity and one comes from steady state) can be seen.

RG4 In Figure 5 , the representative case, every second stimulation impulse causes stimulation at delays from 150 ms to 185 ms. The action potential duration is about 200 ms.

RG5 Finally, in Figure 6 , the representative is shown where every stimulation impulse causes stimulation; this is observable for delays from 190 ms and above.

IRG The behavior of motions observed on delays from 30 ms to 50 ms and 105 ms is irregular, the representative can be seen in Figure 7 . In this case, the mutual ratio of stimulation impulse and stimulation indicates the irregularity of the motion. Moreover, these cases are chaotic due to the output of the 0-1 test for chaos performed in 4.3 Section.

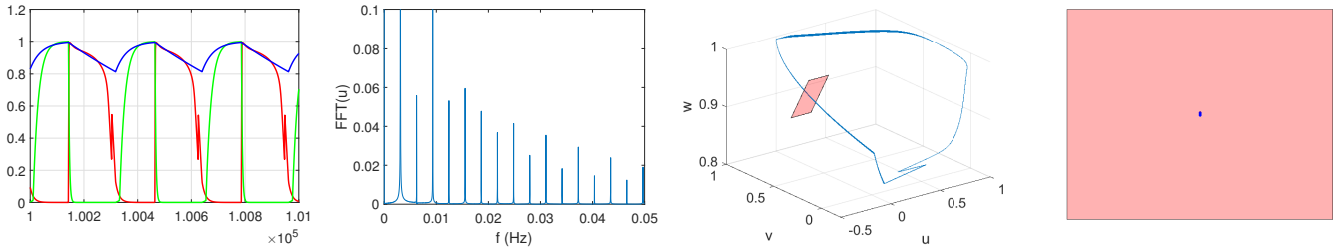

FIGURE 5 From the left: time responses of u (red), v (green), and w (blue); FFT of variable u; phase diagram and Poincaré section of the modified FK3V model for $c = 160$ ms.

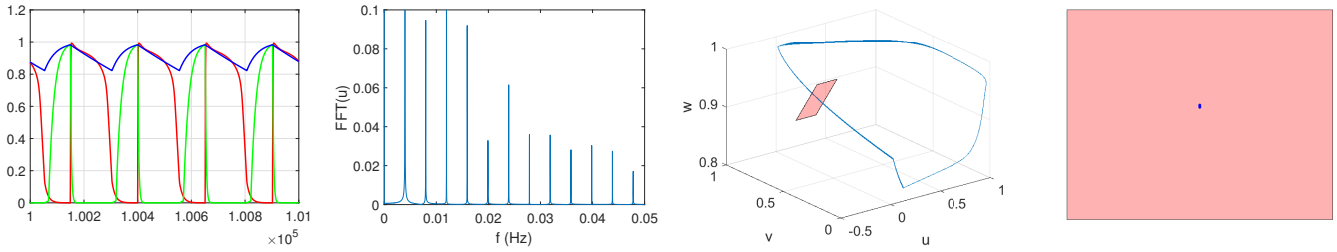

FIGURE 6 From the left: time responses of u (red), v (green), and w (blue); FFT of variable u; phase diagram and Poincaré section of the modified FK3V model for $c = 250$ ms.

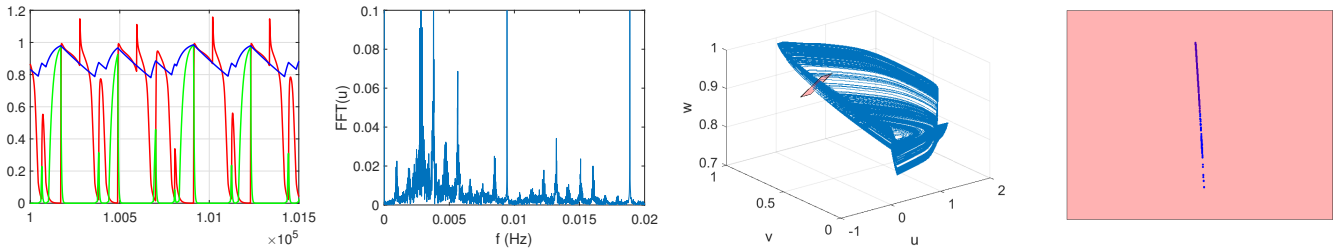

FIGURE 7 From the left: time responses of u (red), v (green), and w (blue); FFT of variable u; phase diagram and Poincaré section the modified FK3V model for $c = 105$ ms.

4.2 | Bifurcation diagram

Next work was to plot bifurcation diagrams of modified FK3V model. Values for diagrams was collected witch period of stimulation frequency. Diagrams can be seen in Figure 8 . In diagrams can be seen, that stimulation delays from 30 to 50 ms and 105 ms are chaotic, at the other delays are regular responses. This coincides with time series exploration.

4.3 | The 0-1 test for chaos

Next, the 0-1 test for chaos was performed[9,10]. This test is used to distinguish regular and chaotic dynamics. It works with the time series and does not need any phase space reconstruction. The resulting value of this test can only be 0 (regular behavior) or 1 (chaos). This correlation method works as follows. For a given set of observations $\phi(j)$ for $j \in \{1, 2, \dots, N\}$ are computed translation variables for suitable choice of $b \in (0, 2\pi)$.

$$p_b(n) = \sum_{j=1}^{N} \phi(j) \cos(jb) = 1,$$

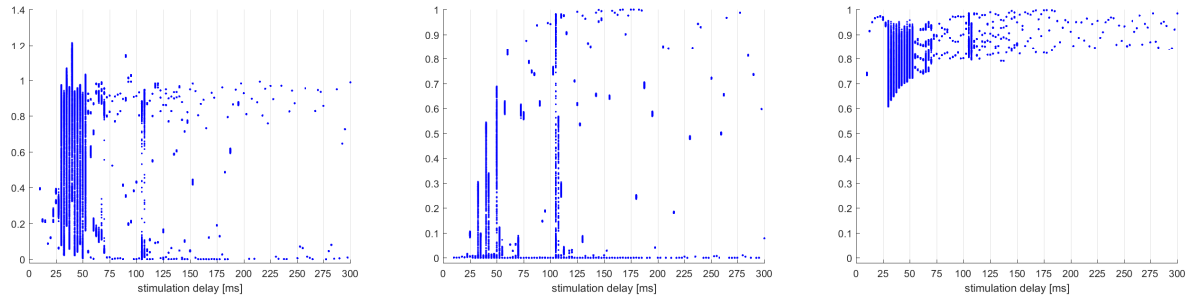

FIGURE 8 Bifurcation diagram for variable u (left), v (middle), and w (right).

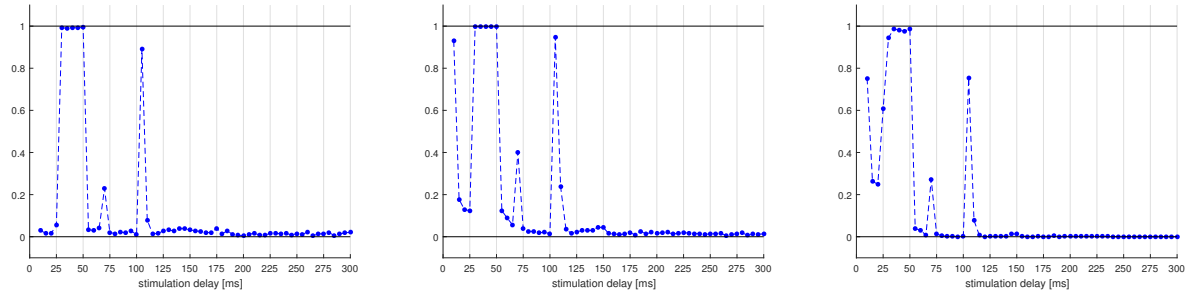

FIGURE 9 Results of the 0-1 test for chaos for $A = 0.48$ and c from 10 ms to 300 ms. Variable u (left), v (middle) and w (right).

$$q_b(n) = \sum_{j=1}^{N} \phi(j) \sin(jb) = 1,$$

then the mean square displacement is computed using the following equation

$$M_b(n) = \lim_{N\to\infty} \frac{1}{N} \sum_{j=1}^{N} [p_b(j+n) - p_b(j)]^2 + [q_b(j+n) - q_b(j)]^2$$

here $n \leq n_{cut}$ where $n_{cut} \ll N$. Then, the estimate of the modified mean square displacement is computed using the next equation

$$D_b(n) = M_b(n) - \left(\lim_{N\to\infty} \frac{1}{N} \sum_{j=1}^{N} \phi(j) \right)^2 \frac{1-\cos(nb)}{1-\cos(b)}.$$

Finally, the output of the 0-1 test is obtained as correlation coefficient of ξ and Δ for fixed parameter b

$$K_b = \mathrm{corr}(\xi, \Delta)$$

where $\xi = (1, 2, \ldots, n_{cut})$ and $\Delta = (D_c(1), D_c 2, \ldots, D_c(n_{cut}))$. Hence, K_b is dependent on the choice of c. To get K as the output of the 0-1 test, as limiting value of all K_b, the result value is taken as

$$K = \mathrm{median}(K_b).$$

The results of this test can bee seen in Figure 9 . At delays up to 25 ms, the behavior of variable u is regular, but for variables v and w , it cannot be decided if the behavior is chaotic or regular. Chaotic behavior of the model was observed on stimulation delays from 30 to 50 ms and 105 ms. There are also several cases of stimulation delays with the output of the 0-1 test for chaos in the range (0.1,0.9); in this cases it cannot be decided if it is chaotic or regular behavior, e.g. at the stimulation delay of 70 ms. Notice, that results of this test coincides with time series and bifurcation diagram.

But because of that, the stimulation of heart cell is dependent not only on the stimulation frequency but also on the amplitude of stimulation, the test for chaos 0-1 was computed also for the amplitude range from 0.16 to 0.96 in step 0.04. But since the results of the test for chaos 0-1 for $A = 0.48$ was the regular behavior for $c > 105$ ms (see Figure 9), the tests were computed

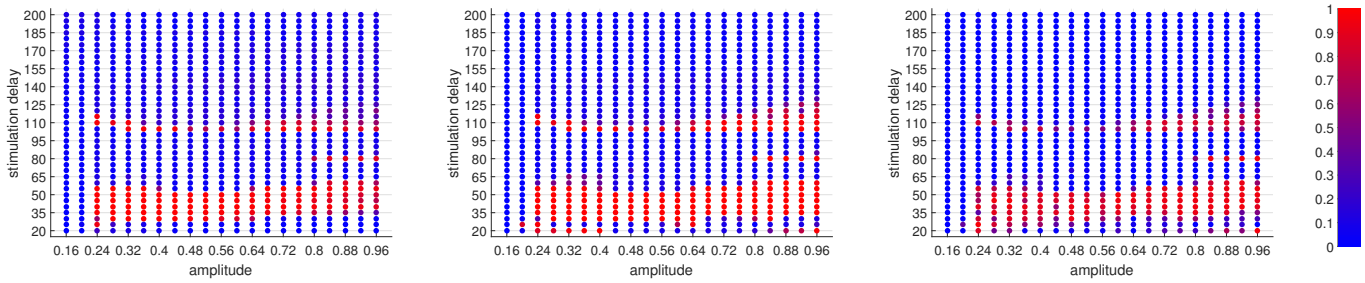

FIGURE 10 Results of the test for chaos 0-1 for various stimulation delays and amplitudes for variable (from the left) u, v, w and color bar (right).

for the stimulation delays from $c = 20$ ms to $c = 200$ ms in 5 ms increments. The results of this test can be seen in Figure 10 . From this figure can be seen that chaotic behavior is focused into three regions.

The first and biggest region of the chaotic behavior is at amplitudes from 0.24 above and stimulation delays from approximately 30 ms to 55 ms. Another area of section of chaotic behavior is at amplitudes from 0.8 and above and stimulation delay 80 ms. And the last region of chaotic behavior is at stimulation delay around $c = 105$ ms and amplitudes from $A = 0.24$.

5 | CONCLUSIONS

In this paper, the Fenton-Karma model of cardiac cell was improved and its dynamics was analyzed in detail with respect to the amplitude A and stimulation delays c. The model (1, 4, 5) was forced by stimulus with the shape of half-sine period. The equations of potentials were solved numerically using the Runge-Kutta method of the fourth order implemented as *ode45* solver in Matlab. It was observed that the model is showing regular (see, e.g., Figures 3 and 6) as well as irregular patterns (see Figure 7) for different range of stimulation delay and amplitude. For detection of this movements character, the Fourier spectra, Poincaré sections, and bifurcation diagrams (Figure 8) were used. Chaotic behavior of variables u, v, and w were confirmed by the 0-1 test for chaos (Figures 10), for suitable choices of stimulation delays and amplitudes.

ACKNOWLEDGEMENTS

This work was supported by The Ministry of Education, Youth and Sports from the National Programme of Sustainability (NPU II) project “IT4Innovations excellence in science - LQ1602“; by The Ministry of Education, Youth and Sports from the Large Infrastructures for Research, Experimental Development and Innovations project “IT4Innovations National Supercomputing Center – LM2015070“; by the project SV4507741/2101, ’Biomedicínské inženyrské systémy XIII’. The Czech Science Foundation (GACR) No. 17-03037S, Investment evaluation of medical device development; by grants SGS No. SP2017/122 VŠB - Technical University of Ostrava, Czech Republic; and by the Czech Science Foundation grant No. P103/15/06700S.

References

1. Allexandre D, Otani N. Preventing alternans-induced spiral wave breakup in cardiac tissue: An ion-channel-based approach. *Phys. Rev. E.* 2004;70.

2. Jacquemet V. Steady-state solutions in mathematical models of atrial cell electrophysiology and their stability. *Mathematical Biosciences.* 2007;208:241–269.

3. Fenton F, Karma A. Vortex dynamics in three-dimensional continuous myocardium with fiber rotation: Filament instability and fibrillation. *Chaos: An Interdisciplinary Journal of Nonlinear Science.* 1998;8:20–47.

4. Oliver R, Krassowska W. Reproducing cardiac restitution properties using the Fenton-Karma membrane model. *Annals of Biomedical Engineering.* 2005;33:907–911.

5. Lombardo D, Fenton F, Narayan S, Rappel W. Comparison of detailed and simplified models of human atrial myocytes to recapitulate patient specific properties. *PLOS Computational Biology.* 2016;12:1–15.

6. Puwal S, Roth B. Numerical simulations of synchroniyed pacing. *Journal of Biological Systems.* 2006;14:101–112.

7. Pak H, Liu Y, Hayashi H, Okuyama Y, Chen P, Lin S. Synchronization of ventricular fibrillation with real-time feedback pacing: implication to low-energy defibrillation. *American Journal of Physiology - Heart and Circulatory Physiology.* 2003;285.

8. Clayton RH, Holden AV. Filament behavior in a computational model of ventricular fibrillation in the canine heart. *IEEE Transactions on Biomedical Engineering.* 2004;51:28–34.

9. Gottwald A, Melbourne I. A new test for chaos in deterministic systems. *Proc. R. Soc. London A.* 2004;460:603–611.

10. Gottwald A, Melbourne I. On the implementation of the 0-1 test for chaos. *SIAM J. Appl. Dyn.*. 2009;8:129–145.

11. Gottwald Georg A, Melbourne Ian. On the validity of the 0-1 test for chaos. *Nonlinearity.* 2009;22(6):1367.

12. Bernardini Davide, Litak Grzegorz. An overview of 0–1 test for chaos. *Journal of the Brazilian Society of Mechanical Sciences and Engineering.* 2015;38(5):1433–1450.

13. Gottwald Georg A., Melbourne Ian. The 0-1 Test for Chaos: A Review. In: Springer Berlin Heidelberg 2016 (pp. 221–247).

14. Lampart Marek, Martinovič Tomáš. A survey of tools detecting the dynamical properties of one-dimensional families. *Advances in Electrical and Electronic Engineering.* 2017;15(2):304-313.

15. Melosik M., Marszalek W.. On the 0/1 test for chaos in continuous systems. *Bulletin of the Polish Academy of Sciences Technical Sciences.* 2016;64(3).

16. Falconer Ian, Gottwald Georg A., Melbourne Ian, Wormnes Kjetil. Application of the 0-1 Test for Chaos to Experimental Data. *SIAM Journal on Applied Dynamical Systems.* 2007;6(2):395-402.

17. Kulp Christopher W., Smith Suzanne. Characterization of noisy symbolic time series. *Phys. Rev. E.* 2011;83:026201.

18. Lampart Marek, Zapoměl Jaroslav. Dynamical properties of a non-autonomous bouncing ball model forced by non-harmonic excitation. *Mathematical Methods in the Applied Sciences.* 2016;39(16):4923–4929. mma.4186.

19. R. Chowdhury D, N. S. Iyengar A, Lahiri S. Gottwald Melborune (0-1) test for chaos in a plasma. 2012;19:53-56.

20. Mukherjee Somenath, Ray Rajdeep, Samanta Rajkumar, Khondekar Mofazzal H., Sanyal Goutam. Nonlinearity and chaos in wireless network traffic. *Chaos, Solitons & Fractals.* 2017;96:23 - 29.

21. Lampart Marek, Vantuch Tomáš, Zelinka Ivan, Mišák Stanislav. Dynamical properties of partial-discharge patterns. *International Journal of Parallel, Emergent and Distributed Systems.* 2017;0(0):1-16.

22. Martinovič Tomáš. Chaotic behaviour of noisy traffic data. *Mathematical Methods in the Applied Sciences.* 2016;:n/a–n/a. mma.4234.

INTERNATIONAL JOURNAL OF COMPUTER MATHEMATICS
https://doi.org/10.1080/00207160.2019.1649662

Taylor & Francis
Taylor & Francis Group

ARTICLE

Dynamical properties of Beeler–Reuter cardiac cell model with respect to stimulation parameters

R. Halfar [a,b]

[a]Department of Cybernetics and Biomedical Engineering, VŠB – Technical University of Ostrava, Ostrava, Czech Republic; [b]IT4Innovations, VŠB – Technical University of Ostrava, Ostrava, Czech Republic

ABSTRACT

The Beeler–Reuter model is one of the oldest models of the cardiac ventricular cell. This model is used in many scientific studies that investigate the propagation of the action potential. In this paper, dynamical properties of Beeler–Reuter model with respect to the frequency and amplitude of the stimulus pulse with the shape of the half-sine period are being investigated. For this purpose bifurcation diagrams, the Fourier spectra, and the 0–1 test for chaos was applied.

ARTICLE HISTORY
Received 31 July 2018
Revised 1 March 2019
Accepted 4 April 2019

KEYWORDS
Beeler–Reuter model; cardiac cell; chaos; bifurcation; Fourier spectra; the 0–1 test for chaos

2010 MATHEMATICS SUBJECT CLASSIFICATIONS
37N30; 34H10; 34H20; 92B05; 92C30

1. Introduction

One of the most dangerous conditions in which the human heart may be present is ventricular fibrillation. This state corresponds to spatiotemporal chaos [16] and can result in sudden death. This paper provides an insight into the dynamical properties of the human heart cell trough investigating Beeler–Reuter model (BR) of the cardiac ventricular cell. It is shown that even in the single cardiac cell can periodic pacing results in chaotic motions of action potential such as in ventricular fibrillation and the resulting motion dependent not only to pacing frequency but also to its amplitude.

BR is a well-established model that has been used since its publication in many scientific studies to elucidate the function of the ventricular cardiac cell and propagation of an action potential (AP). As an example of such a study [6–8,10,12,13] can be mentioned. In [6], responses of the BR model to sinusoidal stimulation are studied. The authors found the periodic as well as chaotic responses of the model to sinus stimulation. For detection of chaotic behaviour, Fast Fourier transform, and Lyapunov exponents were used. In paper [8], simulation of the effects of periodic stimulation on a strand of ventricular muscle is provided. Authors used one dimensional BR and by computing the Lyapunov exponent, bifurcation diagram, the return map, and cobweb diagram found chaotic, as well as periodic motions. In article [7], electrical excitation in a ring of cells described by the Noble, Beeler–Reuter, Luo–Rudy I, and third-order simplified mathematical models are studied. The researchers who used shortening the ring length managed the transition from steady-state circulation to quasiperiodicity. After that, restitution curve of the action potential duration (APD) becomes a double-valued function

CONTACT R. Halfar radek.halfar@vsb.cz Department of Cybernetics and Biomedical Engineering, VŠB – Technical University of Ostrava, Ostrava, Czech Republic; IT4Innovations, VŠB – Technical University of Ostrava, 17. listopadu 15/2172, 708 33 Ostrava, Czech Republic

placed under the APD restitution curve of an isolated cell. Investigation of origin of quasiperiodicity which opens the way to fibrillation (as a form of spatiotemporal chaos) by studying reentrant excitation in a ring of cardiac cells described by BR can be found in study [10]. Paper [13] provides a control scheme for preventing oscillatory instability arising from electrical waves circulating around a hurdle in cardiac tissue. In article [12], Beeler–Reuter and Luo–Rudy model are used for the study of cardiac tissue anisotropy and its role in the breakup of vortex filaments.

Despite the fact that this model was published more than 40 years ago, it is still being used today. Use of this model in recent years is demonstrated in [2,3,14]. In paper [14] the authors analysed the statistical mechanical properties of sustained ventricular fibrillation. For this purpose, the two-dimensional Beeler–Reuter–Drouhard–Roberge model was used. Researchers in the article [2] used the monodomain formulation of the Beeler–Reuter cell model on insulated tissue fibres for studying spatiotemporal effects of a space-fractional model in cardiac electrophysiology. Study [3] deals with finding individualized parameters for complex electrophysiological models. The authors placed a population of models approach within a statistical framework and created an algorithm based on sequential Monte Carlo. The algorithm has been compared with Latin hypercube sampling. For this comparison, the authors used the Beeler–Reuter cardiac electrophysiological model in the presence of a drug block.

This paper is organized as follows. In Section 2, the Beeler–Reuter model and its parameters are introduced. In Section 3, the main results of this work are summarized. In particular, they include the time series, phase portraits, and Fourier spectra of BR for various stimulation frequencies in Section 3.1, the bifurcation diagram in Section 3.2, and the 0–1 test for chaos in Section 3.3. The paper is closed by the conclusions in Section 4.

2. Beeler–Reuter model

The Beeler–Reuter model of the cardiac cell proposed by Beeler and Reuter in 1977 [1] is established by eight equations (see Equations (1)) defining the time derivatives of transmembrane potential V_m in mV, intracellular Ca^{2+} concentration $[Ca]_i$ in mole/l, and six dimensionless gating variables $x_1, m, h, j, d,$ and f. Gating variables are in Equations (1) modelled as variable y (difference in equations for gating variables is given by constants defined in Appendix 1 in Table A3).

$$\begin{aligned} \frac{\mathrm{d}V_m}{\mathrm{d}t} &= \frac{i_{\text{ext}} - i_{k_1} - i_{x_1} - i_{\text{Na}} - i_{\text{Ca}}}{C_m}, \\ \frac{\mathrm{d}[Ca]_i}{\mathrm{d}t} &= -10^{-7} i_{\text{s}} + 0.07(10^{-7} - [Ca]_i), \\ \frac{\mathrm{d}y}{\mathrm{d}t} &= \frac{y_\infty - y}{\tau_y}. \end{aligned} \tag{1}$$

Times t and τ are in ms. Parameter C_m defines membrane capacitance in $\mu\text{F/cm}^2$ (in this study $C_m = 1$). Ionic currents are described in Appendix 1 in Table A1. All currents are in the units of $\mu\text{A/cm}^2$. Definition of this currents are given by Equations (2).

$$\begin{aligned} i_{k_1} &= 0.35 \left(4 \frac{e^{0.04(V_m+85)} - 1}{e^{0.08(V_m+53)} + e^{0.04(V_m+53)}} + 0.2 \frac{V_m + 23}{1 - e^{-0.04(V_m+23)}} \right) \\ i_{x_1} &= x_1 0.8 \frac{e^{0.04(V_m+77)} - 1}{e^{0.04(V_m+35)}} \\ i_{\text{Na}} &= (\overline{g_{\text{Na}}}\, m^3\, h\, j + g_{\text{NaC}})(V_m - E_{\text{Na}}) \\ i_{\text{s}} &= \overline{g_{\text{s}}}\, \mathrm{d}\, f\, (V_m - E_{\text{s}}). \end{aligned} \tag{2}$$

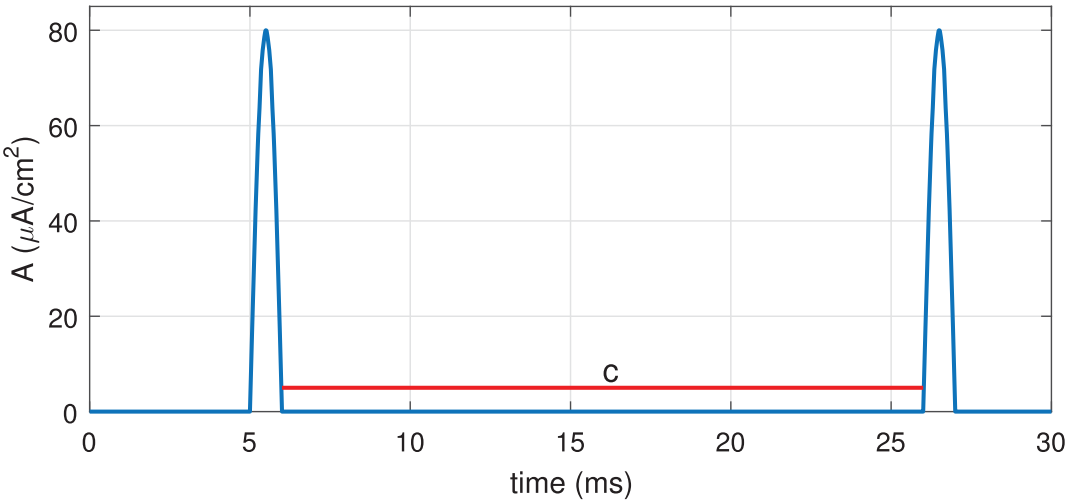

Figure 1. (Color online) Stimulation function i_{ext} for $A = 80\ \mu\text{A/cm}^2$, and $c = 20$ ms. Parameter c is labelled by red colour.

In these equations, parameter E defines voltages and g expresses conductances. The definition of these parameters used in this study is given in Appendix 1 in Table A2. Variable E_s is defined by the following equation:

$$E_s = -82.3 - 13.0287 \ln[Ca]_i.$$

Parameters τ_y and y_∞ used in Equations (1) are given by:

$$\begin{aligned} \tau_y &= \frac{1}{\alpha_y + \beta_y}, \\ y_\infty &= \frac{\alpha_y}{\alpha_y + \beta_y}. \end{aligned} \tag{3}$$

Rate constants α_y and β_y used in Equations (3) are given by:

$$\alpha_y, \beta_y = \frac{C_1 e^{C_2(V_m + C_3)} + C_4(V_m + C_5)}{e^{C_6(V_m + C_3)} + C_7}. \tag{4}$$

The constants used in this equation are summarized in Appendix 1 in Table A3.

In this study, the externally applied current i_{ext} are impulses with a duration of 1 ms created by the first half period of the sine function followed by the zero function. Variable i_{ext} is therefore defined by the following equation:

$$i_{\text{ext}} = \begin{cases} A \sin(\pi(t - n(c+1))), & t \in [n(c+1), n(c+1)+1], \quad n \in \mathbb{N} \cup \{0\}, \\ 0, & t \notin [n(c+1), n(c+1)+1], \quad n \in \mathbb{N} \cup \{0\}. \end{cases} \tag{5}$$

The graphical representation of Equation (5) can be seen in Figure 1.

3. Main results

In individual simulations, the heart cell was paced by stimulation current with an amplitude A from 36 to 130 $\mu\text{A/cm}^2$ with the step of 2 $\mu\text{A/cm}^2$ and duration 1 ms. The individual stimulation pulses were separated by delay c (see Equation (5) and Figure 1)). The computations were performed for the stimulation delays c from 10 to 365 ms with the step of 5 ms. Each simulation was done for the time from 0 to 5×10^5 ms. From the results, a variable named normalized model output (NMO)

was created. This output was computed by calculating the module from the resulting variables that have been modified to have zero mean and unit variance (see Equation (6)). This variable is used to investigate the behaviour of the model as a whole.

$$\mathrm{NMO} = \sqrt{\left(\frac{V_m - \mathrm{E}(V_m)}{\sqrt{\mathrm{var}(V_m)}}\right)^2 + \left(\frac{[Ca]_i - \mathrm{E}([Ca]_i)}{\sqrt{\mathrm{var}([Ca]_i)}}\right)^2 + \sum_{j=1}^{6}\left(\frac{y_j - \mathrm{E}(y_j)}{\sqrt{\mathrm{var}(y_j)}}\right)^2}. \tag{6}$$

From these values and also from the AP (variable V_m), amplitude frequency spectrum using Fast Fourier transform (FFT) for amplitude $A = 80\,\mu\mathrm{A/cm}^2$ and each simulated frequency was computed as well as the phase diagram was created. Since BR has 8 state variables, for the purpose of creating phase portrait gating variables x_1, m, h, j, d, and f was mapped into $\mathbb{R}$ using the following equation:

$$\mathrm{NGO} = \frac{x_1 + m + h + j + d + f - E(x_1 + m + h + j + d + f)}{\sqrt{\mathrm{var}(x_1 + m + h + j + d + f)}}.$$

Next, the bifurcation diagram for the entire simulated frequency spectrum was created and the 0–1 test for chaos was computed for the entire simulated frequency and amplitude spectrum.

3.1. Phase portraits and the Fourier spectra

Chaotic behaviour of the model was observed on stimulation delays $c \in \{45\} \cup [65, 70] \cup [90, 95] \cup [130, 140]$. Regular behaviour was observed elsewhere. The cases with regular behaviour can be divided into five groups (**RG1**–**RG5**). Each of these groups corresponds to the different biological response of the cell to the stimulation pulses and corresponding representatives are shown in Figures 2–6. In all of these cases, the Fourier spectra are formed by a number of harmonic frequencies, hence the frequency of the periodic trajectory is computable.

The irregular (chaotic) case is shown in Figure 7, the **IRG** case. In this case, the Fourier spectra are formed by a number of harmonic components having the basic, super-harmonic, sub-harmonic, and combination frequencies on which superposed further motions with frequencies forming the sided bands of the dominant frequencies are. Their mutual ratio indicates the irregularity of the motion.

RG1 This case can be seen for stimulation delays $c \in [10, 20] \cup \{35\}$ ms. BR adapts to the stimulation delay (parameter c), and the output is a saw-shaped signal with insufficient amplitude. An example of this behaviour is depicted in Figure 2.

RG2 For $c \in [25, 30]$ ms stimulation occurs, but the action potential is superimposed on a saw-signal with the frequency corresponding to pacing frequency. These two signals can be seen in the phase portrait. These results can be seen in Figure 3.

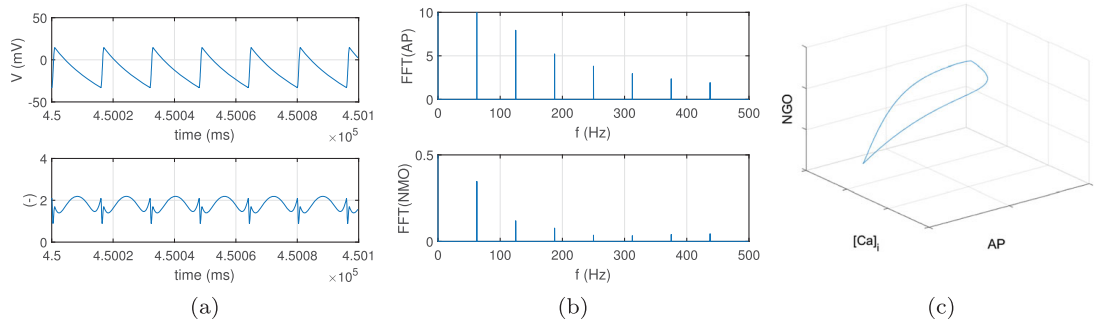

Figure 2. BR responses for $A = 80\,\mu\mathrm{A/cm}^2$ and $c = 15$ ms. (a) Time responses of AP (up) and NMO (below). (b) FFT of AP (up) and NMO (below). (c) Phase diagram of BR.

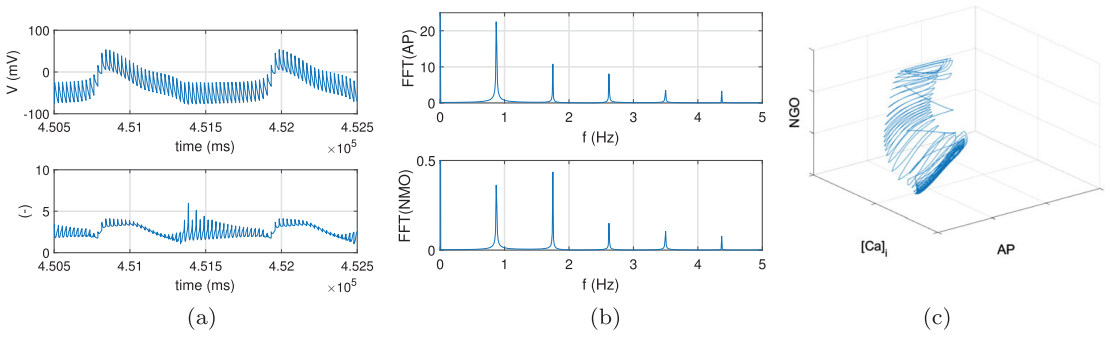

Figure 3. BR responses for $A = 80\,\mu A/cm^2$ and $c = 25$ ms. (a) Time responses of AP (up) and NMO (below). (b) FFT of AP (up) and NMO (below). (c) Phase diagram of BR.

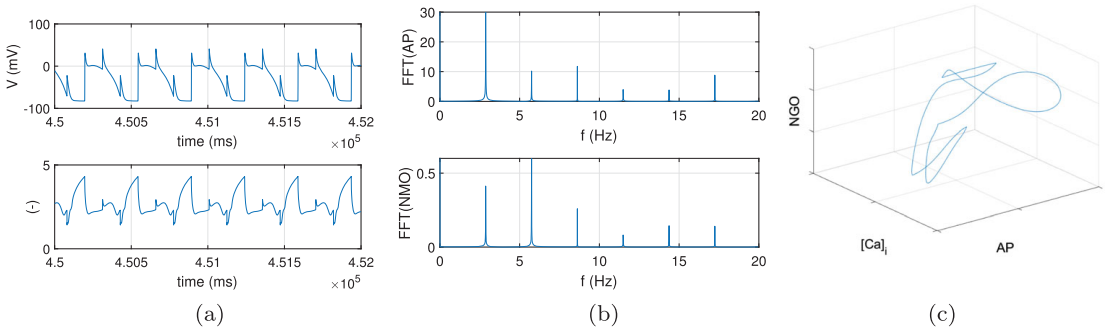

Figure 4. BR responses for $A = 80\,\mu A/cm^2$ and $c = 115$ ms. (a) Time responses of AP (up) and NMO (below). (b) FFT of AP (up) and NMO (below). (c) Phase diagram of BR.

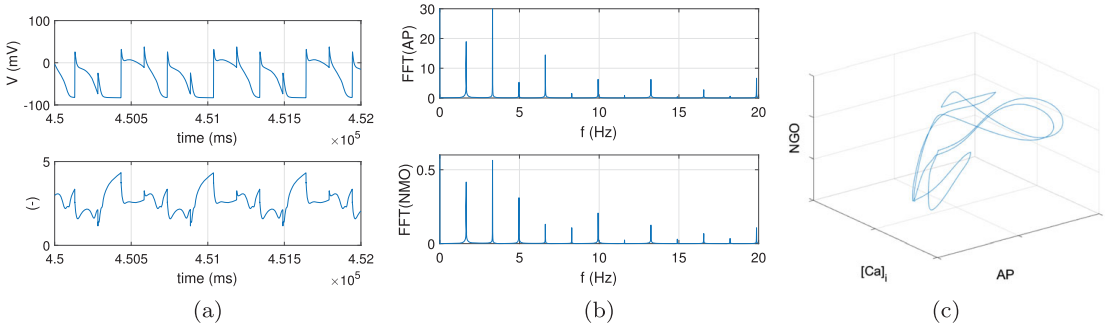

Figure 5. BR responses for $A = 80\,\mu A/cm^2$ and $c = 150$ ms. (a) Time responses of AP (up) and NMO (below). (b) FFT of AP (up) and NMO (below). (c) Phase diagram of BR.

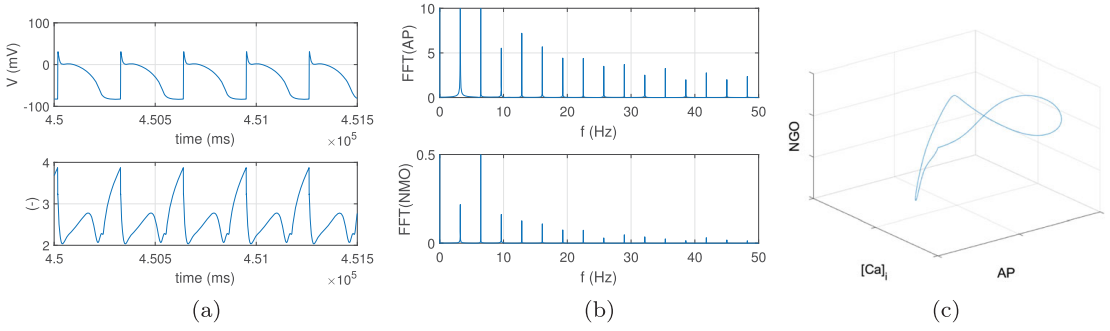

Figure 6. BR responses for $A = 80\,\mu A/cm^2$ and $c = 310$ ms. (a) Time responses of AP (up) and NMO (below). (b) FFT of AP (up) and NMO (below). (c) Phase diagram of BR.

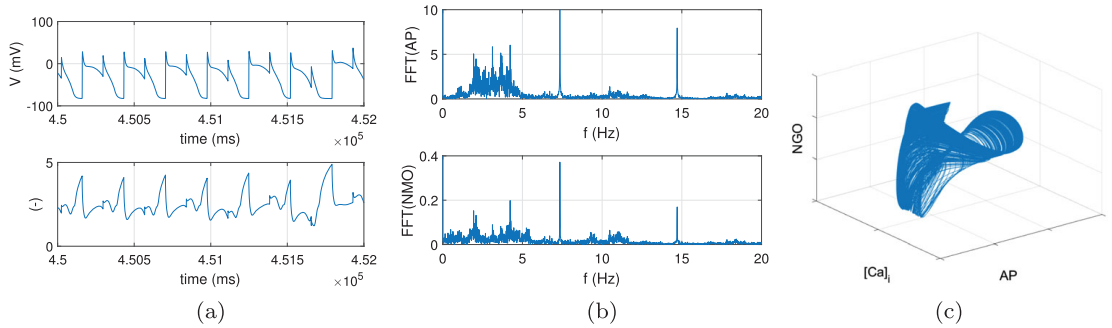

Figure 7. BR responses for $A = 80\,\mu A/cm^2$ and $c = 135$ ms. (a) Time responses of AP (up) and NMO (below). (b) FFT of AP (up) and NMO (below). (c) Phase diagram of BR.

RG3 For stimulation delay $c \in \{40, 60\} \cup [75, 80] \cup [105, 125] \cup \{145\} \cup [155, 275]$ successful stimulation with spikes caused by unsuccessful stimulation pulse can be seen. The number of unsuccessful stimulus pulses is dependent on c. The representative of this behaviour is shown in Figure 4.

RG4 In Figure 5, the typical model response for delay $c \in [50, 55] \cup \{85, 100, 150\}$ ms can be seen. The cell stimulation in these cases comes from the relative refractory period and also from the steady state. The action potential that came from a relative refractory period has a shorter duration and smaller amplitude than the AP from steady state. In the phase portrait, two curves can be seen (one comes from the phase of the relative refractory period and one comes from steady state).

RG5 For stimulation delay $c \in [280, 365]$ every pacing impulse cause stimulation that comes from the steady state. This behaviour can be seen in Figure 6.

IRG Irregular motion of BR can be seen for $c \in \{45\} \cup [65, 70] \cup [90, 95] \cup [130, 140]$. The representative is shown in Figure 7. In this case, the aperiodic motion of time responses together with continuous frequencies distribution indicates the irregularity of the motion. Moreover, these cases are chaotic due to the output of the 0-1 test for chaos performed in Section 3.3.

3.2. Bifurcation diagram

Next, bifurcation diagrams of BR were plotted. The bifurcation diagram was created by making a 'stroboscopic plot' from the continuous function. A snapshot of the continuous function is taken once each stimulation cycle, at the same point in the cycle. This sequence of the snapshots was then plotted vertically. This operation is done for every simulated parameter c. The diagrams can be seen in Figure 8. In the diagrams, it can be seen that for $c \in [25, 30] \cup \{45\} \cup [65, 70] \cup [90, 100] \cup [130, 140]$ are responses either chaotic or with a much longer period than the data collection period for this diagram. At the other delays, there are regular responses. This coincides with time series exploration.

3.3. The 0–1 test for chaos

To distinguished between regular and irregular patterns, the 0–1 test for chaos was performed. This test, introduced in [4] (see also [5]), is used to distinguish regular and chaotic dynamics. It works with the time series and does not need any phase space reconstruction. The resulting value of this test can only be 0 (regular behaviour) or 1 (chaos). The details about the 0-1 test for chaos are given in Appendix 2.

For these simulations, a free software environment R [15] was used including key package developed by Martinovič [9]. The results of this test can bee seen in Figure 9. From the results it can be seen that chaotic motions for action potential were detected for $c \in \{45\} \cup [90, 95]$. For stimulation delays

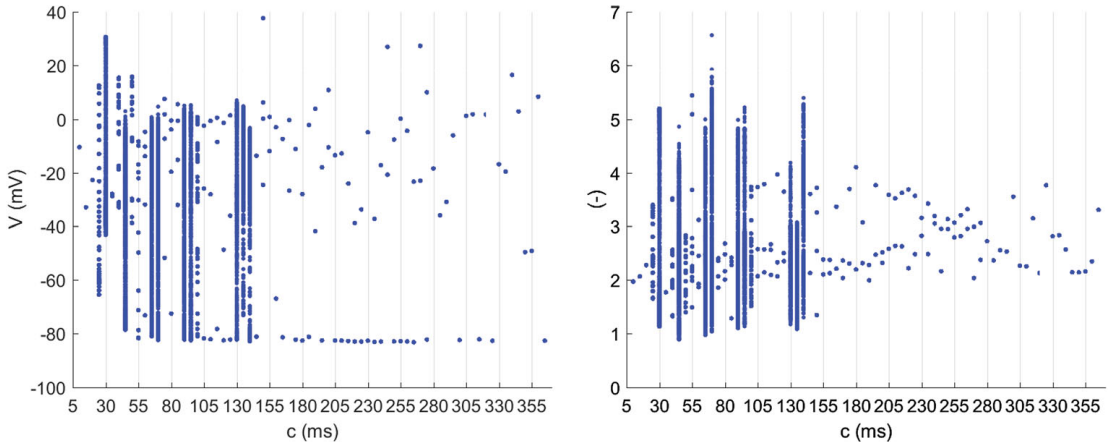

Figure 8. Bifurcation diagram of BR for $A = 80\,\mu\text{A/cm}^2$: for AP (left) and NMO (right).

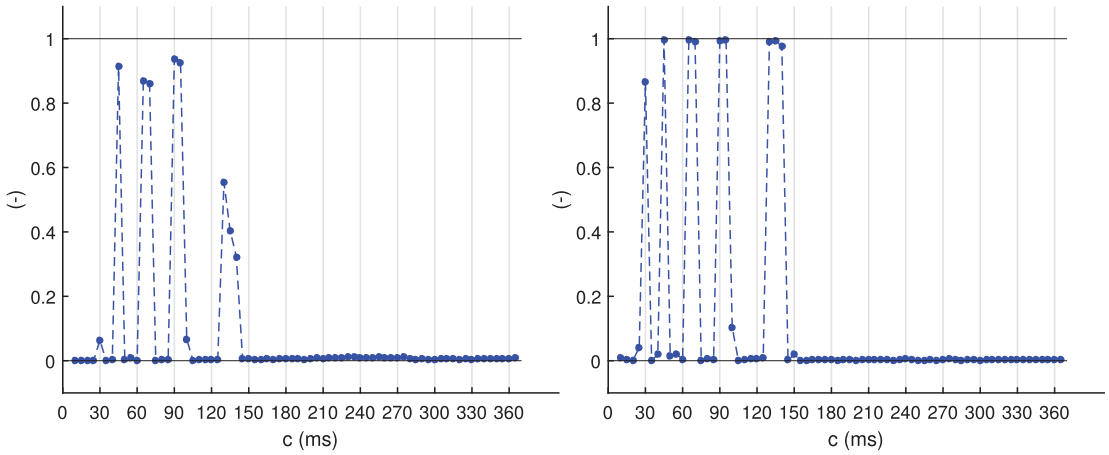

Figure 9. Results of the 0–1 test for chaos for $A = 80\,\mu\text{A/cm}^2$: for AP (left) and NMO (right).

$c \in [65, 70] \cup [130, 140]$ cannot be decided if it is chaotic or regular behaviour. Regular responses were detected elsewhere.

For variable NMO results of the 0–1 test for chaos reports chaotic behaviour for $c \in \{45\} \cup [65, 70] \cup [90, 95] \cup [130, 140]$. For stimulation delay $c = 30$ cannot be decided about the nature of motion. Regular responses were detected elsewhere.

However, since the stimulation of the heart cell is dependent not only on the stimulation frequency but also on the amplitude of stimulation, the 0–1 test for chaos was computed also for the amplitude range A from 36 to 130 $\mu\text{A/cm}^2$ with increments of 2 $\mu\text{A/cm}^2$. The results of this test for stimulation delay up to 160 ms can be seen in Figure 10 (above this delay are all responses regular, hence they are not depicted in the figure).

In Figure 10, it can be seen that chaotic regions are mainly concentrated into three regions. The first region is at stimulations delays about 30–70 ms . The second region is about $c = 90$ ms and the last region is on stimulation delays about 130 ms to 140 ms.

The results of this test for action potential contains a number of states, in which the character of motion cannot be decided about. These states are mainly concentrated on larger amplitudes. Nevertheless, when the model results are being investigated as a whole (in form of variable NMO) the vast majority of these indecisive states will disappear.

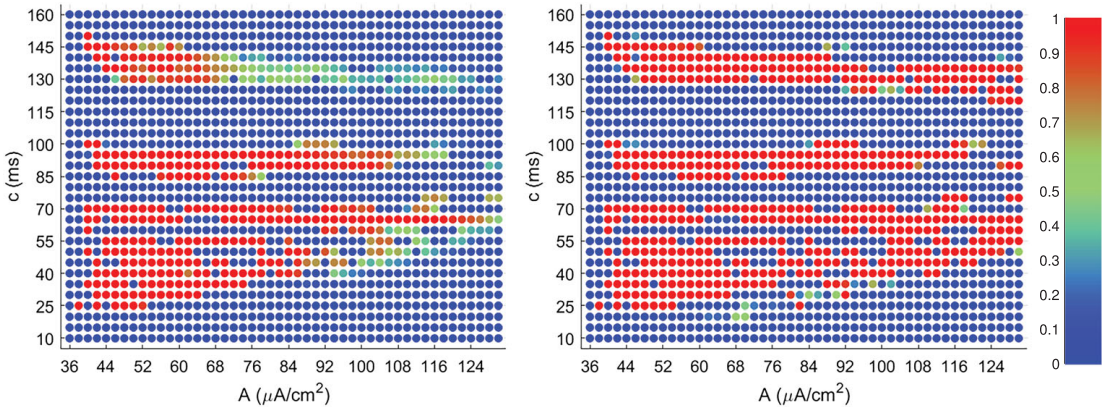

Figure 10. Results of the 0–1 test for chaos for all simulated range of *c* and *A*: for AP (left) and NMO (right).

4. Conclusions

In this paper, the dynamics of the Beeler–Reuter cardiac cell model was analysed in detail with respect to the amplitude *A* and stimulation delay *c*. The model (1) was forced by the stimulus with the shape of the half-sine period. The equations were solved numerically using the variable order solver based on the numerical differentiation formulas implemented as *ode15s* solver in Matlab. It was observed that the model is showing regular (see, e.g. Figure 2) as well as irregular patterns (see Figure 7) for different range of stimulation delays and amplitudes. For detection of this movements character, the Fourier spectra and bifurcation diagrams (see Figure 8) were used. Chaotic behaviour of action potential and normalized model output (NMO) were confirmed by the 0–1 test for chaos (Figures 9 and 10), for suitable choices of stimulation delays and amplitudes. However, in some cases, it cannot be decided if there is chaotic or regular behaviour. From the results can be seen, that the dynamical properties of the BR model are dependent not only to the frequency of stimulation but also to its amplitude.

The achieved results can be compared with paper [11], where dynamical properties of modified Fenton–Karma model of the heart cell were investigated. By this comparison, it can be seen that changes between regular and chaotic motions are much more rapid with the BR model. In particular, the dynamic properties of the BR model are much more dependent on the amplitude of the stimulus pulse.

Disclosure statement

No potential conflict of interest was reported by the author.

Funding

This work was supported by the Ministry of Education, Youth and Sports from the National Programme of Sustainability (NPU II) project 'IT4Innovations excellence in science – LQ1602'; by the Ministry of Education, Youth and Sports from the Large Infrastructures for Research, Experimental Development and Innovations project – IT4Innovations National Supercomputing Center – LM2015070; by the SGC grant No. SP2018/173 'Dynamic systems problems and their implementation on HPC', VŠB – Technical University of Ostrava, Czech Republic; by the project SV4508811/2101 'Biomedical Engineering Systems XIV', VŠB – Technical University of Ostrava, Czech Republic.

ORCID

R. Halfar http://orcid.org/0000-0003-1453-0101

References

[1] G.W. Beeler and H. Reuter, *Reconstruction of the action potential of ventricular myocardial fibres*, J. Physiol. (Lond.) 268 (1977), pp. 177–210. Available at https://physoc.onlinelibrary.wiley.com/doi/abs/10.1113/jphysiol.1977.sp011853.

[2] N. Cusimano, A. Bueno-Orovio, I. Turner, and K. Burrage, *On the order of the fractional Laplacian in determining the spatio-temporal evolution of a space-fractional model of cardiac electrophysiology*, PLoS One 10 (2015), pp. 1–16. Available at https://doi.org/10.1371/journal.pone.0143938.

[3] C.C. Drovandi, N. Cusimano, S. Psaltis, B.A.J. Lawson, A.N. Pettitt, P. Burrage, and K. Burrage, *Sampling methods for exploring between-subject variability in cardiac electrophysiology experiments*, J. R. Soc. Interface 13 (2016), p. 20160214. Available at http://rsif.royalsocietypublishing.org/content/13/121/20160214.

[4] A. Gottwald and I. Melbourne, *A new test for chaos in deterministic systems*, Proc. R. Soc. Lond. A 460 (2004), pp. 603–611.

[5] A. Gottwald and I. Melbourne, *On the implementation of the 0-1 test for chaos*, SIAM J. Appl. Dyn. 8 (2009), pp. 129–145.

[6] J. Jensen, P. Christiansen, A. Scott, and O. Skovgaard, *Chaos in the Beeler–Reuter system for the action potential of ventricular myocardial fibres*, Phys. D: Nonlinear Phenom. 13 (1984), pp. 269–277. Available at http://www.sciencedirect.com/science/article/pii/0167278984902835.

[7] B. Kogan, W. Karplus, M. Karpoukhin, I. Roizen, E. Chudin, and Z. Qu, *Action potential duration restitution and electrical excitation propagation in a ring of cardiac cells*, Comput. Biomed. Res. 30 (1997), pp. 349–359. Available at http://www.sciencedirect.com/science/article/pii/S0010480997914555.

[8] T.J. Lewis and M.R. Guevara, *Chaotic dynamics in an ionic model of the propagated cardiac action potential*, J. Theor. Biol. 146 (1990), pp. 407–432. Available at http://www.sciencedirect.com/science/article/pii/S0022519305807507.

[9] T. Martinovič, *Chaos01: 0-1 Test for Chaos*, R package version 1.1.0, 2016. Available at https://CRAN.R-project.org/package = Chaos01.

[10] Z. Qu, J.N. Weiss, and A. Garfinkel, *Spatiotemporal chaos in a simulated ring of cardiac cells*, Phys. Rev. Lett. 78 (1997), pp. 1387–1390. Available at https://link.aps.org/doi/10.1103/PhysRevLett.78.1387.

[11] H. Radek and L. Marek, *Dynamical properties of the improved FK3V heart cell model*, Math. Methods Appl. Sci. Available at https://onlinelibrary.wiley.com/doi/abs/10.1002/mma.5060.

[12] W.J. Rappel, *Filament instability and rotational tissue anisotropy: A numerical study using detailed cardiac models*, Chaos: Interdiscip. J. Nonlinear Sci. 11 (2001), pp. 71–80. Available at https://aip.scitation.org/doi/abs/10.1063/1.1338128.

[13] W.J. Rappel, F. Fenton, and A. Karma, *Spatiotemporal control of wave instabilities in cardiac tissue*, Phys. Rev. Lett. 83 (1999), pp. 456–459. Available at https://link.aps.org/doi/10.1103/PhysRevLett.83.456.

[14] A. Suzuki and H. Konno, *Stochastic dynamics of phase singularities under ventricular fibrillation in 2d Beeler–Reuter model*, AIP Adv. 1 (2011), p. 032103. Available at https://doi.org/10.1063/1.3614458.

[15] R.C. Team, *R: A Language and Environment for Statistical Computing*, R Foundation for Statistical Computing, Vienna, Austria, 2018. Available at https://www.R-project.org/.

[16] J. Weiss, A. Garfinkel, H. Karagueuzian, Z. Qu, and P. Chen, *Chaos and the transition to ventricular fibrillation – a new approach to antiarrhythmic drug evaluation*, Circulation 99 (1999), pp. 2819–2826.

Appendices

Appendix 1. Definition of BR model parameters

Table A1. Ionic currents in BR model.

Current	Description
i_{k_1}	time-dependent outward potassium current
i_{x_1}	time-activated outward current
i_{Na}	inward sodium current
i_{Ca}	the slow inward current carried mainly by calcium ions
i_{ext}	externally applied current

Table A2. Parameters E and g of BR model.

Parameter	Value	Units
$\overline{g_{\mathrm{Na}}}$	4	μ mmho/cm^2
g_{NaC}	0.003	μ mmho/cm^2
g_{s}	0.09	μ mmho/cm^2
E_{Na}	50	mV

Table A3. Parameters for calculation of constants α_y (ms^{-1}) and β_y (ms^{-1}) [1].

Constant	C_1	C_2	C_3	C_4	C_5	C_6	C_7
α_{x_1}	0.0005	0.083	50	0	0	0.057	1
β_{x_1}	0.0013	−0.06	20	0	0	−0.04	1
α_m	0	0	47	−1	47	−0.1	−1
β_m	40	−0.056	72	0	0	0	0
α_h	0.126	−0.25	77	0	0	0	0
β_h	1.7	0	22.5	0	0	−0.082	1
α_j	0.055	−0.25	78	0	0	−0.2	1
β_j	0.3	0	32	0	0	−0.1	1
α_d	0.095	−0.01	−5	0	0	−0.072	1
β_d	0.07	−0.017	44	0	0	0.05	1
α_f	0.012	−0.008	28	0	0	0.15	1
β_f	0.0065	−0.02	30	0	0	−0.2	1

Appendix 2. Description of the 0–1 test for chaos

This correlation method works as follows. For a given set of observations $\phi(j)$ for $j \in \{1, 2, \ldots, N\}$ translation variables for suitable choice of $b \in (0, 2\pi)$ are computed:

$$p_b(n) = \sum_{j=1}^{N} \phi(j) \cos(jb), \quad q_b(n) = \sum_{j=1}^{N} \phi(j) \sin(jb),$$

then the mean square displacement is computed using the following equation

$$M_b(n) = \lim_{N\to\infty} \frac{1}{N} \sum_{j=1}^{N} [p_b(j+n) - p_b(j)]^2 + [q_b(j+n) - q_b(j)]^2$$

here $n \leq n_{\text{cut}}$ where $n_{\text{cut}} \ll N$. Then, the estimate of the modified mean square displacement is computed using the next equation

$$D_b(n) = M_b(n) - \left(\lim_{N\to\infty} \frac{1}{N} \sum_{j=1}^{N} \phi(j) \right)^2 \frac{1 - \cos(nb)}{1 - \cos(b)}.$$

Finally, the output of the 0–1 test is obtained as a correlation coefficient of ξ and Δ for fixed parameter b

$$K_b = \text{corr}(\xi, \Delta),$$

where $\xi = (1, 2, \ldots, n_{\text{cut}})$ and $\Delta = (D_b(1), D_b(2), \ldots, D_b(n_{\text{cut}}))$. Hence, K_b depends on the choice of b. To get K as the output of the 0–1 test, as limiting value of all K_b, the result value is taken as

$$K = \text{median}(K_b).$$

frontiers in Physiology

ORIGINAL RESEARCH
published: 13 August 2021
doi: 10.3389/fphys.2021.709485

Machine Learning Identification of Pro-arrhythmic Structures in Cardiac Fibrosis

Radek Halfar[1]*, *Brodie A. J. Lawson*[2,3], *Rodrigo Weber dos Santos*[4] and *Kevin Burrage*[3,5]

[1] IT4Innovations, VSB-Technical University of Ostrava, Ostrava, Czechia, [2] Centre for Data Science, School of Mathematical Sciences, Queensland University of Technology, Brisbane, QLD, Australia, [3] ARC Centre of Excellence for Mathematical and Statistical Frontiers, School of Mathematical Sciences, Queensland University of Technology, Brisbane, QLD, Australia, [4] Graduate Program in Computational Modeling, Universidade Federal de Juiz de Fora, Juiz de Fora, Brazil, [5] Department of Computer Science, University of Oxford, Oxford, United Kingdom

Cardiac fibrosis and other scarring of the heart, arising from conditions ranging from myocardial infarction to ageing, promotes dangerous arrhythmias by blocking the healthy propagation of cardiac excitation. Owing to the complexity of the dynamics of electrical signalling in the heart, however, the connection between different arrangements of blockage and various arrhythmic consequences remains poorly understood. Where a mechanism defies traditional understanding, machine learning can be invaluable for enabling accurate prediction of quantities of interest (measures of arrhythmic risk) in terms of predictor variables (such as the arrangement or pattern of obstructive scarring). In this study, we simulate the propagation of the action potential (AP) in tissue affected by fibrotic changes and hence detect sites that initiate re-entrant activation patterns. By separately considering multiple different stimulus regimes, we directly observe and quantify the sensitivity of re-entry formation to activation sequence in the fibrotic region. Then, by extracting the fibrotic structures around locations that both do and do not initiate re-entries, we use neural networks to determine to what extent re-entry initiation is predictable, and over what spatial scale conduction heterogeneities appear to act to produce this effect. We find that structural information within about 0.5 mm of a given point is sufficient to predict structures that initiate re-entry with more than 90% accuracy.

Keywords: machine learning, neural networks, fibrosis, cardiac electrophysiology, arrhythmia, monodomain model, re-entry, unidirectional block

OPEN ACCESS

Edited by:
Rafael Sebastian,
University of Valencia, Spain

Reviewed by:
Oleg Aslanidi,
King's College London, United Kingdom
Francisco Sahli Costabal,
Pontificia Universidad Católica de Chile, Chile

***Correspondence:**
Radek Halfar
radek.halfar@vsb.cz

Specialty section:
This article was submitted to Computational Physiology and Medicine, a section of the journal Frontiers in Physiology

Received: *14 May 2021*
Accepted: *30 June 2021*
Published: *13 August 2021*

Citation:
Halfar R, Lawson BAJ, dos Santos RW and Burrage K (2021) Machine Learning Identification of Pro-arrhythmic Structures in Cardiac Fibrosis. Front. Physiol. 12:709485. doi: 10.3389/fphys.2021.709485

1. INTRODUCTION

According to the WHO, in 2016, 17.9 million people worldwide died of cardiovascular diseases (31% of all deaths). These diseases are the most common cause of death in the world. Although the function and dysfunction of the heart have been extensively studied, the sheer complexity of the spatiotemporal dynamics underlying its electrical signalling process leaves much still poorly understood. This is particularly true when complicating factors are present, such as cardiac fibrosis.

Cardiac fibrosis, the over-activity of fibroblasts in the heart, poses significant health risks (Hinderer and Schenke-Layland, 2019). Fibroblasts deposit extracellular matrix proteins that can separate myocytes, resulting in tortuous paths of activation that increase the risk of signalling malfunctions. This risk depends critically on the extent and arrangement of afflicted tissue, but this dependency is intricate and very difficult to quantify. Efforts have been made to classify

different types of fibrotic patterning with the suggestion that might help stratify risk (de Jong et al., 2011) but with little attempt to explain why or how these different types of pattern present different levels of risk. A separate approach focuses on small-scale structures that produce key behaviours underlying re-entry and arrhythmia. The pro-arrhythmic mechanisms of fibrosis are well understood (Nguyen et al., 2014), but the precise patterns that do or do not trigger those mechanisms are not well understood. The computational simulation presents a powerful tool for investigating these structures mechanistically, and machine learning (ML) provides the opportunity to automate identification.

In this study, we consider the risk of re-entry posed by many different fundamental structures of fibrosis. The specific pattern of fibrosis plays two important roles in the promotion of re-entry or micro-re-entry: through re-entrant paths within the damaged region that are long enough to accommodate the wavelength of the propagating action potential (AP) and by the presence of structures that facilitate one-way block of AP propagation. We concentrate on the latter, that is, structures that selectively block conduction, for example, permitting conduction in one direction but not the other. This phenomenon of a *unidirectional block* is a critical precursor to re-entry (Quan and Rudy, 1990).

Computational studies have successfully reproduced re-entries from fibrosis for different types of diseases, such as atrial fibrillation (Alonso et al., 2016; Vigmond et al., 2016), myocardial infarction (Sachetto Oliveira et al., 2018a), and many other pathologies related, for instance, to hypoxia and fibrosis including hypertrophic cardiomyopathy, hypertensive heart disease, recurrent myocardial infarction, obstructive pulmonary disease, obstructive sleep apnoea, and cystic fibrosis (Sachetto Oliveira et al., 2018b). However, as we do not know which kind of patterns within the fibrotic substrate are pro-arrhythmic, these studies depend on the generation of hundreds of thousands of fibrosis patterns, followed by Monte Carlo simulations and statistical analysis. These studies have investigated, for example, the probability of re-entry as a function of the fraction of damaged tissue. Nevertheless, the kind of patterns that facilitate unidirectional blocks and how often these patterns are present in damaged tissues are important open questions.

Machine learning (ML), as with most fields, has begun to see a considerable application to cardiac electrophysiology. These include automated extraction of subtle information from the electrogram (Yang et al., 2018; Mincholé et al., 2019) and the identification of promising targets or success rates for ablation (Zahid et al., 2016; Muffoletto et al., 2019, 2021; Shade et al., 2020). In this study, we generate a large number of different realisations of fibrotic arrangement corresponding to significantly damaged tissue and then apply a single stimulus originating from many different points. This creates a rich dataset of structures that give rise to re-entry. We then isolate regions of selective block and train a classifier model that identifies with high accuracy whether a given pattern of fibrosis generates this pro-arrhythmic behaviour. Importantly, this successful classification is a first step to address fundamental questions relating anatomical heterogeneity to re-entry risk, and over what spatial scale these effects manifest.

2. MATERIALS AND METHODS

2.1. Simulation of Cardiac Activity

We simulate cardiac activity inside the regions afflicted with fibrosis, examining the patternings of obstacles to conduction that initiate re-entries sustained inside these fibrotic regions. These micro-re-entries cause fibrotic regions to act potentially as ectopic pacemakers that drive tachycardia or other arrhythmia (Hansen et al., 2015). As our focus is on the initiation and immediate sustainment of re-entry, we do not simulate how waves of activation produced by a fibrotic region interact with healthy surrounding tissue, nor do we consider scenarios such as fast pacing that indicate the existence of prior signalling dysfunction.

Cardiac electrophysiological dynamics were simulated using the monodomain formulation (Sundnes et al., 2006),

$$C_m \frac{\partial V}{\partial t} = \nabla \cdot \left(D \nabla V \right) - I_{\text{ion}}, \tag{1}$$

which treats cardiac cells as capacitive and hence describes the change in their membrane potential in terms of the current that flows diffusively to/from neighbouring cells through gap junctions and by ion transport through the ion channels of the cell membrane. We use a capacitance density of $C_m = 1\,\mu\text{F}\,\text{m}^{-2}$ and electrical conductivity $D = 2.5 \times 10^{-4}\,\text{mS}$. Cell APs were simulated using the Bueno-Orovio–Cherry–Fenton (BOCF) model, a reduced model that nevertheless accurately captures the most important electrophysiological dynamics of ventricular myocytes (Bueno-Orovio et al., 2008). To represent the effects of significant tissue damage on APs Shaw and Rudy (1997); Sachetto Oliveira et al. (2018b), we modified model parameters to shorten AP duration (APD) to approximately 50 ms (see **Figure 1A** and **Table 1**). This results in a conduction velocity of $23\,\text{cm}\,\text{s}^{-1}$, reflecting the decreased gap junction functionality in diseased tissue (Duffy, 2012; Nguyen et al., 2014).

Simulations were carried out in two-dimensional, $2 \times 2\,\text{cm}$ slices of isotropically conductive cardiac tissue. We chose a larger amount of tissue than the minimum needed to support re-entry as reported for these types of conditions ($0.7 \times 0.7\,\text{cm}$; Sachetto Oliveira et al., 2018b), so as to increase the number of re-entries present in our generated data. The effect of fibrosis on conduction was represented by the presence of non-conducting obstacles (for example collagen), a common approach taken for both ventricular tissue (Ten Tusscher and Panfilov, 2007; McDowell et al., 2011) and atrial tissue (Cherry et al., 2007; McDowell et al., 2015), as well as highly-detailed microscopic models of cardiac tissue where cells are disconnected by barriers or dead cells (Jacquemet and Henriquez, 2009; Hubbard and Henriquez, 2014; Gouvêa de Barros et al., 2015). This approach is in contrast to approaches that represent fibrotic obstacles indirectly through modifications to conductivity in afflicted areas, often in response to imaging data informing fibroblast density (Zahid et al., 2016; Roy et al., 2020).

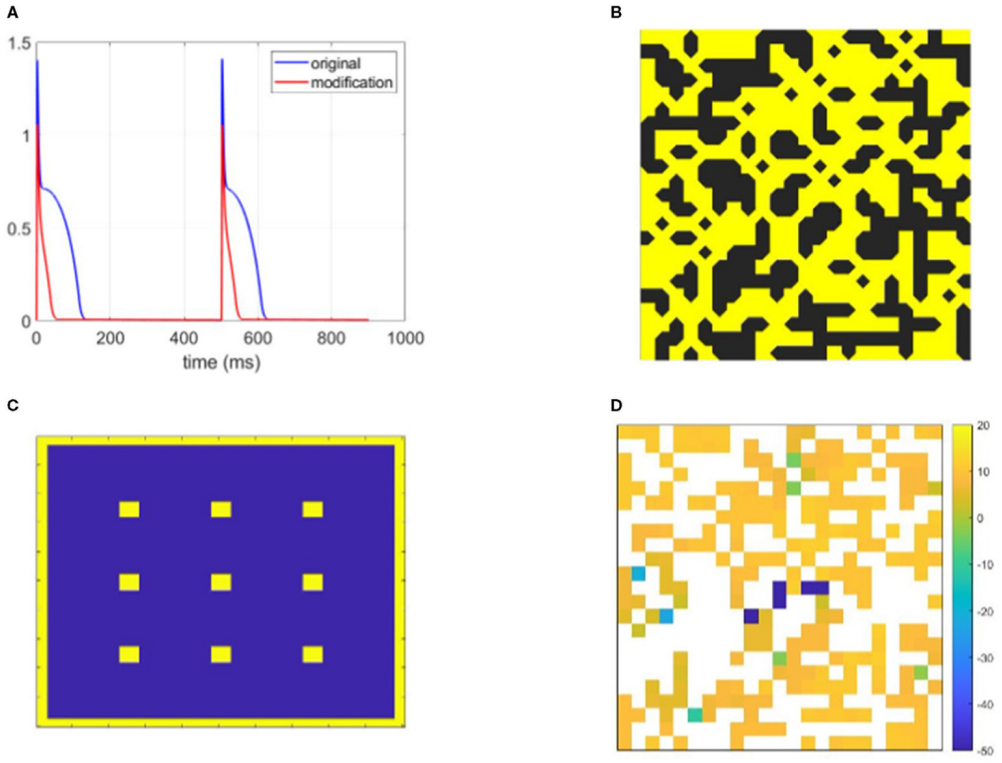

FIGURE 1 | Graphical demonstration of some of the methods used in this study. **(A)** The action potential (AP) of the Bueno-Orovio-Cherry-Fenton (BOCF) model modified to represent strongly fibrosis-afflicted tissue (parameters in **Table 1**), and the original BOCF model. Remodelled myocytes repolarise very rapidly with a triangular-shaped AP. **(B)** An example fibrotic structure, visualised to highlight the 'diagonal' connectivity inherent to placing nodes on element vertices. **(C)** The stimulus locations (yellow) used across separate simulations to generate wavefronts travelling in different directions and hence bolster identification of structures that produce re-entry. **(D)** Re-entry vulnerability index (RVI) values observed for the structure pictured in **(B)**, showing the identification (by significantly negative value) of locations that demonstrate selective conduction block.

TABLE 1 | The parameters of the Bueno-Orovio-Cherry-Fenton (BOCF) model, modified to represent cardiac tissue with significant fibrosis.

Parameter	Value	Parameter	Value	Parameter	Value
C_m	1	τ_v^+	1.4506	τ_{s1}	2.7342
u_v	0.3	τ_{v1}^-	60	τ_{s2}	16
u_v^-	0.006	τ_{v2}^-	1150	τ_{fi}	$0.11C_m$
u_w	0.13	τ_w^+	200	τ_{si}	2.8
u_w^-	0.03	τ_{w1}^-	60	τ_{so1}	30.0181
u_o	0.006	τ_{w2}^-	15	τ_{so2}	0.9957
u_s	0.9087	τ_{w_∞}	0.07	k_s	2.0994
u_{so}	0.4	τ_{o1}	400	k_w^-	65
u_u	1.2	τ_{o2}	6	k_{so}	2.0458
w_∞^*	0.94				

Parameter notation is that of Bueno-Orovio et al. (2008).

Obstacles were seeded randomly through the domain by randomly replacing each grid element with a non-conductive element with some fixed probability ρ, a typical approach used for modelling diffuse fibrosis (Kazbanov et al., 2016). We did not explicitly consider the other types of fibrotic microtexture (such as compact or patchy fibrosis de Jong et al., 2011). However, by choosing $\rho \sim 0.5$ and simulating many different realisations, we have considered a very broad range of patterns on the fine-scale that we analyse in this study. It is worth noting that other types of fibrotic patterning could be directly incorporated into our machine learning workflow through recent techniques for computer generation of large numbers of realisations of different fibrotic patterns (Clayton, 2018; Jakes et al., 2019).

Equation (1) was discretised using a vertex-centred control volume finite element method that integrates bilinear interpolants over the square-shaped elements. This generates a non-diagonal mass matrix and significantly reduces discretisation error in this sharp-fronted wavefront setting (Pathmanathan et al., 2012). For a vertex-centred mesh where nodes are at element vertices, excitation can still propagate through the "crack" between diagonally opposed obstructions, owing to a node being there. As such, to make our visualisations of fibrotic structures more intuitive, we display fibrotic obstructions such that these diagonal connections are respected (**Figure 1B**). Timestepping used the second-order generalisation of the Rush–Larsen method put forward by Perego and Veneziani (2009), with $\Delta t = 0.05$ ms. Simulations continued until all cardiac activity died out, or $t = 2$ s was reached. These simulations were carried out on the Barbora supercomputer (Czech Republic).

2.2. Re-entries and Conduction Block

Our study concentrates solely on the effect of structure on the initiation of re-entrant patterns of activation. As such, each individual simulation used only one stimulus pulse so as to preclude other conflating factors such as repolarisation heterogeneity in scarred tissue (Gough et al., 1985). However, to maximise the opportunity to identify pro-arrhythmic structures, we increased robustness to specific propagation directions and patterns of activation by separately using 13 different stimulus sites for each fibrotic realisation (**Figure 1C**). To obtain sufficient data featuring re-entry, a sweep through values $0.4 \leq \rho \leq 0.6$ was first used to determine those extents of fibrosis prone to re-entry. For each density value considered, 50 different realisations of fibrosis were created. Re-entry was detected by the activation of any boundary nodes more than one time (**Figure 2**), capturing ectopic waves that successfully escape the fibrotic region being simulated. A realisation of fibrotic structure that generated a re-entry for any of the possible stimulus sites was then labelled as a substrate for re-entry.

Following initial observations, our high-throughput simulation protocol concentrated on the range $\rho \in [0.46, 0.50]$ as the values most prone to re-entry. For each ρ value in this range (in increments of 0.01), an additional 800 fibrotic patterns were created, and the same simulation protocol as above then applied to each. **Table 2** summarises the size, and basic qualities, of the resulting data.

To detect specific micro-structures that promote re-entry, we used the re-entry vulnerability index (RVI) (Orini et al., 2017; Orini et al., 2019). This index calculates the difference in activation time for a node and the repolarisation time of its neighbours, and hence indicates potential for re-entry formation (**Figure 1D**). In particular negative values occur when a neighbouring node has already activated and repolarised when a node first activates, allowing the node to spread its activation back to that neighbour and potentially much more of the tissue. This scenario arises when conduction blocks despite the existence of waiting excitable tissue, for example, due to excessive electrotonic loss (Nguyen et al., 2014). An example of conduction dying out due to source-sink mismatch, only for wave propagation to succeed in travelling through the same structure from a different direction, is provided in **Figure 3**.

Significantly negative RVI values further indicate a likelihood that surrounding tissue will also be ready to excite, increasing the risk that a re-entrant event develops into an ectopic wavefront significant enough to escape and hence trigger extrasystole. We, therefore, find all locations that exhibited RVI values below a threshold RVI ≤ -50. When multiple locations were detected together as a contiguous group, these were simplified to a single location. Around each detected site, the patterning of fibrosis

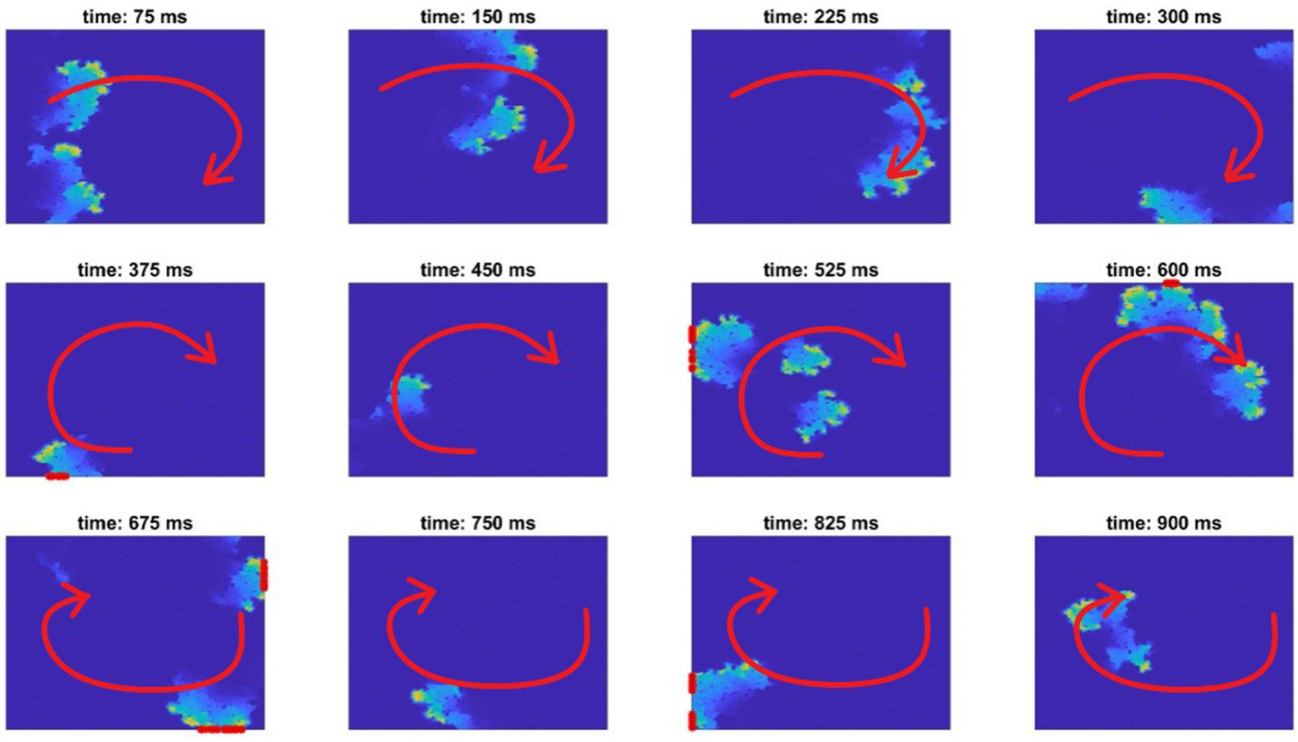

FIGURE 2 | A re-entry formed in fibrotic tissue (red arrow indicates the direction of AP propagation), and its detection. An AP initialised on the left border propagates through the tissue, failing to conduct through the bottom passage. Then, when the excitation turns around (about 250 ms), it transmits through this bottom passage and successfully re-emerges into the remainder of tissue, forming a re-entry (about 375 ms). Only re-entries that might escape back into the tissue surrounding the afflicted region are counted, as detected by nodes sitting on the boundary of the domain being activated more than one time (marked with a red asterisk on the boundaries).

(as an array of binary values) was extracted, and labelled as a "discriminative" structure, reflecting its inconsistent passing along the excitation dependent on wavefront direction or other conditions. To complete the dataset, this set of structures was complemented by a set of 'indiscriminate' structures of the same size, selected by finding locations that satisfied two conditions. First, indiscriminate structures have to be activated (at least 40% of their constituent excitable tissue), so that their effects on wavefront propagation had been tested by the simulation they came from. Second, indiscriminate structures could not contain any locations identified by RVI values under the threshold as discriminative.

TABLE 2 | Summary of the simulations performed, and the resulting data used for machine learning (ML) (using one structure size as an example).

65,650	Total simulations
3,902	Simulations featuring a re-entry (that reached the boundary)
5,050	Unique arrangements of fibrosis
1,907	Fibrotic arrangements that generated re-entry
228,659	11×11 binary patterns exhibiting selective block
228,571	11×11 binary patterns not exhibiting selective block

2.3. Pattern Classification

To explore how much information regarding re-entry risk is contained in the patterning of fibrosis, we considered the ability of neural networks (NN) to successfully classify different

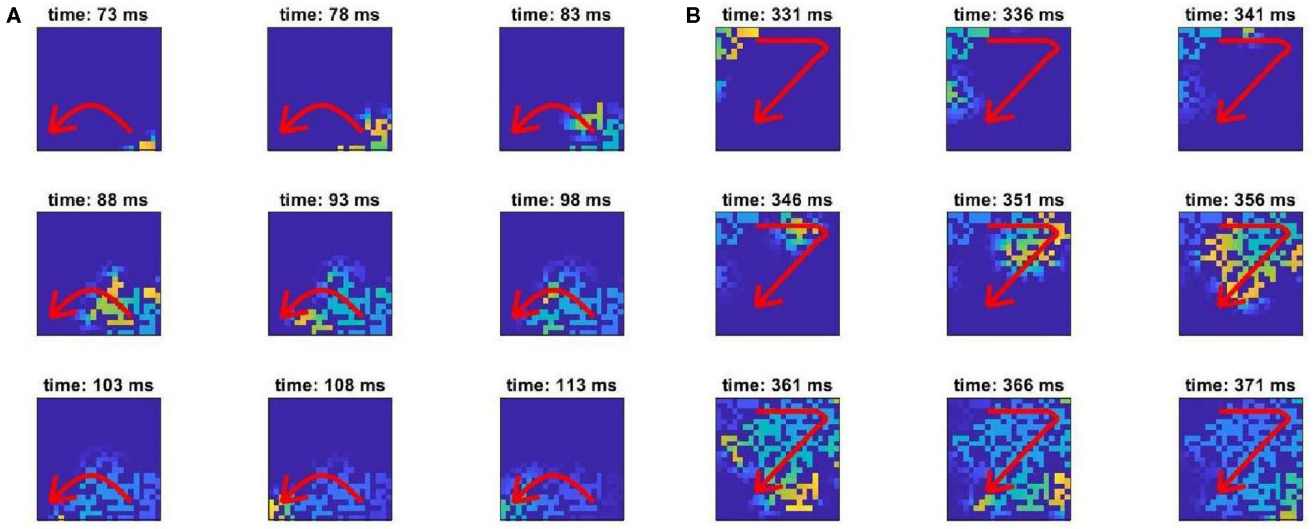

FIGURE 3 | Snapshots of AP propagation demonstrating an event of the unidirectional block. Visualised is one section of the full fibrotic region, detected by our RVI-based approach. The brightness of colour indicates level of activation, and the red arrows indicate the overall direction of propagation. **(A)** The wave propagates from the bottom-right to the bottom-left corner of the section, attempting also to propagate through the central passage but failing due to an imbalance between excited and excitable tissue. **(B)** When the wavefront later propagates through the top portion of this structure, it is able to successfully propagate downwards through the central passage, re-entering into the tissue in the bottom portion.

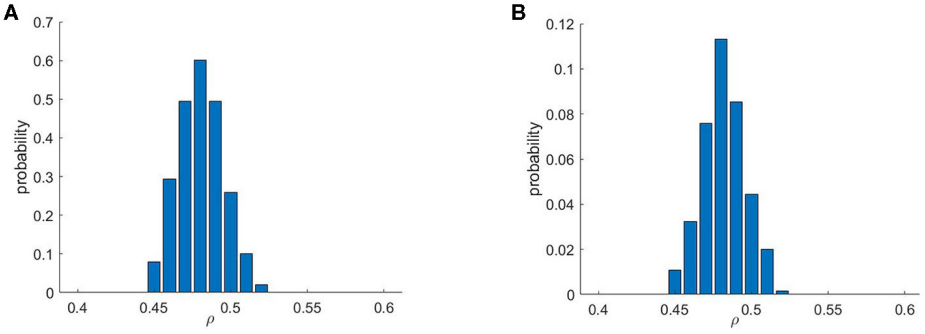

FIGURE 4 | Re-entry formation depends critically on the amount of fibrotic obstructions. Only a specific range of values of ρ, the probability that any individual mesh element is obstructed, permits re-entry formation. Shown are the probabilities that a given fibrotic realisation produced a re-entry for **(A)** at least one stimulus scenario and **(B)** for an individual stimulus scenario. A comparison of these two histograms highlights the importance of considering multiple stimulus locations when evaluating a structure for potential as an arrhythmic substrate.

structures as discriminative about excitation transfer or not. The datasets were made balanced by detecting and adding indiscriminate structures until these were the same in number as the discriminative structures. As each structure is a binary mask, they can simply be converted to a vector of 0 and 1 values to serve as input to an NN. The NN then outputs a single value indicating a category to which structure belongs (discriminative or not).

A variety of NN architectures were considered, using densely interconnected layers and zero to four hidden layers. Layer size varied from 100 to 1,200 neurons. All NN training and evaluation used the Keras application programming interface (API) (Chollet, Francois et al., 2015), a popular Python library for machine learning. We used the *Adam* optimiser with a binary cross-entropy loss function to optimise the neural network. The rectified linear activation function (*ReLU*) activation function was used in the inner layers and a sigmoid activation function in the outer layer. To explore the spatial scale on which patterning acts to create selective block of conduction and hence re-entry, we also considered the ability to identify selectively blocking patterns when working with structures of various sizes. In particular we take the element identified *via* RVI as the centre of a square binary pattern, with side lengths varying from 5 elements (0.5 mm) to 23 elements (2.3 mm).

3. RESULTS

3.1. Preliminary Results

As briefly mentioned in Methods, re-entries were found to appear only within a rather selective range of ρ values (**Figure 4**), matching observations of previous studies considering micro re-entry in untextured fibrosis (Sachetto Oliveira et al., 2018a,b). This effect is caused by the requirement for both a sufficient amount of obstruction to create the structures that produce a source-sink mismatch, and a sufficiently conductive structure for any resulting re-entrant event to successfully reach the domain boundary and hence produce an ectopic beat. This balance is strongly related to the percolation threshold, and we note that the critical range of $0.45 \leq \rho \leq 0.52$ for re-entry is here larger than in the previous studies, as vertex-centred meshes are naturally more conductive. **Figure 4** also compares the chance of re-entry for any individual simulation (one stimulus site), with the chance per pattern realisation (for at least one re-entry across all stimulus sites). Even given that a structure can produce re-entries that escape the fibrotic region, only very few choices of stimulus location result in this behaviour, demonstrating a significant sensitivity to activation pattern.

Figure 5 compares the frequency with which selectively blocking micropatterns were identified across the large-scale fibrotic realisations (4 cm^2) that did or did not result in re-entry. The cases exhibiting re-entry showed on average more than two times as many selectively blocking sites than those that did not. This confirms the intuition that the presence of microstructures that may initiate re-entry correlates significantly with the overall risk posed by a fibrotic region. However, even those realisations that did not produce re-entry under any stimulus scenario still produced many individual events of unidirectional or other selective block of conduction. This shows that the mutual spatial arrangement of these initiator patterns, and the larger-scale structure more generally, is also critical to the formation of re-entries that persist and escape into the surrounding tissue. Notably, there exists a positive feedback effect when it comes to simply counting detected discriminative microstructures, and as once a re-entry has successfully formed, there is an additional opportunity for repolarisation heterogeneity to produce further block events in vulnerable microstructures.

Individual examples of micropatterns capable or incapable of initiating re-entry, as detected by our methods, are presented in **Figure 6**. As shown by the arrows indicating the direction of AP propagation (or block), the pro-arrhythmic patterns (left side) all result in unidirectional block. Examining the fine-scale structures that produce this effect reveals broad correspondence to the AP emerging from thin passages into larger regions of open tissue. This is the classical example of structural heterogeneity producing unidirectional block through source-sink mismatch (Ciaccio et al., 2018). However, the rich diversity of patterning in these structures and the presence of visually similar arrangements in the structures observed to permit normal conduction (right side of figure) highlight the difficulty of differentiating by eye alone patterns that may or may not initiate re-entry. This motivates the use of machine learning as a more accurate, and automated, means of carrying out this classification.

3.2. Classification of Micropatterns That Can Initiate Re-entry

The micropatterns that do or do not exhibit selective (unidirectional, or inconsistent) conduction block were learned by training a NN classifier, as described in Methods. Depending on the NN architecture and micropattern size, the overall accuracy of the classifier (as evaluated using unseen test

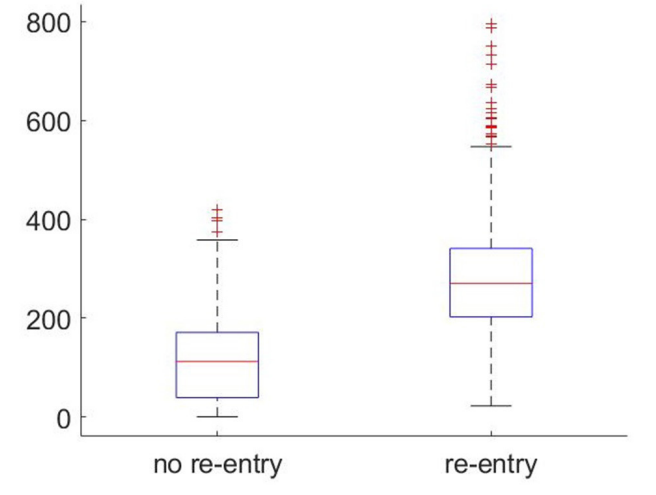

FIGURE 5 | Boxplots showing the frequency of microstructures that selectively block condution (as detected by significant negative RVI) occurring in large-scale fibrotic realisations that did or did not exhibit re-entry. The higher the number of such discriminative structures found, the more likely a re-entrant AP will survive and then escape into the surrounding tissue.

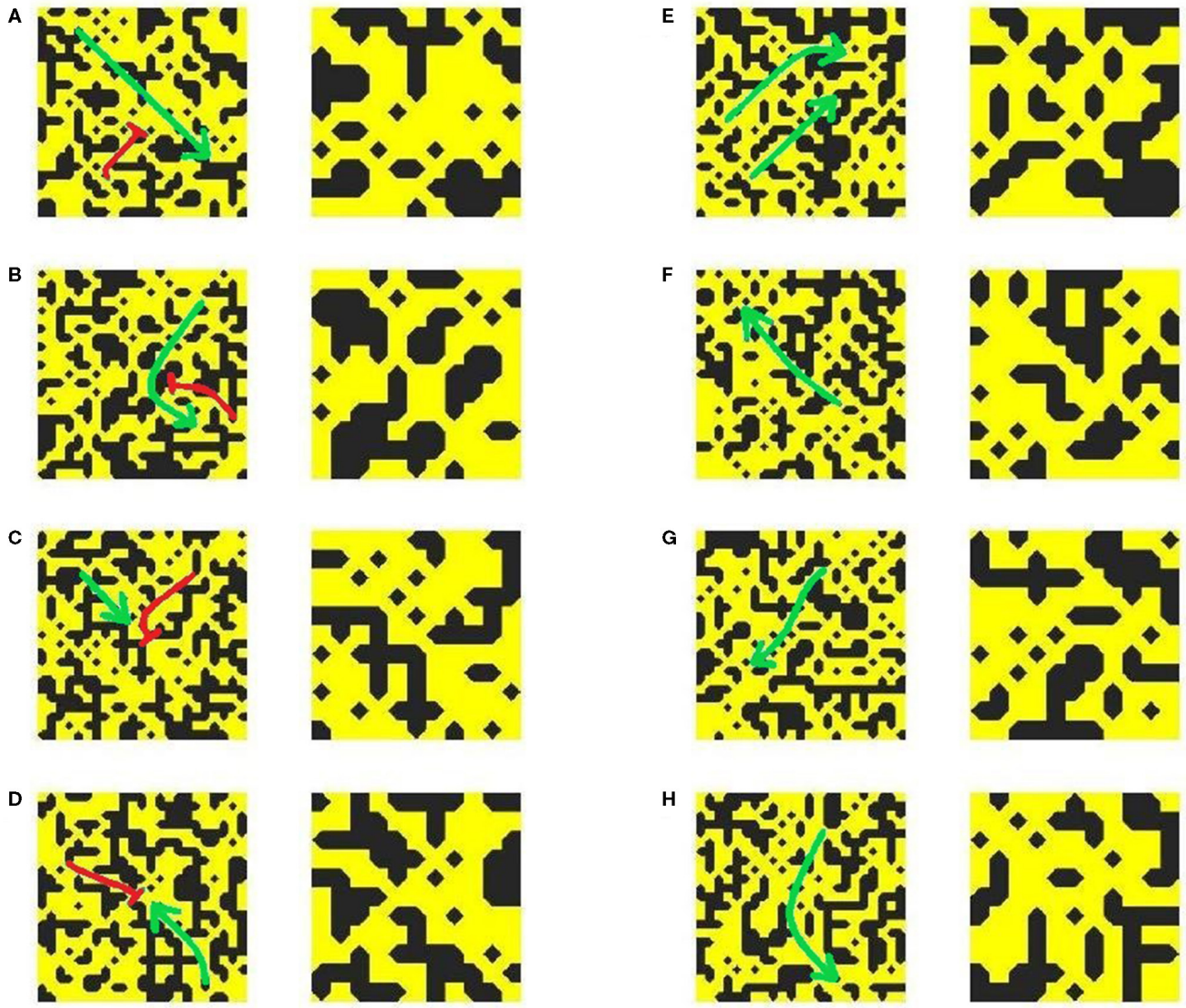

FIGURE 6 | Examples of pro-arrhythmic **(A–D)** and non-arrhythmogenic **(E–H)** micropatterns (23×23 elements), and a close-up view of the structure at their centre. Green arrows indicate the directions of AP propagation, with red flat arrowheads indicating conduction block.

data) ranged from approximately 75 to 91%. Specificity and sensitivity ranged from 74 to 91%, and the area under the receiver operating characteristic curve (ROC) curve ranged from 0.82 to 0.95. The dependence of performance on network architecture, for a fixed micropattern size, is summarised in **Table 3**, where it can be seen that maximal classification accuracy of 91% was obtained by using two hidden layers of 1,000 neurons each. This architecture strikes the balance between including enough neurons to capture the high complexity of the classification problem, and the risks of training difficulties or overfitting posed by a network with too many neurons. The classification problems using other micropattern sizes showed very similar relationships between accuracy and network architecture. In **Table 4** is shown the confusion matrix of the NN for micropatterns of size 23 × 23, and 9 × 9. These results confirm that NN performance is balanced, that is, the NN can detect pro-arrhythmic as well as non pro-arrhythmic structures with the same accuracy.

The classifier models with appropriate architectures obtain very good accuracy, considering they are attempting to identify a complex phenomenon such as unidirectional or otherwise selective block only from binary micropattern data. On one hand, we have considered many different patterns of activation (by using different choices of stimulus site) to generate these data, and so structures identified as pro-arrhythmic might still exist safely in a scar region if they never experienced waves travelling in the necessary direction to trigger the initial re-entry. On the other hand, structures identified as non-arrhythmogenic will have been subjected to multiple different AP propagation scenarios. This suggests that microstructures identified as indiscriminate

TABLE 3 | The resulting accuracy/area under the curve (AUC) of the neural network (NN) for the size of the micropattern 9.

		Hidden layers				
		0	1	2	3	4
Neurons in layer	100	0.758/0.837	0.791/0.871	0.804/0.881	0.809/0.887	0.817/0.891
	200	0.778/0.855	0.844/0.91	0.864/0.925	0.865/0.925	0.866/0.925
	400	0.81/0.884	0.893/0.937	0.886/0.938	0.895/0.941	0.882/0.933
	600	0.833/0.898	0.899/0.943	0.901/0.945	0.901/0.946	0.9/0.946
	800	0.848/0.907	0.894/0.938	0.9/0.945	0.904/0.947	0.894/0.938
	1000	0.855/0.915	0.904/0.946	0.911/0.952	0.909/0.951	0.903/0.948
	1200	0.856/0.915	0.908/0.947	0.91/0.95	0.905/0.946	0.897/0.947

TABLE 4 | (A) The confusion matrix of the NN for 23×23 micropatterns, with four hidden layers and 800 neurons in each layer.

		True state	
		Pro-arrhythmic	Not pro-arrhythmic
(A)			
Prediction	Pro-arrhythmic	17,179	4,611
	Not pro-arrhythmic	4,616	17,174
(B)			
Prediction	Pro-arrhythmic	20911	2,090
	Not pro-arrhythmic	2,094	20,915

(B) The confusion matrix of the NN for 9×9 micropatterns, using three hidden layers and 1,000 neurons in each layer.

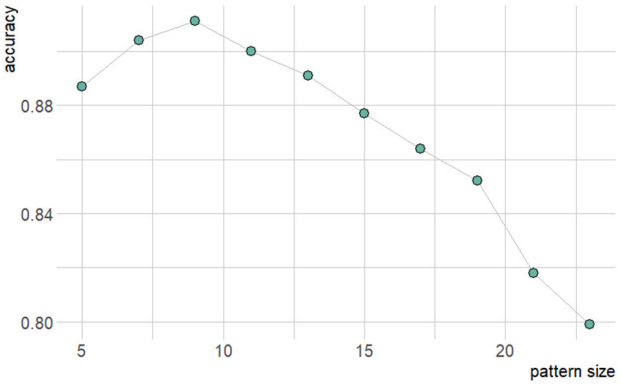

FIGURE 7 | Graph of resulting accuracy dependence on micropattern size for two hidden layers and 1,000 neurons.

could potentially be considered safe independent of the factor of wavefront direction.

Classifier accuracy also allows us to consider the information necessary in order to identify pro-arrhythmic micropatterns of obstruction. In this study, we have varied the size of these micropatterns, and thus can gain some understanding regarding the spatial scale on which the dynamics of unidirectional or selective block truly acts. On one hand, if the structures considered are too small to correctly identify the relevant source-sink interactions, accuracy will suffer due to this lack of requisite information. On the other hand, when redundant information is included by using a too large micropattern size, this only increases the dimensionality of the learning problem without supplying anything useful, and accuracy suffers due to the negatively shifted the balance between dimension and amount of training data.

Figure 7 shows how changes to micropattern size impact the accuracy of the resulting classifier models. Accuracy peaks for patterns of size 9×9, suggesting that the balance of source-sink mismatch for a wavefront is meaningfully controlled by the surrounding structure on a length scale of about 0.4–1 mm. The larger end of this range arises from the observation that with increased amounts of training data, higher-dimensional datasets may have exhibited even higher classification accuracy. Saliency maps, which show the respective levels of contribution of the individual elements of a structure towards the resulting classification output by a NN, also showed a tendency to concentrate importance on a small central subsection of the larger micropatterns (**Figure 8**). This provides further evidence towards the conclusion that selective and unidirectional block events are governed by structure over only a small length scale.

3.3. Generalisation to New Data

In discussing classifier model accuracy, we have been referring to the performance of the model in classifying micropatterns not seen by it during the training process, but still sourcing from the same overall batch of simulations from which the training data were taken.

In this study, we test the classifier model in a more demanding fashion by evaluating its performance on a new batch of simulations designed to more directly examine events of the selective block. These simulations were carried out on smaller fibrotic domains (46×46 elements total), with single stimuli triggered separately on all four edges of the domain to increase the chance of observing unidirectional block where it might arise. The best-performing classifier model was then used to try to identify which microstructures in these new realisations of fibrosis would or would not show this type of block.

Figure 9 shows a range of example patterns, including those (both susceptible and not susceptible to unidirectional block) that the classifier model successfully identified, and some of the pro-arrhythmic structures that the model failed to detect. The

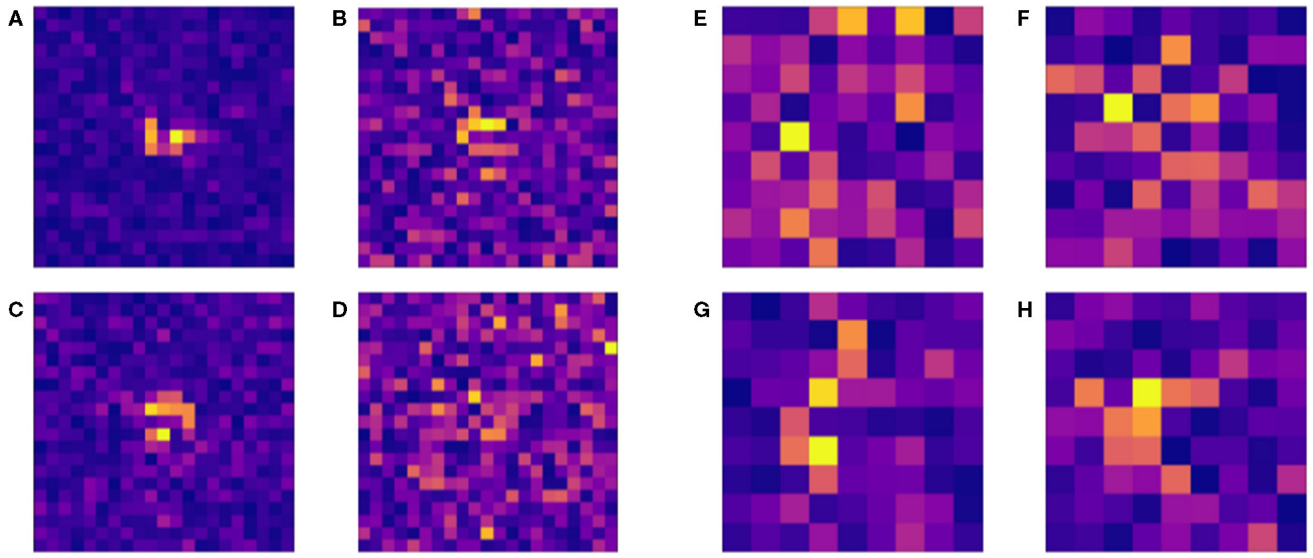

FIGURE 8 | Example saliency maps for a selection of 21×21 **(A–D)** patterns classified by a neural network with zero hidden layers and 1,200 neurons in one layer and 9×9 patterns **(E–H)** with two hidden layers and 1,000 neurons in one layer. The lightness of grid sites indicates their level of contribution towards the decision of the classifier for the different micropatterns tested. In the case of the larger patterns **(A–D)**, site importance is concentrated around the centre of the pattern, whereas smaller patterns more consistently use sites throughout the pattern to evaluate a structure for selective conduction block. This supports the conclusion that the vast majority of these proarrhythmic phenomena take place on smaller spatial scales.

same archetypal structure of channels connecting to open regions to produce unidirectional block is observed, although again identification by eye is significantly challenging. For example, structures exhibiting omnidirectional block (**Figures 9D,E**) do not seem to be immediately separable from those exhibiting unidirectional block (**Figures 9A–C,G–I**), but only the latter structures are able to initiate a re-entry. Our classifier model allows for the identification of this property beyond a simple human search for the obvious, qualitative patterns.

However, some patterns that show unidirectional block when simulated were not detected by the NN classifier, despite its high accuracy on the data originally used to test its performance. There could be several reasons for this. The unidirectional block events observed in false-negative cases often occur very close to the micropattern boundary (**Figures 9H,I**). In such cases, there is insufficient information about the structure around the wavefront at the critical location of the block, and so the classifier model struggles to predict it. Additionally, in these smaller-scale simulations, many more of the micropatterns evaluated for testing will fall closer to the domain boundaries, where the balance of source and sink can be affected by the initial stimulus and the inability of travelling wavefronts to form their full 'tail' of activated cells that provide an additional electrotonic sources of depolarisation. This is likely due to the fact that the structure responsible for conduction block (unidirectional or otherwise) will not precisely coincide with the location where the wavefront dies out. We discuss this further in Conclusions.

4. CONCLUSIONS

We have used high-throughput simulation to approach an exhaustive exploration of the issue of re-entry initiation in fibrosis-afflicted tissue, a key precursor to arrhythmia (Hansen et al., 2015; Sachetto Oliveira et al., 2018a). It is known, at least for randomly placed obstructions as considered here, that the probability a site is obstructed is a critical determinant of re-entry formation (Vigmond et al., 2016; Sachetto Oliveira et al., 2018b). This finding was recapitulated in this study, for a different type of computational mesh and was extended by also exploring how different patterns of activation interact with these regions of afflicted tissue. In particular, we have demonstrated that for the most risk-associated extents of fibrosis ($\rho \sim 0.49$), a majority of fibrotic realisations were in fact capable of initiating re-entry from a single stimulus but only for waves sourcing from a select few pattern-specific locations. This suggests that lower rates of initiation previously reported (Sachetto Oliveira et al., 2018b) are largely a function of only a single stimulus pattern being considered in that study. This additionally sheds light on one role of ectopic beats in arrhythmia initiation; if one of the stimulus scenarios is said to correspond to a healthy sinus rhythm activation pattern, then the other stimulus scenarios are related to events such as premature contractions and can often initiate re-entry even when the typical activation sequence does not.

Although we observed activation sequence to be similarly as important as structure in terms of producing re-entrant waves that escape the scar region, the fine-scale events of selective block required to initiate any re-entrant activity were not expected to be overly dependent on activation sequence. This intuition was seen to hold, with a NN classifier model trained only using binary arrays of fibrosis occupancy (no activation pattern information) obtaining very good accuracy (up to 91% for this very challenging learning problem). We also used classifier accuracy to suggest the important length scale for identifying the unidirectional block in these fibrotic micropatterns, observing

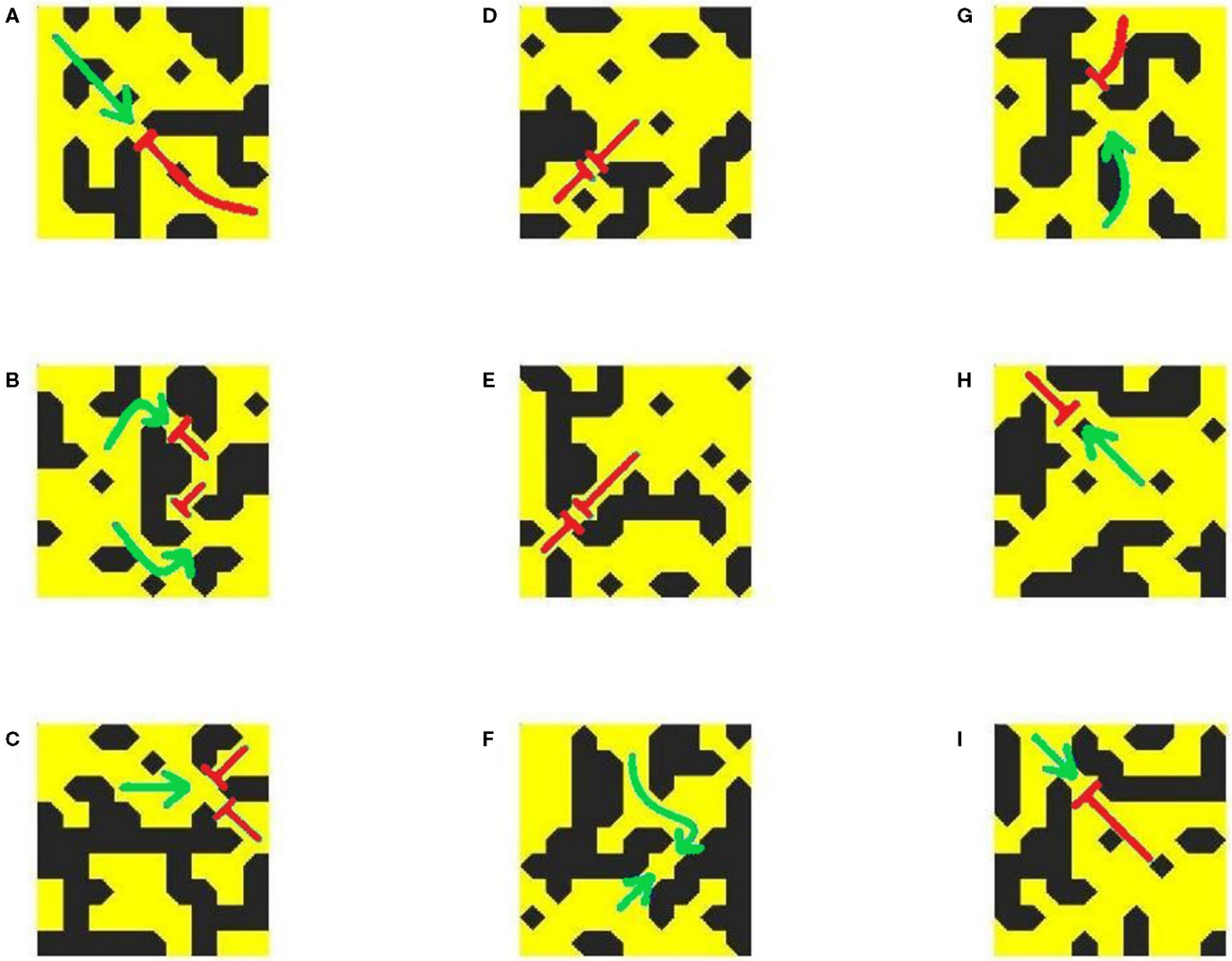

FIGURE 9 | Conduction patterns in completely unseen structures from new simulations, and the corresponding predictions of the classifier model. Shown are examples of correctly identified pro-arrhythmic **(A–C)** and non-arrhythmogenic **(D–F)** micropatterns, and undetected pro-arrhythmic **(G–I)** micropatterns. All are of size 9×9 elements. Green arrows indicate the directions of AP propagation, with red flat arrowheads indicating conduction block. Notably, the classifier model can successfully identify structures that result in a complete block from all directions **(D,E)** but could not successfully identify all pro-arrhythmic structures, particularly those where block occurs near the micropattern boundary **(H,I)**.

9×9 patterns to best balance information content and learning problem dimensionality for the NNs. This suggests the effective length scale for individual events of unidirectional (or other selective) conduction block to be ~ 0.5 mm or a little larger.

When the classifier was tested on completely new data (new simulations not used for training, validation, or testing), it remained able to detect the key structures involved in generating unidirectional block events. Impressively, completely-blocking structures (i.e., blocking from all directions) could be correctly classified. This more challenging test of the classifier model did expose some of the limitations of the approach used in this study, however. First, our RVI-based detection method picks out the locations where activation dies out, but this does not always perfectly correspond to the structure most responsible for the failure to propagate. For example, a wavefront emerging from a thin channel into a bay of excitable tissue may die out a little way into the bay, even though the structure surrounding where the channel ends is the most important. One potential direction forward is improving the block detection algorithm, so it better localises the structure responsible for the unidirectional block instead of wave die-out points. Another direction is to move away from detecting specific sites of unidirectional block altogether, and instead attempt to classify micropatterns using data generated by simulating AP propagation across the micro patterns themselves.

As the focus of this study was purely on how much fibrotic structure itself can inform the risk of re-entry, we have not considered the importance of specific electrophysiological conditions for the initiation and sustainment of re-entrant activation patterns. Some examination of the effects of parameter

variability in this context has already been carried out (Lawson et al., 2020), but it is a limitation of this study that we have not explicitly considered how different electrophysiological conditions impact the importance of structure vs. activation sequence or the ability to predict structures that selectively block. We suspect that if the conductivity of unobstructed tissue was adjusted, or a different cell model (or parameter values for the BOCF model) was used, the general conclusions we have drawn here would remain valid, but of course classifier models would need to be retrained. Anisotropic conduction, in particular, might also have a pronounced effect on our observations here, especially considering that different 'textures' of fibrosis meaningfully act to change the effective anisotropy of afflicted tissue (Nezlobinsky et al., 2020).

We have used a generously sized region of afflicted tissue for data generation in this study, larger than the minimal size required to support re-entry in similar simulations (Sachetto Oliveira et al., 2018b) and larger than micro-re-entrant paths observed in explanted hearts (Hansen et al., 2015). Domain size certainly effects the probability of observing a sustained re-entry, but the observation that the direction of the initial wavefront is critical for re-entry initiation should be robust to the domain size. We have demonstrated that the individual micro-structures that do or do not exhibit selective or unidirecitonal block act on a length scale of about $\sim$0.5 mm, much smaller than the size of the full simulation domain. A bigger limitation of our choice of domain is its two-dimensional nature, a necessity for carrying out the number of simulations performed here. In three-dimensions, critical length scales and fibrotic extents of highest risk would be expected to change, owing to the differences in source/sink balance (Xie et al., 2010; Sachetto Oliveira et al., 2018b).

In summary, a new pipeline was implemented to generate two datasets for pro-arrhythmic and non-arrhythmic fibrotic patterns. The pipeline involves simulations of re-entries within fibrotic substrates augmented by stimulations coming from multiple sites and the automatic identification of unidirectional blocks *via* the RVI method. These datasets were used to train and test a neural network that was able to successfully classify (accuracy up to 91%) micropatterns by only taking as input their structures. Therefore, our results suggest that machine learning provides tools that can be further exploited to address fundamental questions such as the relationship between anatomical heterogeneity and re-entry risk, and over what spatial scale this heterogeneity should be considered.

DATA AVAILABILITY STATEMENT

The raw data supporting the conclusions of this article will be made available by the authors, without undue reservation.

AUTHOR CONTRIBUTIONS

RH and BL created the simulation tools used. RH performed the training and testing of neural network classifiers and created tools used in visualising results. All authors contributed to the analysis of results and subsequent development of the study, original study concept, and drafting of the manuscript.

FUNDING

This work was supported by the Ministry of Education, Youth and Sports from the Large Infrastructures for Research, Experimental Development, and Innovations project e-INFRA CZ-LM2018140, Technology Agency of the Czech Republic: TN01000013. This work was partially supported by CNPq, FAPEMIG, CAPES, and UFJF, Brazil, and by the ARC Centre of Excellence for Mathematical and Statistical Frontiers (CE140100049).

ACKNOWLEDGMENTS

RH would like to thank ACEMS for hosting his visit to the Queensland University of Technology in March 2020, and IT4Innovations for supporting this internship.

SUPPLEMENTARY MATERIAL

The Supplementary Material for this article can be found online at: https://www.frontiersin.org/articles/10.3389/fphys.2021.709485/full#supplementary-material

REFERENCES

Alonso, S., dos Santos, R. W., and Bär, M. (2016). Reentry and ectopic pacemakers emerge in a three-dimensional model for a slab of cardiac tissue with diffuse microfibrosis near the percolation threshold. *PLoS ONE* 11:e0166972. doi: 10.1371/journal.pone.0166972

Bueno-Orovio, A., Cherry, E., and Fenton, F. (2008). Minimal model for human ventricular action potentials in tissue. *J. Theor. Biol.* 253, 544–560. doi: 10.1016/j.jtbi.2008.03.029

Cherry, E. M., Ehrlich, J. R., Nattel, S., and Fenton, F. H. (2007). Pulmonary vein reentry—properties and size matter: insights from a computational analysis. *Heart rhythm* 4, 1553–1562. doi: 10.1016/j.hrthm.2007.08.017

Chollet, Francois et al. (2015). *Keras. GitHub*. Available online at: https://github.com/fchollet/keras.

Ciaccio, E. J., Coromilas, J., Wit, A. L., Peters, N. S., and Garan, H. (2018). Source-sink mismatch causing functional conduction block in re-entrant ventricular tachycardia. *JACC Clin. Electrophysiol.* 4, 1–16. doi: 10.1016/j.jacep.2017.08.019

Clayton, R. H. (2018). Dispersion of recovery and vulnerability to re-entry in a model of human atrial tissue with simulated diffuse and focal patterns of fibrosis. *Front. Physiol.* 9:1052. doi: 10.3389/fphys.2018.01052

de Jong, S., van Veen, T. A. B., van Rijen, H. V. M., and de Bakker, J. M. T. (2011). Fibrosis and cardiac arrhythmias. *J. Cardiovasc. Pharmacol.* 57, 630–638. doi: 10.1097/FJC.0b013e318207a35f

Duffy, H. S. (2012). The molecular mechanisms of gap junction remodeling. *Heart Rhythm* 9, 1331–1334. doi: 10.1016/j.hrthm.2011.11.048

Gough, W. B., Mehra, R., Restivo, M., Zeiler, R. H., and El-Sherif, N. (1985). Reentrant ventricular arrhythmias in the late myocardial infarction period in the dog: correlation of activation and refractory maps. *Circ. Res.* 57, 432–442. doi: 10.1161/01.RES.57.3.432

Gouvêa de Barros, B., Weber dos Santos, R., Lobosco, M., and Alonso, S. (2015). Simulation of ectopic pacemakers in the heart: multiple ectopic beats

generated by reentry inside fibrotic regions. *Biomed Res. Int*. 2015:713058. doi: 10.1155/2015/713058

Hansen, B. J., Zhao, J., Csepe, T. A., Moore, B. T., Li, N., Jayne, L. A., et al. (2015). Atrial fibrillation driven by micro-anatomic intramural re-entry revealed by simultaneous sub-epicardial and sub-endocardial optical mapping in explanted human hearts. *Eur. Heart J.* 36, 2390–2401. doi: 10.1093/eurheartj/ehv233

Hinderer, S., and Schenke-Layland, K. (2019). Cardiac fibrosis-a short review of causes and therapeutic strategies. *Adv. Drug Deliv. Rev*. 146, 77–82. doi: 10.1016/j.addr.2019.05.011

Hubbard, M. L., and Henriquez, C. S. (2014). A microstructural model of reentry arising from focal breakthrough at sites of source-load mismatch in a central region of slow conduction. *Am. J. Physiol. Heart Circ. Physiol*. 306, H1341–H1352. doi: 10.1152/ajpheart.00385.2013

Jacquemet, V., and Henriquez, C. S. (2009). Genesis of complex fractionated atrial electrograms in zones of slow conduction: A computer model of microfibrosis. *Heart Rhythm* 6, 803–810. doi: 10.1016/j.hrthm.2009.02.026

Jakes, D., Burrage, K., Drovandi, C. C., Burrage, P., Bueno-Orovio, A., dos Santos, R. W., et al. (2019). Perlin noise generation of physiologically realistic patterns of fibrosis. *bioRxiv*. doi: 10.1101/668848

Kazbanov, I. V., Ten Tusscher, K. H., and Panfilov, A. V. (2016). Effects of heterogeneous diffuse fibrosis on arrhythmia dynamics and mechanism. *Sci. Rep*. 6:20835. doi: 10.1038/srep20835

Lawson, B. A. J., Oliveira, R. S., Berg, L. A., Silva, P. A. A., Burrage, K., and dos Santos, R. W. (2020). Variability in electrophysiological properties and conducting obstacles controls re-entry risk in heterogeneous ischaemic tissue. *Philos. Trans. R. Soc. A Math. Phys. Eng. Sci*. 378:20190341. doi: 10.1098/rsta.2019.0341

McDowell, K. S., Arevalo, H. J., Maleckar, M. M., and Trayanova, N. A. (2011). Susceptibility to arrhythmia in the infarcted heart depends on myofibroblast density. *Biophys. J.* 101, 1307–1315. doi: 10.1016/j.bpj.2011.08.009

McDowell, K. S., Zahid, S., Vadakkumpadan, F., Blauer, J., MacLeod, R. S., and Trayanova, N. A. (2015). Virtual electrophysiological study of atrial fibrillation in fibrotic remodeling. *PLoS ONE* 10:e0117110. doi: 10.1371/journal.pone.0117110

Mincholé, A., Camps, J., Lyon, A., and Rodríguez, B. (2019). Machine learning in the electrocardiogram. *J. Electrocardiol*. 57, S61–S64. doi: 10.1016/j.jelectrocard.2019.08.008

Muffoletto, M., Fu, X., Roy, A., Varela, M., Bates, P. A., and Aslanidi, O. V. (2019). "Development of a deep learning method to predict optimal ablation patterns for atrial fibrillation, in *2019 IEEE Conference on Computational Intelligence in Bioinformatics and Computational Biology (CIBCB)* (Siena, IEEE), 1–4.

Muffoletto, M., Qureshi, A., Zeidan, A., Muizniece, L., Fu, X., Zhao, J., et al. (2021). Toward patient-specific prediction of ablation strategies for atrial fibrillation using deep learning. *Front. Physiol*. 12:674106. doi: 10.3389/fphys.2021.674106

Nezlobinsky, T., Solovyova, O., and Panfilov, A. V. (2020). Anisotropic conduction in the myocardium due to fibrosis: the effect of texture on wave propagation. *Sci. Rep*. 10:764. doi: 10.1038/s41598-020-57449-1

Nguyen, T. P., Qu, Z., and Weiss, J. N. (2014). Cardiac fibrosis and arrhythmogenesis: The road to repair is paved with perils. *J. Mol. Cell. Cardiol*. 70, 83–91. doi: 10.1016/j.yjmcc.2013.10.018

Orini, M., Graham, A., Srinivasan, N., Campos, F., Hanson, B., Chow, A., et al. (2019). Evaluation of the re-entry vulnerability index to predict ventricular tachycardia circuits using high density contact mapping. *Heart Rhythm* 17, 576–583. doi: 10.1016/j.hrthm.2019.11.013

Orini, M., Taggart, P., Hayward, M., and Lambiase, P. D. (2017). "Optimization of the global re-entry vulnerability index to minimise cycle length dependency and prediction of ventricular arrhythmias during human epicardial sock mapping, in *2017 Computing in Cardiology (CinC)*, (Rennes) 1–4.

Pathmanathan, P., Bernabeu, M. O., Niederer, S. A., Gavaghan, D. J., and Kay, D. (2012). Computational modelling of cardiac electrophysiology: explanation of the variability of results from different numerical solvers. *Int. J. Num. Methods Biomed. Eng*. 28, 890–903. doi: 10.1002/cnm.2467

Perego, M., and Veneziani, A. (2009). An efficient generalization of the Rush-Larsen method for solving electro-physiology membrane equations. *Elecr. Trans. Num. Anal*. 35, 234–256.

Quan, W., and Rudy, Y. (1990). Unidirectional block and reentry of cardiac excitation: a model study. *Circ. Res*. 66, 367–382. doi: 10.1161/01.RES.66.2.367

Roy, A., Varela, M., Chubb, H., MacLeod, R., Hancox, J. C., Schaeffter, T., et al. (2020). Identifying locations of re-entrant drivers from patient-specific distribution of fibrosis in the left atrium. *PLoS Comput. Biol*. 16, 1–25. doi: 10.1371/journal.pcbi.1008086

Sachetto Oliveira, R., Alonso, S., Campos, F.ernando, O., Rocha, B. M., Fernandes, J. F., Kuehne, T., et al. (2018a). Ectopic beats arise from micro-reentries near infarct regions in simulations of a patient-specific heart model. *Sci. Rep*. 8:16392. doi: 10.1038/s41598-018-34304-y

Sachetto Oliveira, R., Alonso, S., and Weber dos Santos, R. (2018b). Killing many birds with two stones: hypoxia and fibrosis can generate ectopic beats in a human ventricular model. *Front. Physiol*. 9:764. doi: 10.3389/fphys.2018.00764

Shade, J. K., Ali, R. L., Basile, D., Popescu, D., Akhtar, T., Marine, J. E., et al. (2020). Preprocedure application of machine learning and mechanistic simulations predicts likelihood of paroxysmal atrial fibrillation recurrence following pulmonary vein isolation. *Circulation* 13:e008213. doi: 10.1161/CIRCEP.119.008213

Shaw, R. M., and Rudy, Y. (1997). Electrophysiologic effects of acute myocardial ischemia: a theoretical study of altered cell excitability and action potential duration. *Cardiovasc. Res*. 35, 256–272. doi: 10.1016/S0008-6363(97)00093-X

Sundnes, J., Lines, G. T., Cai, X., Nielsen, B. F., Mardal, K., and Tveito, A. (2006). *Computing the Electrical Activity in the Heart*. Berlin: Springer-Verlag.

Ten Tusscher, K. H., and Panfilov, A. V. (2007). Influence of diffuse fibrosis on wave propagation in human ventricular tissue. *Europace* 9(Suppl. 6):vi38–vi45. doi: 10.1093/europace/eum206

Vigmond, E., Pashaei, A., Amraoui, S., Cochet, H., and Hassaguerre, M. (2016). Percolation as a mechanism to explain atrial fractionated electrograms and reentry in a fibrosis model based on imaging data. *Heart Rhythm* 13, 1536–1543. doi: 10.1016/j.hrthm.2016.03.019

Xie, Y., Sato, D., Garfinkel, A., Qu, Z., and Weiss, J. N. (2010). So little source, so much sink: requirements for afterdepolarizations to propagate in tissue. *Biophys. J.* 99, 1408–1415. doi: 10.1016/j.bpj.2010.06.042

Yang, T., Yu, L., Qi, J., Wu, L., and He, B. (2018). Localization of origins of premature ventricular contraction by means of convolutional neural network from 12-lead ECG. *IEEE Trans. Biom. Eng.* 65, 1662–1671. doi: 10.1109/TBME.2017.2756869

Zahid, S., Cochet, H., Boyle, P. M., Schwarz, E. L., Whyte, K. N., Vigmond, E. J., et al. (2016). Patient-derived models link re-entrant driver localization in atrial fibrillation to fibrosis spatial pattern. *Cardiovasc. Res*. 110, 443–454. doi: 10.1093/cvr/cvw073

Conflict of Interest: The authors declare that the research was conducted in the absence of any commercial or financial relationships that could be construed as a potential conflict of interest.

Publisher's Note: All claims expressed in this article are solely those of the authors and do not necessarily represent those of their affiliated organizations, or those of the publisher, the editors and the reviewers. Any product that may be evaluated in this article, or claim that may be made by its manufacturer, is not guaranteed or endorsed by the publisher.

Characterization of cardiac cell electrophysiology model using recurrence plots

Radek Halfar

Abstract The main aim of this paper is to analyse the evolution of cardiac cell transmembrane potential forced by periodic pacing. For this purpose, the Beeler-Reuter model of ventricular cardiac cell is used. The Beeler-Reuter model is a well stated mathematical model of a cardiac ventricular cell. Many papers dealing with heart electrophysiology using this model for its great properties. In this paper, the model is forced by pacing stimulus with the shape of the half-sine period followed by zero function. The computed model motions are investigated using the recurrence plots, recurrence quantification analysis, and approximate entropy with respect to the pacing period.

1 Introduction

Since heart diseases are the most common cause of death in the world [19, 5] it is very important to understand the proper heart work. The mechanical heart work is governed by electrical impulses generated by the heart itself. These impulses propagate through the heart and make the heart pump blood into the body. Therefore on the proper propagation of these impulses depends on each individual's life.

In this paper, the recurrence plots and recurrence quantification analysis (RQA) are used for investigation of dynamic of the Beeler-Reuter cardiac cell model of transmembrane potential and the influence of the pacing period to this dynamic.

Since its introduction in 1987 by Eckmann et al. [7] recurrence plot (RP) became an important tool for the investigation of the dynamical system. Since then, RPs were successfully used for authentication in the Internet of Things [2], automatic Parkinsons disease identification [1], investigation of heart rate variability [16] and many others.

IT4Innovations, VSB - Technical University of Ostrava, 17. listopadu 15/2172, 708 33 Ostrava, Czech Republic, e-mail: radek.halfar@vsb.cz

2 Beeler-Reuter model

The Beeler-Reuter model of the cardiac cell proposed by Beeler and Reuter in 1977 [3]. Model is established by eight Equations (1) defining the time derivatives of transmembrane potential V_m in mV, intracellular Ca^{2+} concentration $[Ca]_i$ in mole/l, and six dimensionless gating variables x_1, m, h, j, d, and f. Gating variables are in Equations (1) modelled as variable y (difference in equations for the particular gating variables is given by constants).

$$\begin{aligned} \frac{dV_m}{dt} &= \frac{i_{ext} - i_{k_1} - i_{x_1} - i_{Na} - i_{Ca}}{C_m}, \\ \frac{d[Ca]_i}{dt} &= -10^{-7} i_s + 0.07(10^{-7} - [Ca]_i), \\ \frac{dy}{dt} &= \frac{y_\infty - y}{\tau_y}. \end{aligned} \tag{1}$$

Times t and τ are in ms. Parameter C_m defines membrane capacitance in μF/cm^2 (in this study $C_m = 1$). Detailed information about the Beeler-Reuter model can be seen in [3]. Typical ventricular transmembrane potential computed using Beeler-Reuter model can be seen in Fig. 1.

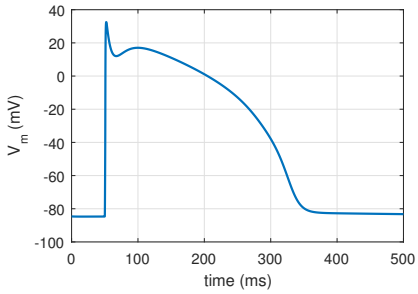

Fig. 1 Transmembrane potential (variable V_m) of stimulated ventricular cardiac cell computed using Beeler-Reuter model.

In this paper, the externally applied current i_{ext} are impulses with a duration of 1 ms and amplitude of 80 μA/cm^2 created by the first half period of the sine function followed by the zero function. Variable i_{ext} is therefore defined by the following equation:

$$i_{ext} = \begin{cases} 80\sin(\pi(t - n(c+1))) & t \in [n(c+1), n(c+1)+1], \\ 0 & t \notin [n(c+1), n(c+1)+1]. \end{cases}$$

The graphical representation of variable i_{ext} can be seen in Fig. 2.

The model equations were solved numerically using the variable order solver based on the numerical differentiation formulas implemented as an *ode15s* solver in MATLAB [17]. The computations were performed for the stimulation delays c from 10 to 365 ms with a step of 5 ms. Each simulation was done for the time from 0

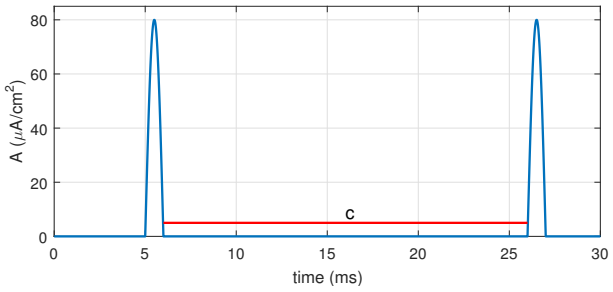

Fig. 2 Stimulation function i_{ext} for $A = 80\ \mu\text{A/cm}^2$, and $c = 20$ ms. Parameter c is labeled by red color.

to 10^5 ms. Subsequent analysis of resulting transmembrane potential using RP was performed in R [18] designed by R Core Team using packages *nonlinearTseries* [8] and *fractal* package [6].

3 Main results

In order to exclude transient phenomena, the only transmembrane potential (variable V_m) from 90×10^3 to 10^5 ms were analyzed. From this time period, the values for subsequent analysis were selected with 1 ms time step. The investigated time series is thus a length of 10001 data points.

3.1 Recurrence plots

From this time series, the time delay was firstly estimated. This estimation was computed using *fractal* package [6] by the first zero crossing of the autocorrelation function. Next, the number of embedding dimension was estimated by the algorithm suggested by L. Cao [4] and calculated using *nonlinearTseries* package [8]. The threshold for defining to states as a recurrence was selected as a 3% of phase space diameter.

Next, the recurrence plots were computed using *nonlinearTseries* package. Resulting RPs can be divided into two groups. One group consists of RP made by long and uninterrupted diagonal lines ($c \in [10,25] \cup [35,40] \cup [55,60] \cup [75,85] \cup [105,125] \cup [145,365]$). Example of this RP is shown in Fig. 3. In this figure, the periodic motion of the calculated transmembrane potential is revealed. The period of the oscillation corresponds to the vertical distance between lines in RP.

In Fig. 4 is depicted graph of given pacing impulses needed for one recurrence of the model.

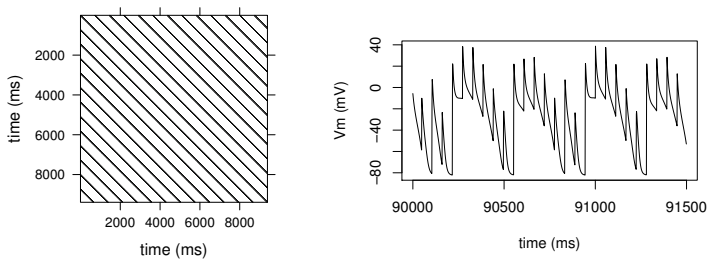

Fig. 3 Resulting reccurence plot (left) and transmembrane potential (right) for $c = 55$ ms.

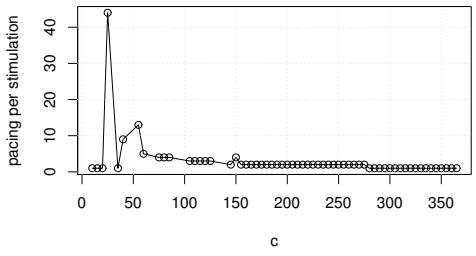

Fig. 4 Graph of given stimulus per one stimulation.

In this figure can be seen, that for stimulation delays $c \in [10,20] \cup \{35\}$ ms is only one stimulation needed for model recurrence. With respect to the short stimulation period it can be derived, that the model did not enter the rest phase and the transmembrane potential changes within a short range of voltage (see Fig. 5). For the stimulation delay $c = 25$ ms can be seen, that for one recurrence is more than 40 stimulation. For this delay, a triangular signal generated by rapid pacing of the model is superimposed on the proper transmembrane potential (see Fig. 1 and Fig. 5). For $c \geq 40$ are unsuccessful pacing pulses superimposed on the transmembrane potential and the number of the stimulation impulses per recurrence is dropping (with exception of $c = \{55,150\}$).

In the second case, the diagonals are interrupted ($c \in \{30\} \cup [45,50] \cup [65,70] \cup [130,140]$). Examples of these RPs can be seen in Fig. 6 and 7. These lines represent time intervals, where the trajectory in the phase space runs parallel to another sequence of this trajectory (dynamics is similar). In RPs can also be seen certain vertical distances, but these distances are not as regular as in the previous case. In several cases in this group can be seen a small rectangular patch which rather looks like the RP of the periodic motion (see Fig. 7). This structure reveals an unstable periodic orbit.

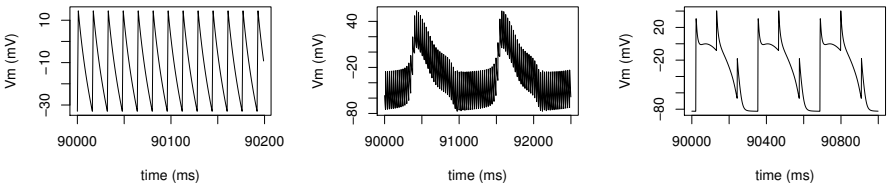

Fig. 5 Transmembrane potential for $c = 15$ ms (left), $c = 25$ ms (middle), and $c = 110$ ms (right).

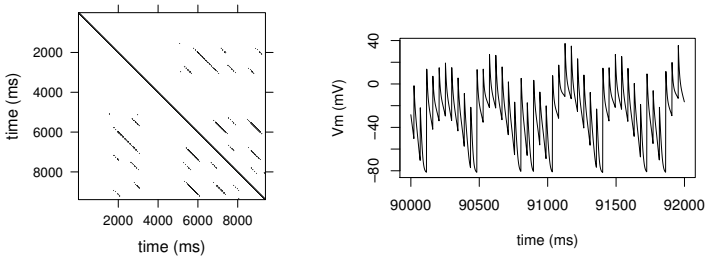

Fig. 6 Resulting reccurence plot (left) and transmembrane potential (right) for $c = 45$ ms.

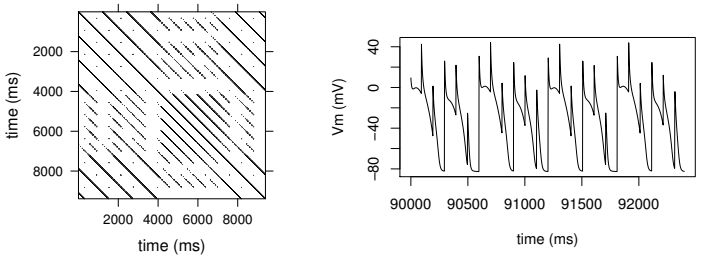

Fig. 7 Resulting reccurence plot (Left) and transmembrane potential (right) for $c = 100$ ms.

3.2 Recurrence quantification analysis

Next, the recurrence quantification analysis (RQA) was computed. RQA is a method that belongs to nonlinear data analysis. This technique quantifies the number and duration of recurrences of a dynamical system in state space. Details about RQA can be founded in [15]. These calculation were performed in R using *nonlinearTseries* package [8]. The resulting RPs were analyzed using several measures. The best results were achieved by calculating the length of the longest diagonal line (L_{max}) and the ratio between the percentage of diagonal lines in the RP DET, and density

of recurrence points in a recurrence plot *RR*. Results of RQA can be seen in Fig. 8. In this figure can be seen that the length of the longest diagonal line can be divided into two groups. One group consist of RPs with $L_{max} \leq 8000$. This RPs can be seen for $c \in \{25,30,45,50,65,70\} \cup [90,100] \cup [130,140]$, and the RP with $L_{max} > 8000$ which was observed elsewhere. The measure $ratio$ divides the RP into two groups as well. For the RP with $ratio \geq 500$ for the stimulation delays $c \in \{25,45,50,65,70\} \cup [90,100] \cup \{130,135\}$ and for $ratio < 500$ observed elsewhere. Notice, that results of RQA correspond to the observations made using RPs.

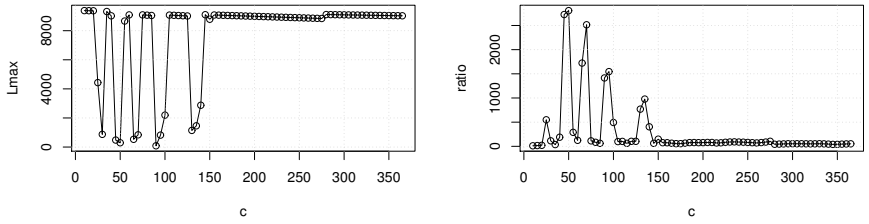

Fig. 8 Results of RQA for L_{max} (left) and $ratio$ (right).

3.3 Approximate entropy

Next, the approximate entropy (ApEn) was computed. This technique allows comparing the complexity of the system with different parameters setting. Another advantage of this method is that it can be calculated in a short time series. For more details about approximate entropy see [14, 13].

The calculations of this technique were performed in R using the *TSEntropies* package. Neighborhood threshold r was defined as a 10% of phase space diameter. The ApEn of Beeler-Reuter model can be seen in Fig. 9. In this figure can be seen an increase of complexity around stimulation delay 30, 45, 70, 90, and 135 ms. Local extrema on similar values of c can be seen also in Fig. 8. In this figure can be seen that results of RQA (Fig. 8) and ApEn (Fig. 9) coincide for most values of parameter c.

4 Conclusions

In this paper, the transmembrane potential calculated using the Beeler-Reuter model was analyzed with respect to the stimulation period. The model (1) was paced by

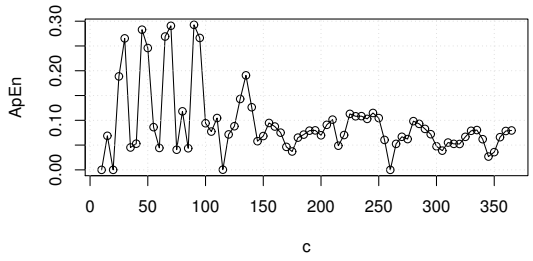

Fig. 9 Results of the approximate entropy.

the stimulus with the shape of the half-sine period. For the solving model equations, variable order solver based on the numerical differentiation formulas implemented as an *ode15s* solver in MATLAB was used.

It was observed, that with periodical forcing the model shows periodic as well as non-periodic motions and the complexity of data vary with stimulation period. For the evaluation of motion, the recurrence plots, recurrence quantification analysis (see Fig. 8), and approximate entropy (see Fig. 9) were used.

The achieved results can be compared to the investigation of the Beeler-Reuter model using the 0-1 test for chaos published in [11]. This test was designed to distinguish regular and chaotic dynamics. The resulting value of this test close to 0 shows regular behaviour, and result close to 1 shows chaotic motion. For more detailed description of this test see [9, 10].

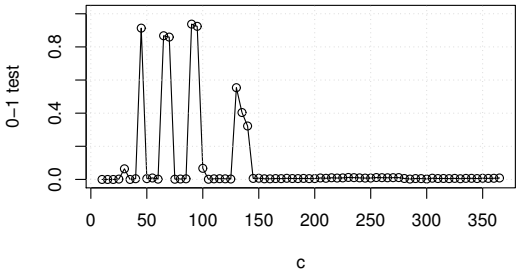

Fig. 10 Results of the 0-1 test for chaos.

Comparing Fig. 8 and 10 can be seen, that the result of RQA and the 0-1 test for chaos coincide in most values. The difference (the 0-1 test for chaos indicates regular motion and the $ratio \geq 500$ or $L_{max} \leq 8000$ and vise versa) in these figures can be

found for $c \in \{25, 30, 50, 100\}$ for RQA measure L_{max}, and for $c \in \{25, 50, 100, 140\}$ for RQA measure *ratio*. The achieved results can be also compared with paper [12], where dynamical properties of modified Fenton-Karma model of the heart cell was investigated.

Acknowledgements This work was supported by The Ministry of Education, Youth and Sports from the National Programme of Sustainability (NPU II) project "IT4Innovations excellence in science – LQ1602"; by The Ministry of Education, Youth and Sports from the Large Infrastructures for Research, Experimental Development and Innovations project "IT4Innovations National Supercomputing Center – LM2015070"; by SGC grant No. SP2019/125 "Qualification and quantification tools application to dynamical systems", VŠB - Technical University of Ostrava, Czech Republic.

References

1. Afonso, L.C., Rosa, G.H., Pereira, C.R., Weber, S.A., Hook, C., Albuquerque, V.H.C., Papa, J.P.: A recurrence plot-based approach for parkinsons disease identification. Future Generation Computer Systems **94**, 282 – 292 (2019). DOI https://doi.org/10.1016/j.future.2018.11.054. URL http://www.sciencedirect.com/science/article/pii/S0167739X18322507
2. Baldini, G., Giuliani, R., Dimc, F.: Physical layer authentication of internet of things wireless devices using convolutional neural networks and recurrence plots. Internet Technology Letters (2018). DOI 10.1002/itl2.81
3. Beeler, G.W., Reuter, H.: Reconstruction of the action potential of ventricular myocardial fibres. The Journal of Physiology **268**(1), 177–210 (1977). DOI 10.1113/jphysiol.1977.sp011853. URL https://physoc.onlinelibrary.wiley.com/doi/abs/10.1113/jphysiol.1977.sp011853
4. Cao, L.: Practical method for determining the minimum embedding dimension of a scalar time series. Physica D: Nonlinear Phenomena **110**, 43–50 (1997). DOI 10.1016/S0167-2789(97)00118-8
5. Centers for Disease Control and Prevention: Leading causes of death. https://www.cdc.gov/nchs/fastats/leading-causes-of-death.htm (2017). [Online; accessed 29-May-2019]
6. Constantine, W., Percival, D.: fractal: A Fractal Time Series Modeling and Analysis Package (2017). URL https://CRAN.R-project.org/package=fractal. R package version 2.0-4
7. Eckmann, J.P., Kamphorst, S.O., Ruelle, D.: Recurrence plots of dynamical systems. Europhysics Letters (EPL) **4**(9), 973–977 (1987). DOI 10.1209/0295-5075/4/9/004. URL https://doi.org/10.1209%2F0295-5075%2F4%2F9%2F004
8. Garcia, C.A.: nonlinearTseries: Nonlinear Time Series Analysis (2018). URL https://CRAN.R-project.org/package=nonlinearTseries. R package version 0.2.5
9. Gottwald, A., Melbourne, I.: A new test for chaos in deterministic systems. Proc. R. Soc. London A **460**, 603–611 (2004)
10. Gottwald, A., Melbourne, I.: On the implementation of the 0-1 test for chaos. SIAM J. Appl. Dyn. **8**, 129–145 (2009)
11. Halfar, R.: Dynamical properties of beeler-reuter cardiac cell model with respect to stimulation parameters. International Journal of Computer Mathematics (-to appear)
12. Halfar, R., Lampart, M.: Dynamical properties of the improved FK3V heart cell model. Mathematical Methods in the Applied Sciences **41**, 7472–7480 (2018). DOI 10.1002/mma.5060

13. K. L. Ho, K., B Moody, G., Peng, C.K., E Mietus, J., G Larson, M., Levy, D., Goldberger, A.: Predicting survival in heart failure case and control subjects by use of fully automated methods for deriving nonlinear and conventional indices of heart rate dynamics. Circulation **96**, 842–8 (1997). DOI 10.1161/01.CIR.96.3.842
14. Lampart, M., Martinovi, T.: Chaotic behavior of the cml model with respect to the state and coupling parameters. Journal of Mathematical Chemistry (2019). DOI 10.1007/s10910-019-01023-2
15. Marwan, N., Romano, M.C., Thiel, M., Kurths, J.: Recurrence plots for the analysis of complex systems. Physics Reports **438**(5), 237 – 329 (2007). DOI https://doi.org/10.1016/j.physrep.2006.11.001. URL http://www.sciencedirect.com/science/article/pii/S0370157306004066
16. Marwan, N., Wessel, N., Meyerfeldt, U., Schirdewan, A., Kurths, J.: Recurrence-plot-based measures of complexity and their application to heart-rate-variability data. Physical Review E **66**, 026,702 (2002). DOI 10.1103/PhysRevE.66.026702
17. Matlab (2016a). The MathWorks, Inc., Natick, Massachusetts, United States.
18. Team, R.C.: R: A Language and Environment for Statistical Computing. R Foundation for Statistical Computing, Vienna, Austria (2018). URL https://www.R-project.org/
19. World Health Organization: The top 10 causes of death. http://www.who.int/mediacentre/factsheets/fs310/en/ (2017). [Online; accessed 10-May-2018]

Motions of the human cardiac cell electrophysiology model

Radek Halfar
VSB - Technical University of Ostrava, IT4Innovations, Czech Republic
E-mail: radek.halfar@vsb.cz

Abstract. One of the many processes in the human body on which our lives depend is the proper propagation of the electrical signal in the heart tissue. This propagation is dependent on the work of each heart cell, and even small variations in the synchronous work of these cells can lead to life-threatening conditions. A proper understanding of cardiac electrophysiology is therefore essential to understanding heart function and treating heart disease. In this work, cardiac electrophysiology is investigated using a mathematical model of a human ventricular cell (Bueno-Orovio-Cherry-Fenton model). This model is paced by regular stimulation impulses, and its responses to this stimulation are analyzed in terms of their dynamic properties, and the dependence of its dynamic parameters for the frequency and amplitude of stimulation. For this analysis, classical and modern tools from the field of dynamic systems theory (e.g. entropy measures, Fourier spectra, the 0-1 test for chaos) are used.

1. Introduction

The heart is a very complex organ on which work each person's life depends. It is controlled by electrical signals that determine our heart rate. With an improperly given electrical signal, the heart can enter a state of ventricular fibrillation that is incompatible with life. From the dynamic systems point of view, ventricular fibrillation is spatiotemporal chaos [1]. The dynamic properties of cardiac tissue are therefore examined in detail and many papers are dealing with this topic [2, 3, 4, 5]. Among such studies, we can mention, for example, works in which parameters are sought in which chaotic and regular responses of cardiac cell models occur [2, 3] or describes the transitions between the different types of the dynamic behavior of these models [5]. Researchers are also describing the behavior of ventricular fibrillation [4], and designing a control scheme to prevent instability in cardiac tissue [6].

In this work, the dynamic properties of the Bueno-Orovio-Cherry-Fenton model [7] are investigated. This model is paced by different amplitude and frequency settings. The responses of this model are then examined in terms of their regularity and complexity.

The paper is organized as follows. In Section 2, the Bueno-Orovio-Cherry-Fenton model is introduced. In Section 3, the main findings of this study are summarized. These main findings include time and frequency domain signal analysis in Subsection 3.1. Then using the 0-1 test for chaos for detection of chaotic and regular data in Subsection 3.2. The results of the complexity analysis of the obtained time series by entropy measure can be found in Subsection 3.3. Section 4 summarizes the main results of this study.

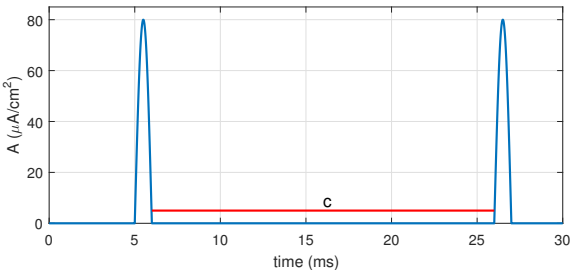

Figure 1. Stimulation function i_{ext} for $A = 80$ μA/cm^2, and $c = 20$ ms. Parameter c is labeled by red color.

2. Bueno-Orovio-Cherry-Fenton model

The Bueno-Orovio-Cherry-Fenton model of human ventricular cell [7] was designed in 2008 and is defined by 4 differential equations (see Equation (1)). With this model, 5 different sets of parameters are defined (see table 1) approximating the behavior of the epicardial, endocardial, and midmyocardial cells, as well as two other ionic models of human ventricular cells (Priebe-Beuckelmann and Ten Tusscher et al. models). In this work, a parameter set describing the epicardial cell is used.

$$\begin{aligned}
\partial_t u =& J_{stim} - (J_{fi} + J_{so} + J_{si}) \\
\partial_t v =& (1 - H(u - \theta_v))(v_\infty - v)/\tau_v^- - H(u - \theta_v)\, v/\tau_v^+ \\
\partial_t w =& (1 - H(u - \theta_w))(w_\infty - w)/\tau_w^- - H(u - \theta_w)\, w/\tau_w^+ \\
\partial_t s =& ((1 + \tanh(k_s(u - u_s)))/2 - s)/\tau_s
\end{aligned} \tag{1}$$

The equation describing the time derivation of the transmembrane potential $\partial_t u$ is described by ionic currents J_{fi} (defining membrane depolarization), J_{so} (defining membrane repolarization), and J_{si} (balances the current J_{so} during the plateau phase). The definitions of these curents can be seen in Equation (2).

$$\begin{aligned}
J_{fi} &= -vH(u - \theta_v)(u - \theta_v)(u_u - u)/\tau_{fi} \\
J_{so} &= (u - u_o)(1 - H(u - \theta_w))/\tau_o + H(u - \theta_w)/\tau_{so} \\
J_{si} &= -H(u - \theta_w)\, ws/\tau_{si}
\end{aligned} \tag{2}$$

J_{stim} describes the current that is applied to the cell externally. In this work, this current is formed by the composition of the zero function of length c and the first half of the period of a sinusoidal function with amplitude A. A graphical representation of this current can be seen in Figure 1. The equation of this current can be found in Equation (3).

$$i_{ext} = \begin{cases} A\sin(\pi(t - n(c+1))), & t \in [n(c+1), n(c+1)+1], \quad n \in \mathbb{N} \cup \{0\}, \\ 0, & t \notin [n(c+1), n(c+1)+1], \quad n \in \mathbb{N} \cup \{0\}. \end{cases} \tag{3}$$

In these equations, there are several time parameters described as a function of the transmembrane potential u. These functions are defined as follows:

$$\begin{aligned}
\tau_v^- &= \left(1 - H\left(u - \theta_v^-\right)\right)\tau_{v1}^- + H\left(u - \theta_v^-\right)\tau_{v2}^- \\
\tau_w^- &= \tau_{w1}^- + \left(\tau_{w2}^- - \tau_{w1}^-\right)\left(1 + \tanh\left(k_w^-\left(u - u_w^-\right)\right)\right)/2 \\
\tau_{so} &= \tau_{s01} + (\tau_{s02} - \tau_{s01})(1 + \tanh(k_{so}(u - u_{so})))/2 \\
\tau_s &= (1 - H(u - \theta_w))\tau_{s1} + H(u - \theta_w)\tau_{s2} \\
\tau_0 &= (1 - H(u - \theta_0))\tau_{01} + H(u - \theta_0)\tau_{02}.
\end{aligned} \tag{4}$$

Table 1. Model parameters [7].

Parameter	EPI	ENDO	M	PB	TNNP
u_o	0	0	0	0	0
u_u	1.55	1.56	1.61	1.45	1.58
θ_v	0.3	0.3	0.3	0.35	0.3
θ_w	0.13	0.13	0.13	0.13	0.015
θ_v^-	0.006	0.2	0.1	0.175	0.015
θ_o	0.006	0.006	0.005	0.006	0.006
τ_{v1}^-	60	75	80	10	60
τ_{v2}^-	1150	10	1.4506	1150	1150
τ_v^+	1.4506	1.4506	1.4506	1.4506	1.4506
τ_{w1}^-	60	6	70	140	70
τ_{w2}^-	15	140	8	6.25	20
k_w^-	65	200	200	65	65
u_w^-	0.03	0.016	0.016	0.015	0.03
τ_w^+	200	280	280	326	280
τ_{fi}	0.11	0.1	0.078	0.105	0.11
τ_{o1}	400	470	410	400	6
τ_{o2}	6	6	7	6	6
τ_{so1}	30.0181	40	91	30.0181	43
τ_{so2}	0.9957	1.2	0.8	0.9957	0.2
k_{so}	2.0458	2	2.1	2.0458	2
u_{so}	0.65	0.65	0.6	0.65	0.65
τ_{s1}	2.7342	2.7342	2.7342	2.7342	2.7342
τ_{s2}	16	2	4	16	3
k_s	2.0994	2.0994	2.0994	2.0994	2.0994
u_s	0.9087	0.9087	0.9087	0.9087	0.9087
τ_{si}	1.8875	2.9013	3.3849	1.8875	2.8723
$\tau_{w\infty}$	0.07	0.0273	0.01	0.175	0.07
w_∞^*	0.94	0.78	0.5	0.9	0.94

The values v_∞ and w_∞ are defined as

$$v_\infty = \begin{cases} 1, & u < \theta_v^- \\ 0, & u \geq 0_v^- \end{cases} \tag{5}$$

$$w_\infty = (1 - H(u - \theta_o))(1 - u/\tau_{w\infty}) + H(u - \theta_o)\, w_\infty^*.$$

In these equations $H(x)$ stands for standard Heaviside function.

3. Main results

In this work, the Bueno-Orovio-Cherry-Fenton model was paced using a stimulation current defined by Equation (3), and the influence of the amplitude and frequency of the stimulation current (parameter A and c) was investigated. The amplitude of the stimulation was varied from 0.45 to 1.00 in 0.025 steps. The c parameter was examined in the range of 30 to 117.5 ms with a step of 2.5 ms. Each simulation was numerically calculated in the time range from 0 to 500 s using the explicit Runge-Kutta (4,5) formula as a *ode45* solver in MATLAB. Due to the elimination of transients, the responses of the model in times from 0 to 250 s were removed. The time series thus obtained were subsampled using the stimulation frequency (1 sample was left in each stimulation period for future analysis).

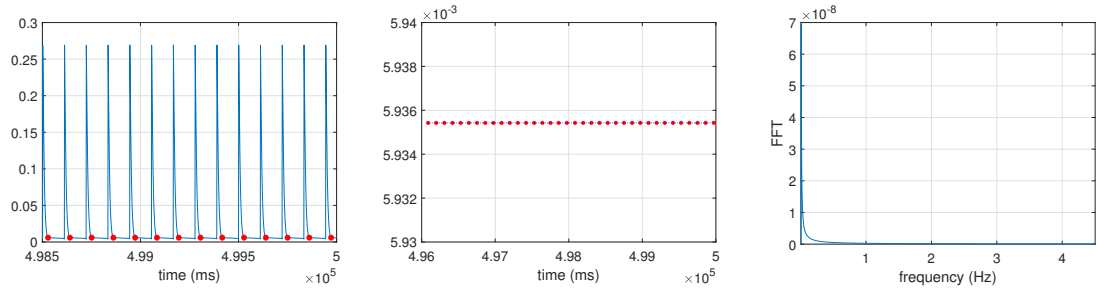

Figure 2. Results for $A = 0.45$, and $c = 110$ ms.Left figure: modeled action potential (blue) with depicted points, that are analyzed (red); middle figure: analyzed time series (red); right figure: Fourier spectrum of analyzed time series.

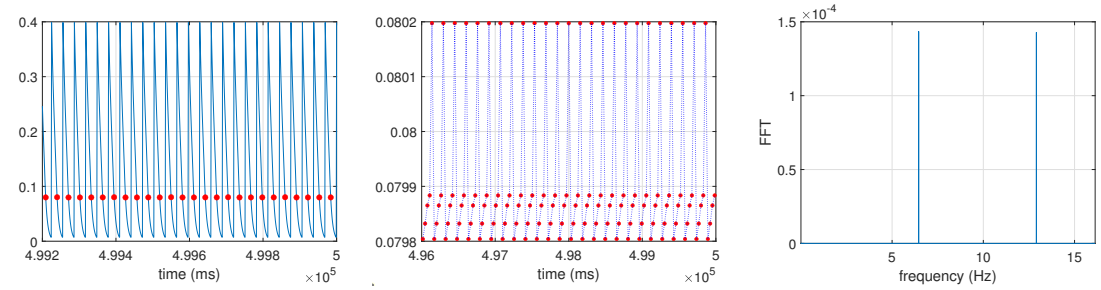

Figure 3. Results for $A = 0.65$, and $c = 30$ ms.Left figure: modeled action potential (blue) with depicted points, that are analyzed (red); middle figure: analyzed time series (red); right figure: Fourier spectrum of analyzed time series.

3.1. Time series, Fourier spectra, and bifurcation analysis
The responses of the examined model can be divided into 4 categories.

- In the first category, the stimulus current was not strong enough to create an action potential (mainly simulations where $A < 0.5$). Only the triangular signal generated by insufficient cell stimulation can be seen in the simulated transmembrane potential. The frequency spectrum consists only of discrete spikes, which imply the regular motion of a dynamic system in phase space. Examples of these time series can be seen in Figures 2 and 3.
- The second group is also formed by a current that insufficiently stimulates the heart cell (mostly $A < 0.5$). In these cases, however, the frequency spectrum is continuous, which indicates the irregular movement of the dynamic system. This case is shown in Figure 4.
- An action potential has already been created in this category and the responses of the model form a regular motion represented by a discrete frequency spectrum. These time series can be found mainly for $A < 0.5$ a $c \geq 60$ (see Figure 5).
- The action potential is formed by an irregular motion that forms a continuous frequency spectrum. These responses are typical for pacing delay $c < 60$ and pacing amplitude $A > 0.5$. An example of this time series can be found in Figure 6.

Next, bifurcation diagrams were plotted for 3 stimulation amplitudes $A = 0.55, 0.85, 1$ (see Figure 7). It can be seen from these diagrams that the irregular movement of the action potential is concentrated at higher stimulation frequencies and the regular movement is detected at higher values of the stimulation delay c (the bifurcation diagram is formed by individual points for these values of c). This corresponds to time series exploration.

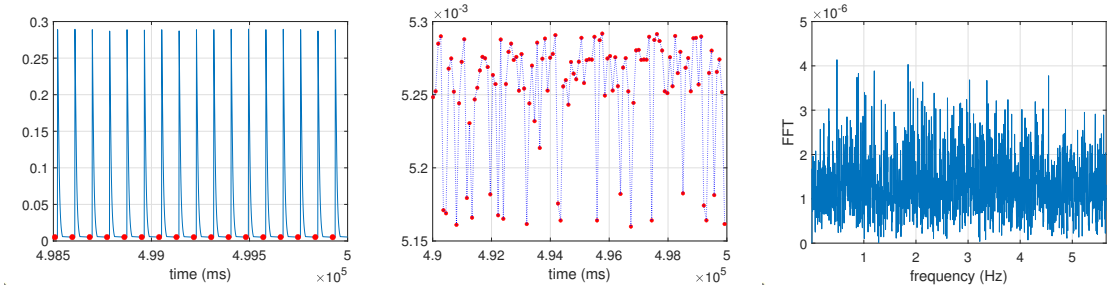

Figure 4. Results for $A = 0.475$, and $c = 87.5$ ms. Left figure: modeled action potential (blue) with depicted points, that are analyzed (red); middle figure: analyzed time series (red); right figure: Fourier spectrum of analyzed time series.

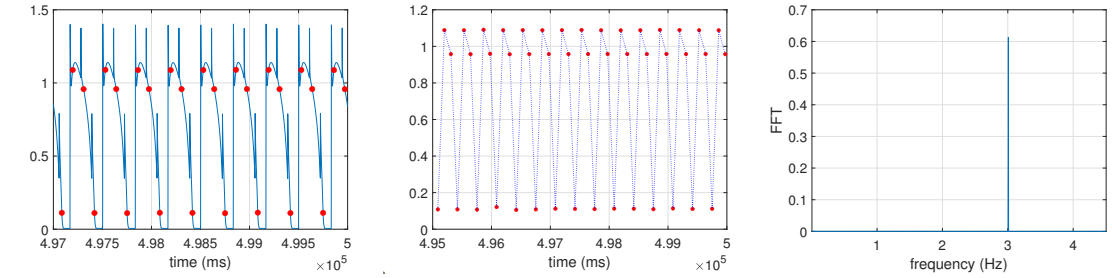

Figure 5. Results for $A = 0.75$, and $c = 110$ ms.Left figure: modeled action potential (blue) with depicted points, that are analyzed (red); middle figure: analyzed time series (red); right figure: Fourier spectrum of analyzed time series.

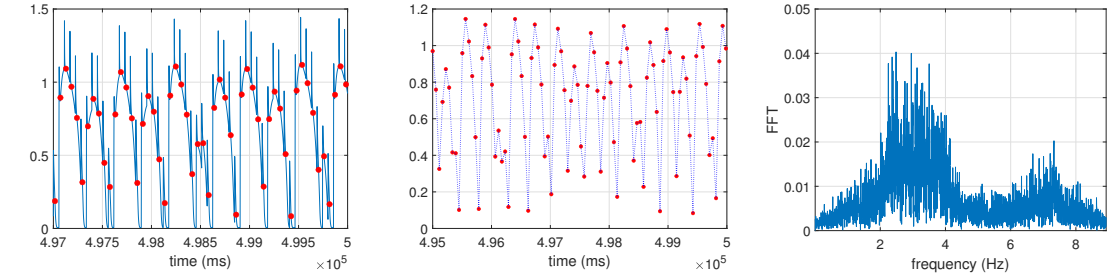

Figure 6. Results for $A = 0.75$, and $c = 55$ ms.Left figure: modeled action potential (blue) with depicted points, that are analyzed (red); middle figure: analyzed time series (red); right figure: Fourier spectrum of analyzed time series.

3.2. The 0–1 test for chaos

The 0-1 test for chaos was performed to detect chaotic movements in the investigated time series. This test was introduced in 2004 in the article [8] (see also [9]). One of the advantages of this test is that it works directly with the time series and therefore it is not necessary to reconstruct the motion of the dynamic system in phase space. The output value of this test is between 0 and 1. In the case of the resulting values approaching 0, we consider the examined time series to be regular. For a final value approaching 1, we consider the time series to be chaotic. If the final value of this test is not close to 0 or 1($(0.05, 0.95)$) it is not possible to decide whether it is

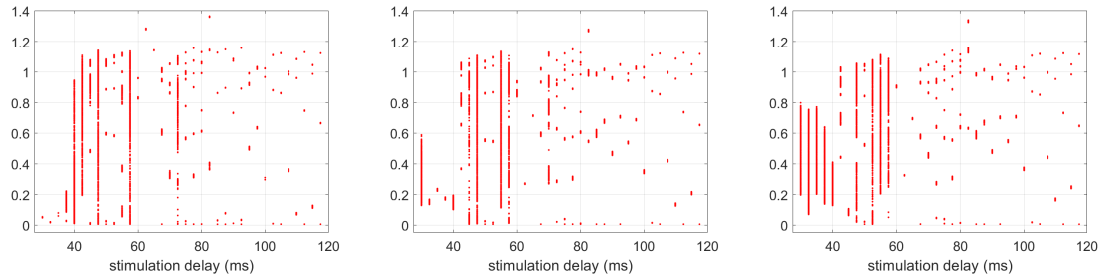

Figure 7. Bifurcation diagram of analyzed time series for $A = 0.55$ (left), $A = 0.85$ (middle), and $A = 1$ (right).

a chaotic or regular movement.

This test has been used in many different studies to detect chaotic motion in data. An example is [10], where the author investigated the motion of a double pendulum forced by biharmonic excitation or paper [11] where is used to find chaotic and regular motions of atomic force microscopy in tapping mode.

The 0-1 test for chaos is calculated in the following way. For a given set of observations $\phi(j)$ for $j \in \{1, 2, \ldots, N\}$ the translation variables $p_b(n) = \sum_{j=1}^{N} \phi(j)\cos(jb)$, and $q_b(n) = \sum_{j=1}^{N} \phi(j)\sin(jb)$ are calculated for a suitable set of values in $b \in (0, 2\pi)$. Subsequently, the mean square displacement is calculated using the following equation.

$$M_b(n) = \lim_{N\to\infty} \frac{1}{N} \sum_{j=1}^{N} [p_b(j+n) - p_b(j)]^2 + [q_b(j+n) - q_b(j)]^2$$

here $n \leq n_{cut}$ where $n_{cut} \ll N$. Next, the modified mean square displacement is estimated.

$$D_b(n) = M_b(n) - \left(\lim_{N\to\infty} \frac{1}{N} \sum_{j=1}^{N} \phi(j) \right)^2 \frac{1 - \cos(nb)}{1 - \cos(b)}.$$

Next, the correlation coefficients of ξ and Δ for the fixed parameter b are calculated.

$$K_b = \mathrm{corr}(\xi, \Delta)$$

where $\xi = (1, 2, \ldots, n_{cut})$ and $\Delta = (D_b(1), D_b(2), \ldots, D_b(n_{cut}))$. Finally, the resulting value of the 0-1 test for chaos is obtained as the median of K_b.

$$K = \mathrm{median}(K_b).$$

The resulting values of the 0-1 chaos test can be found in Figure 8. In this figure, it can be seen that chaotic movements occur mainly at low values of stimulation amplitudes ($A \leq 0.5$) or very fast stimulation frequencies ($c \leq 57.5$ ms). An example of these time series can be found in Figure 4, and 6. This chaotic area is disturbed by the regular movement detected especially at the stimulation delay $c = 50$ and $c = 52.5$ ms. Furthermore, a larger amount of regular behavior can be observed at the lowest investigated amplitude $A = 0.45$ (see Figure 2). Next, it can be noticed that the vast majority of regular behavior is concentrated in the region with a higher stimulation period and higher amplitude. An example of this time series can be found in Figure 5. In the figure, it can be also noticed several examples where it is not possible to decide on the regularity or chaos of the movement (points that are not drawn in red or blue). These time series occur mainly during transitions between regular and chaotic motion.

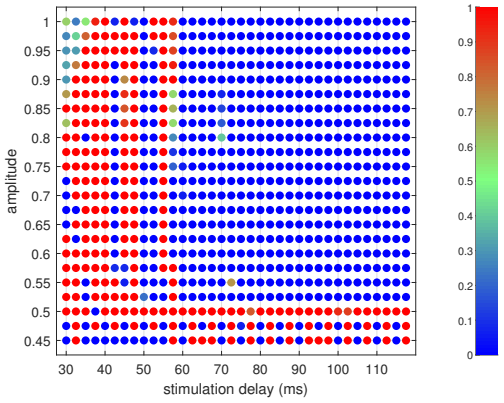

Figure 8. Results of the 0-1 test for chaos.

3.3. Entropy

Entropy calculations do not focus on the detection of regular and chaotic data but assess the overall complexity of the investigated time series. Therefore, using this method, it is not possible to decide whether it is a chaotic or regular movement of a dynamic system. The larger the value of entropy, the greater the complexity of the investigated time series. There are several types of entropies. For example can be mentioned are topological entropy [12], Kolmogorov-Sinai entropy [13], approximate entropy [14] and sample entropy [15]. Sample entropy (SampEn) is a modification of approximate entropy (ApEn) developed by Steve M. Pincus [14]. The main difference between a sample and approximate entropy is that SampEn does not include self-similar patterns as ApEn does. The definitions of ApEn and SampEn can be found in [16]. Sample and approximate entropy are used in this work for the analysis of the investigated time series.

The results of these tests can be found in Figure 9. In this figure can be seen that the results obtained with SampEn and ApEn are very similar. The highest complexity of the analyzed time series is concentrated in two areas of higher stimulation frequencies. One area is the amplitude of less than 0.65 ($A < 0.65$) and has a stimulation delay of less than 35 ms ($c < 35$). Another area can be found for $A \geq 0.65$ and $c < 50$. Higher data complexity can also be seen for stimulation amplitudes at which no cell stimulation occurs ($A < 0.5$). By comparing the results of the 0-1 test for chaos (see Figure 8) and entropy (see Figure 9) it can be noticed that the parameters where the higher entropy (data complexity) was measured are also parameters that the 0-1 test for chaos evaluated as chaotic.

4. Conclusions

In this study, the dynamic properties of the Bueno-Orovio-Cherry-Fenton model depending on the pacing amplitude and stimulation frequency were investigated. It has been shown that for regular stimulation, the model shows both regular as well as chaotic responses. These chaotic responses were detected using the 0-1 test for chaos. Furthermore, the complexity of the modeled action potential was investigated by calculating the approximate and sample entropy. It was found, that the modeled action potential reaches the highest complexity at high stimulation frequencies. By comparing the results of the 0-1 test for chaos and entropy was proved that time series with high signal complexity is also chaotic.

By comparing the results of this work with the dynamic properties of the improved Fenton-Karma model [2] and Beeler-Reuter model [3] it can be seen that the responses of the investigated

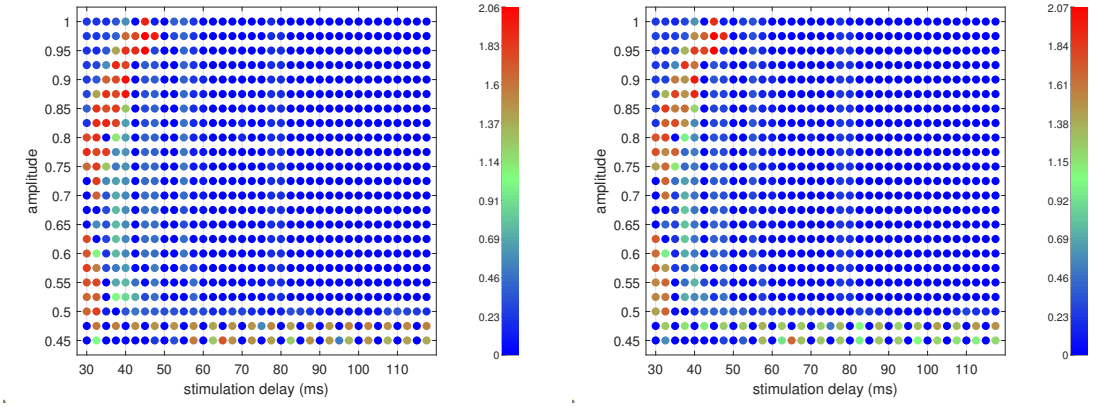

Figure 9. Results of the approximate entropy (left), and the sample entropy (right).

model are more chaotic at low stimulation amplitudes. Furthermore, it can be noted that the action potential of the Bueno-Orovio-Cherry-Fenton model is not chaotic for the stimulation delay of $c \geq 60$ (unlike other models). These differences in dynamic parameters can have several causes. These may be the properties of parametric sets examined in these works. Furthermore, this phenomenon can be caused by the way of evaluating the dynamic properties of a given model, or it can be the properties of the modeled equations.

Acknowledgements
This work was supported by The Ministry of Education, Youth and Sports from the National Programme of Sustainability (NPU II) project IT4Innovations excellence in science – LQ1602; by The Ministry of Education, Youth and Sports from the Large Infrastructures for Research, Experimental Development and Innovations project IT4Innovations National Supercomputing Center – LM2015070; by SGC grant No. SP2020/137 "Dynamic system theory and its application in engineering", VŠB - Technical University of Ostrava, Czech Republic.

References
[1] Weiss J, Garfinkel A, Karagueuzian H, Qu Z and Chen P 1999 *Circulation* **99** 2819–26
[2] Halfar R and Lampart M 2018 *Mathematical Methods in the Applied Sciences* **41** 7472–7480 (*Preprint* `https://onlinelibrary.wiley.com/doi/pdf/10.1002/mma.5060`) URL `https://onlinelibrary.wiley.com/doi/abs/10.1002/mma.5060`
[3] Halfar R 2020 *International Journal of Computer Mathematics* **97** 498–507 (*Preprint* `https://doi.org/10.1080/00207160.2019.1649662`) URL `https://doi.org/10.1080/00207160.2019.1649662`
[4] Suzuki A and Konno H 2011 *AIP Advances* **1** 032103 (*Preprint* `https://doi.org/10.1063/1.3614458`) URL `https://doi.org/10.1063/1.3614458`
[5] Lewis T J and Guevara M R 1990 *Journal of Theoretical Biology* **146** 407 – 432 ISSN 0022-5193 URL `http://www.sciencedirect.com/science/article/pii/S0022519305807507`
[6] Rappel W J, Fenton F and Karma A 1999 *Phys. Rev. Lett.* **83**(2) 456–459 URL `https://link.aps.org/doi/10.1103/PhysRevLett.83.456`
[7] Bueno-Orovio A, Cherry E and Fenton F 2008 *Journal of theoretical biology* **253** 544–60
[8] Gottwald A and Melbourne I 2004 *Proc. R. Soc. London A* **460** 603–611
[9] Gottwald A and Melbourne I 2009 *SIAM J. Appl. Dyn.* **8** 129–145
[10] Lampart M and Zapoměl J 2020 *Nonlinear Dynamics* **99** 1909–1921
[11] Ribeiro M A, Balthazar J M, Lenz W B, Rocha R T and Tusset A M 2020 *Shock and Vibration* **2020** 1–18 URL `https://doi.org/10.1155/2020/4048307`

[12] Lampart M and Raith P 2010 *Nonlinear Analysis: Theory, Methods & Applications* **73** 1533 – 1537 ISSN 0362-546X URL http://www.sciencedirect.com/science/article/pii/S0362546X10002725
[13] Clark D, Tarra L and Berera A 2020 *Phys. Rev. Fluids* **5**(6) 064608 URL https://link.aps.org/doi/10.1103/PhysRevFluids.5.064608
[14] Pincus S M, Gladstone I and Ehrenkranz R A 1991 *Journal of Clinical Monitoring* **7** 335–345
[15] Richman J S and Moorman J R 2000 *American Journal of Physiology-Heart and Circulatory Physiology* **278** H2039–H2049 pMID: 10843903
[16] Tomčala J 2020 *Entropy* **22** 863 URL https://doi.org/10.3390/e22080863

Chapter 5

Conclusion

In this work, the dynamic of cardiac electrophysiology is analyzed. Dynamic behaviour is investigated from the level of cardiac cells to the propagation of electrical signals in cardiac tissue. Furthermore, the work investigates the effect of pathological tissue scarring and detecting dangerous fibrotic structures that create proarrhythmic phenomena in cardiac tissue.

The presented results were published in impact research journals (WoS Q1-Q2). A list of all published papers (including two conference proceedings) that are thesis-related can be found in Appendix A. In addition, Appendix B is given a list of the author's thesis unrelated published results.

In this work, the chaotic properties of cardiac cell models were demonstrated. These properties were confirmed using classical and modern methods of dynamic systems, such as frequency analysis, bifurcation diagrams and the 0-1 test for chaos and the dependence of dynamic behaviour on stimulation parameters (amplitude and frequency) was shown. Since each model is built with a different level of abstraction, these dynamic behaviour changes also depend on the model used. These results were published as two research papers (see [**TR.1.2**] and [**TR.1.3**]) and two proceeding journals (see [**TR.2.1**] and [**TR.2.2**]).

The last part of this work is dedicated to the effect of pathological fibrosis spatial distribution on the appearance of proarrhythmic phenomena called unidirectional blocks (structures selectively blocking AP propagation from a specific direction). The results of this work were published in a research journal (see Paper [**TR.1.1**]). In work, the level of fibrotic changes at which the re-entrant propagation of the action potential is most likely to occur is found. This information was used to simulate a large number of pathological re-entrant propagations. Sites promoting re-entry were found in this data using the re-entry vulnerability index. By extracting the fibrotic pattern around these sites and patterns that do not manifest these phenomena, a dataset of 'save' structures and structures in which these proarrhythmic phenomena appear was created. A neural network was then trained to detect these proarrhythmic structures with more than 90% accuracy. These results provided evidence that using the spa-

tial distribution of fibrotic cells in the tissue can predict the emergence of these proarrhythmic phenomena. Furthermore, physical dimensions in which unidirectional block takes place were estimated using saliency maps.

In future work, further use of artificial intelligence (possibly in combination with features calculated using dynamic system methods) is planned. Further exploration of the possibilities of using artificial intelligence in combination with the implementation of real data can bring progress in diagnosing and treating heart diseases. By implementing RQA analysis, it is possible to more accurately detect the sites for targeting cardiac ablation (scaring the tissue to restore a healthy heartbeat). Moreover, by classifying fibrotic tissue, diagnosis can be made more efficient, and potentially dangerous cardiac scars that can lead to life-threatening pathologies can be detected. There is still a long way to go to achieve these goals, but the results presented in this work indicate that it is possible to get there and opens the way to new possibilities for computational electrophysiology research.

References

1. HÉNON, M. A two-dimensional mapping with a strange attractor. *Communications in Mathematical Physics*. 1976-02, vol. 50, no. 1, pp. 69–77. Available from DOI: 10.1007/bf01608556.
2. MARWAN, N. A historical review of recurrence plots. *The European Physical Journal Special Topics*. 2008, vol. 164, pp. 3–12. Available from DOI: 10.1140/epjst/e2008-00829-1.
3. MARWAN, Norbert; CARMEN ROMANO, M.; THIEL, Marco; KURTHS, Jürgen. Recurrence plots for the analysis of complex systems. *Physics Reports*. 2007, vol. 438, no. 5, pp. 237–329. ISSN 0370-1573. Available from DOI: https://doi.org/10.1016/j.physrep.2006.11.001.
4. GOTTWALD, A; MELBOURNE, I. A new test for chaos in deterministic systems. *Proc. R. Soc. London A*. 2004, vol. 460, pp. 603–611.
5. GOTTWALD, A; MELBOURNE, I. On the implementation of the 0-1 test for chaos. *SIAM J. Appl. Dyn.* 2009, vol. 8, pp. 129–145.
6. PINCUS, Steven M.; GLADSTONE, I.; EHRENKRANZ, Richard A. A regularity statistic for medical data analysis. *Journal of Clinical Monitoring*. 1991, vol. 7, pp. 335–345.
7. RICHMAN, Joshua S.; MOORMAN, J. Randall. Physiological time-series analysis using approximate entropy and sample entropy. *American Journal of Physiology-Heart and Circulatory Physiology*. 2000, vol. 278, no. 6, H2039–H2049. Available from DOI: 10.1152/ajpheart.2000.278.6.H2039. PMID: 10843903.
8. TOMČALA, Jiří. New Fast ApEn and SampEn Entropy Algorithms Implementation and Their Application to Supercomputer Power Consumption. *Entropy*. 2020, vol. 22, no. 8. ISSN 1099-4300. Available from DOI: 10.3390/e22080863.
9. DELGADO-BONAL, Alfonso; MARSHAK, Alexander. Approximate Entropy and Sample Entropy: A Comprehensive Tutorial. *Entropy*. 2019, vol. 21, no. 6. ISSN 1099-4300. Available from DOI: 10.3390/e21060541.

10. FENTON, F; KARMA, A. Vortex dynamics in three-dimensional continuous myocardium with fiber rotation: Filament instability and fibrillation. *Chaos: An Interdisciplinary Journal of Nonlinear Science*. 1998, vol. 8, pp. 20–47.

11. BEELER, G. W.; REUTER, H. Reconstruction of the action potential of ventricular myocardial fibres. *The Journal of Physiology*. 1977, vol. 268, no. 1, pp. 177–210. Available from DOI: 10.1113/jphysiol.1977.sp011853.

Appendix A

Author's thesis related publications

A.1 Journal articles

[**TR.1.1**]. **Halfar, R**, Lawson, BAJ, dos Santos, RW and Burrage, K. 2021. Machine Learning Identification of Pro-arrhythmic Structures in Cardiac Fibrosis. *Front. Physiol.*; 12:709485. https://doi.org/10.3389/fphys.2021.709485 (**Jimp, Q1**)

[**TR.1.2**]. **Halfar, R**. 2020. Dynamical properties of Beeler–Reuter cardiac cell model with respect to stimulation parameters. *International Journal of Computer Mathematics.*; 97:1-2, 498-507. https://doi.org/10.1080/00207160.2019.1649662 (**Jimp, Q2**)

[**TR.1.3**]. **Halfar, R**, Lampart, M. 2018. Dynamical properties of the improved FK3V heart cell model. *Math Meth Appl Sci.*; 41: 7472– 7480. https://doi.org/10.1002/mma.5060 (**Jimp, Q2**)

A.2 Proceedings articles (indexed)

[**TR.2.1**]. **Halfar, R**. 2021. Motions of the human cardiac cell electrophysiology model. *Journal of Physics: Conference Series.*; https://doi.org/10.1088/1742-6596/1730/1/012127

[**TR.2.2**]. **Halfar, R**. 2020. Characterization of Cardiac Cell Electrophysiology Model Using Recurrence Plots. *Chaos and Complex Systems. Springer Proceedings in Complexity.*; https://doi.org/10.1007/978-3-030-35441-1_8

Appendix B

Author's thesis unrelated publications

B.1 Journal articles

[**TU.1.1**]. Foltyn, J, Proto, A, Oczka, D, **Halfar, R**, et al. 2019. Evaluation of an Electro-Pneumatic Device for Artificial Capillary Pulse Generation used in a Prospective Study in Animals for Surgical Neck Wound Healing. *Scientific Reports.*; 9: 2045-2322. https://doi.org/10.1038/s41598-019-46397-0 (**Jimp, Q1**)

B.2 Proceedings articles (indexed)

[**TU.2.1**]. **Halfar, R**. 2020. Effects of Age and Illness to the Complexity of Human Stabilogram. *Chaos and Complex Systems. Springer Proceedings in Complexity.*; https://10.1007/978-3-030-35441-1_9

[**TU.2.2**]. **Halfar, R**, Litschmannova, M and Cerny, M. 2019. Effects of External Conditions to Chaotic Properties of Human Stability. *Advances in Intelligent Systems and Computing.*; 1011: 141-150. https://doi.org/10.1007/978-3-030-23762-2_13

[**TU.2.3**]. Foltyn, J, **Halfar, R**, Cerny, M and Noury, N. 2018. Multipurpose Sensor for Human Movement Analysis. *IEEE 20th International Conference on e-Health Networking, Applications and Services (Healthcom).*; https://doi.org/10.1109/HealthCom.2018.8531166

[**TU.2.4**]. **Halfar, R** et al. 2018. Sensor based solution for cranial remodeling orthosis. *IEEE 20th International Conference on e-Health Networking, Applications and Services (Healthcom).*; https://doi.org/10.1109/HealthCom.2018.8531080

B.3 List of software

[**TU.3.1**]. **Halfar, R**. 2019. dydea: Detection of Chaotic and Regular Intervals in the Data. Available online: https://CRAN.R-project.org/package=dydea